Chapter 3

SIDIS with CLAS12

Chapter 1 introduced polarized Semi-Inclusive Deep Inelastic Scattering (SIDIS) as a powerful tool for investigating the nucleon's internal structure, allowing access to the Transverse-Momentum-Dependent (TMD) distributions. This Chapter aims to outline a preliminary analysis of the Beam-Spin Asymmetry (BSA) associated with the structure-function $F_{LU}^{\sin\phi}$. It is treated as a case study on a possible measurement of non-perturbative QCD phenomena with flavor sensitivity, made possible by having an efficient PID apparatus. The analysis is performed on data acquired by the CLAS12 experiment at JLab, using the first module of the RICH installed in 2018 and refined information from the Pass2 reprocessing of data from periods with Hydrogen (RG-A) and Deuterium (RG-B) unpolarized targets. The second module was not available till the start of experiments with polarized targets in June 2022 whose data were still in the calibration phase at the time of this work. The analysis is based on the efficiency study reported in Chapter 2, which guarantees minimal pion contamination in the eK^+X sample. The study aims to show that it is possible to extract relevant observables with kaons, like the Beam-Spin Asymmetry, despite the reduction in statistics and the limited phase space available with the considered data set. The SIDIS data selection criteria, the analysis method, and the results are included in this Chapter.

3.1 Data

The analyzed data belong to CLAS12 Run Group B (RG-B) and were acquired in the spring of 2019. The target was unpolarized liquid Deuterium, and the longitudinally polarized electron beam was run at 10.6 GeV and 10.2 GeV with a current of 50 nA. The average beam polarization was $(84.8 \pm 1.5)\%$; it was monitored during the data-taking period by frequent measurements performed with the Moller polarimeter placed upstream CLAS12. The beam helicity was swapped with a frequency of 30 Hz to wash out detector effects

and minimize the systematic effects. The torus magnet was full-field *inbending*, pushing positive particles forward outward.

A control sample of data belonging to CLAS12 Run Group A (RG-A) acquired in the spring of 2019 was also used because of the very similar running conditions with respect to Run Group B (RG-B). In this case, the target was unpolarized liquid Hydrogen and the longitudinally polarized electron beam was run at 10.2 GeV with a current of 50 nA. The average beam polarization was $(84.5 \pm 1.5)\%$. The other conditions were the same.

The analysis is performed on positive kaons: the final state being eK^+X. The standard CLAS12 reconstruction provides the electron identification and the kinematic of the particles, while it is expressly required that the RICH identifies the kaon. These conditions reduce the available statistic because, at the time of data collection, only one of the six CLAS12 sectors was equipped with a RICH module. The analyzed data sample constitutes approximately one-third of the available statistics of electroproduction on Deuterium acquired by RG-B and one-fifth of that on Hydrogen by RG-A.

Most of the focus during the analysis was dedicated to the sample of data provided by RG-B; generally, the studies described refer to data of the scattering of electrons off the Deuterium target.

3.1.1 The CLAS12 SIDIS selection

Electron related cuts

The final states, which include one electron and one positive kaon, are considered in this analysis. For the electron selection, the standard CLAS12 conditions for SIDIS events were applied [48]:

- The electron has to be in the Forward Detector, i.e. its polar angle is between 5° and 40°.
- The electron has to be a trigger particle for the experiment.
- The number of photoelectrons in the HTCC has to be greater than 2.
- The energy in the PCAL has to be greater than 0.07 GeV.
- The DC fiducial cut developed for RG-A is applied (running conditions for RG-B were quite similar, except for the target that was Deuterium instead of Hydrogen, so no significant differences are expected).
- The z coordinate of track vertex was selected to be between −8 cm and 3 cm.
- The so-called "diagonal cut" is applied for the electron with momentum larger than 4.5 GeV. In this momentum range, the HTCC manifests some inefficiency in distinguishing electron and pion, which can be

mitigated using a selection based on the ratio of the energy deposed in the pre-shower and inner calorimeter.

- The ECAL fiducial cut, which allows to decrease the contamination of negative pion into the electron sample.

Hadron and RICH related cuts

Aiming to study the performance of the RICH, the following conditions were applied to the hadron:

- The particle has to be passed through sector 4 and identified by the RICH;
- Aiming to study the role of the RICH, the momentum is selected to be included in the detector nominal working range ($3 \div 8\,\mathrm{GeV/c}$);
- The DC fiducial cut developed for RG-A is applied (running conditions for RG-B were quite similar, except for the target that was Deuterium instead of Hydrogen, so no significant differences are expected).
- The z coordinate of track vertex is selected to be between $-10\,\mathrm{cm}$ and $2.5\,\mathrm{cm}$.
- Having the particle trajectory a key role in the ring reconstruction, which is based on a ray-tracing algorithm, the fitted DC track has to have a reduced $\chi^2_{track} < 8$.
- The number of photoelectrons in the RICH has to be greater than 2, to well-define the ring.
- The RICH *RQ* variable, defined in Section 2.4 and providing an estimation of the goodness of the identification, has to be larger than 0.1.

Kinematic cuts

Remembering notation defined for SIDIS in Section 1.3,

$$\ell(l) + N(P) \rightarrow \ell(l') + H(p_H) + X \tag{3.1}$$

where the quantities in parentheses represent the four-momenta, the following quantities can be defined:

- Q is the transferred momentum;

$$Q = \sqrt{(l' - l)^2} = \sqrt{-q^2} \tag{3.2}$$

- y is the fraction of electron energy transferred to the target;

$$y = \frac{P \cdot q}{P \cdot l} \tag{3.3}$$

- W is the center of mass energy

$$W = m_N^2 + 2m_N\nu - Q^2 \tag{3.4}$$

where ν is the energy carried by the virtual photon;

- MM is the missing mass of the reaction

$$MM = \sqrt{(E_{in} - E_{out})^2 - (\mathbf{p}_{in} - \mathbf{p}_{out})^2} \tag{3.5}$$

- z is the fraction of electron energy acquired by the kaon;

$$z = \frac{P \cdot p_H}{P \cdot q} \tag{3.6}$$

- x_F is the so-called Feynman x, which is the fractional longitudinal center-of-mass momentum of the hadron.

$$x_F = \frac{2p_H \cdot q}{Q^2} \tag{3.7}$$

On these quantities, the cuts based on the kinematic were applied:

- $Q^2 > 1\,\mathrm{GeV}^2$, to select the DIS regime.
- $y < 0.75$, in order to ensure the high virtuality of the photon, limiting the contributions from charge symmetric background and radiative effects.
- $W > 2$, to avoid nuclear resonances with relevant cross-sections.
- $MM > 1.6\,\mathrm{GeV}$, to minimize the contribution of exclusive channels.
- $z > 0.2$, to reduce the probability of hadrons deriving from baryon decays or target fragmentation. In this case, it can be tightned because the requirement on the hadron minimum momentum corresponds to $z > 0.4$
- $x_F > 0.0$, to minimize the effects related to the target fragmentation. In this case, it can be neglected because the high-momentum hadron automatically make the requirement satisfied.

Selection criteria not-RICH related	Original sample rejection [%]
DC fiducial cut on hadron	52.6
$\chi^2_{track}/NDF < 8$	50.0
y < 0.75	45.6
Other 11 cuts	$0.1 \div 15$ each
All non-RICH cuts combined	$96.6 \rightarrow 5.5 \times 10^5$ events

(a) Recap of the percentage of events rejected applying the different selection criteria. On top, the criteria that are independent of the RICH. In the last row is included the number of events that survived all the cuts.

Selection criteria on RICH variables	Reduced sample rejection [%]
RICH photons ≥ 3	46.7
$RQ > 0.1$	19.4
RICH-related cuts combined	$53.4 \rightarrow 2.6 \times 10^5$ events

(b) The effects of quality assessment that were previously defined for the RICH. In the last row is included the number of events that survived all the cuts.

Table 3.1: Recap of the percentage of events rejected applying the different selection criteria.

Cuts effect

The effect of cuts is evaluated on the sample of events which include a $3 \div 8\,\mathrm{GeV/c}$ K^+ identified by the RICH. This means that the used statistics is limited with respect the one available at CLAS12 because the RICH covers[1] one-sixth of the spectrometer.

The first step was to evaluate the rejection powers of non-RICH related criteria, defining the sample available for the RICH. Then, the effects of the quality assessment defined in Section 2.4 are evaluated on this reduced sample. The reduction in statistics produced by each cut was evaluated by applying them separately to the full sample and checking the size of the selected sub-sample. There are three main cuts rejecting approximately 50% of the events each. The other selection criteria, separately, rejected events in the range between $0.1 \div 15\%$ of the original sample. Combining the three main and the eleven secondary selection criteria, the subsample obtained consists of 7.3% of the original sample, which means $\sim 5.5 \times 10^5$ events.

The second step was to evaluate the effects of the RICH-related selection. The request of at least three photons rejected $\sim 46.7\%$ of the events, while the RQ cut rejected $\sim 19.4\%$ of the events. Combining them, the final sample is obtained and includes $\sim 2.6 \times 10^5$ events, corresponding to the 45.6% of the subsample that survived the non-RICH selections. Table 3.1 contains a recap of the effects of selection criteria.

The phase space covered by the particles surviving the selection is shown

[1] At the time of data taking only one CLAS12 sector was equipped with the RICH

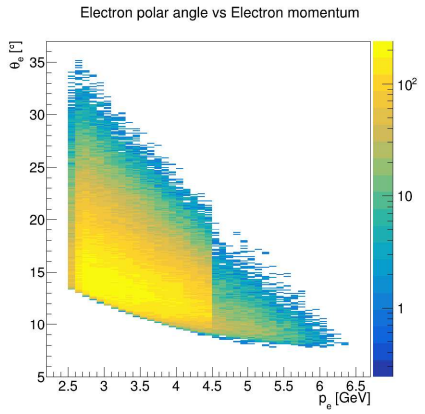

(a) Distribution of the polar angle and momentum of the selected electrons. The separation line visible at 4.5 GeV is due to the "diagonal cut".

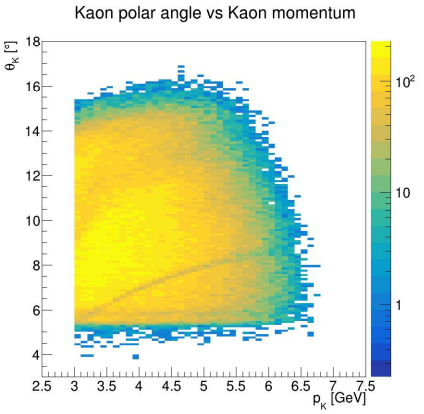

(b) Distribution of the polar angle and momentum of the selected kaons. The slightly darker line depends on the small separation between the two regions covered by the aerogel.

Figure 3.1: Phase space covered by the selected events.

in Figure 3.1, while the distributions as a function of Q^2, x_B, z, p_T are represented in Figure 3.2.

3.2 Analysis

Since the available statistic is limited, the Unbinned Maximum Likelihood (UML) method was selected to obtain the measurement. With respect to the binned method, UML requires more computational resources but provides more reliable results in case of low statistics because it computes the asymmetry term event-by-event instead of using a cumulative histogram. The analysis software was developed by the author using `C++` and Clas12root, a framework derived from ROOT CERN that includes methods to read the CLAS12 data files, that are coded in binary HIghly Performance Output (HIPO) format.

3.2.1 The Unbinned Maximum Likelihood fit

The UML Fit [47, 49] method is based on the assumption that the Probability Density Function (PDF) associated with the i event has the same functional form of the cross-section

$$PDF(x_i, \alpha) = \frac{\sigma_{UU}(1 + A_i(\alpha))}{\mathcal{N}\left(\int d\sigma_{UU}\right)} \tag{3.8}$$

where x_i is the set of variables associated with the event, α is a set of parameters, $\mathcal{N}$ is a term depending on $\int d\sigma_{UU}$ to normalize the PDF to 1,

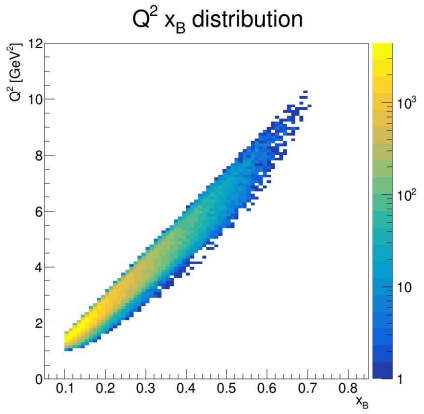

(a) Distribution of events as a function of the Q^2 and x_B variables.

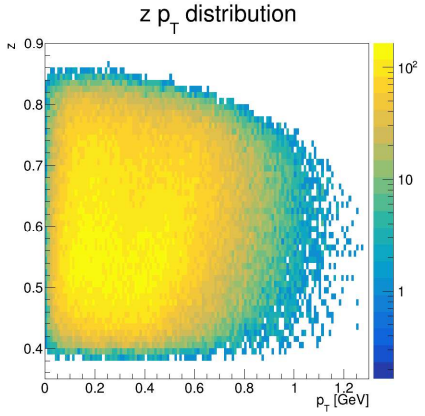

(b) Distribution of events as a function of the z and p_T variables.

Figure 3.2: Distribution of events in the four-dimension of interest.

σ_{UU} is the unpolarized cross-section, and A_i is a term taking into account the wanted asymmetry. If the unpolarized cross-section does not depend on the parameters of the fit, as it happens in this case, the PDF became

$$PDF(x_i, \alpha) = 1 + A_i(\alpha) \tag{3.9}$$

The likelihood function for a set of N independent events can be obtained as

$$\mathcal{L} = \prod_{i=1}^{N} PDF(x_i, \alpha) \tag{3.10}$$

Applying the logarithm to the $\mathcal{L}$ permits the transformation of the product into a sum, making easier the computation:

$$\log \mathcal{L} = \sum_{i}^{N} \log \left[PDF\left(x_i, \alpha\right) \right] \tag{3.11}$$

Under the hypothesis of a large sample of independent measurements, the logarithm of the likelihood behaves like a χ^2.

$$\chi^2 = -2 \log \mathcal{L} \tag{3.12}$$

so it is possible to extract the most probable value of the asymmetry by minimizing the χ^2.

To extract the $A_{LU}^{\sin\phi}$ asymmetry, the PDF is

$$PDF_{\pm}(x_i, A_{LU}^{\sin\phi}) = 1 \pm P_b(A_{LU}^{\sin\phi} \sin\phi_i) \tag{3.13}$$

where the sign changes following the helicity of the beam, and P_b is the beam mean polarization. This PDF is automatically normalized, so it can be used directly in the definition of the likelihood

$$\log \mathcal{L} = \sum_{i}^{N^+ + N^-} \log \left[1 \pm P_b \left(A_{LU}^{\sin\phi} \sin\phi_i \right) \right] \tag{3.14}$$

The $F_{LU}^{\sin\phi}$ term is related to the BSA $A_{LU}^{\sin\phi}$ by the equation

$$A_{LU}^{\sin\phi} = \frac{\sqrt{2\varepsilon(1-\varepsilon)} F_{LU}^{\sin\phi}}{F_{UU}} \tag{3.15}$$

where ε is a kinematic factor defined in Equation 1.12. Then, the likelihood is

$$\log \mathcal{L} = \sum_{i}^{N^+ + N^-} \log \left[1 \pm P_b \left(\frac{\sqrt{2\varepsilon(1-\varepsilon)} F_{LU}^{\sin\phi}}{F_{UU}} \sin\phi_i \right) \right] \tag{3.16}$$

and it is sufficient to minimize $-2\mathcal{L}$ to find the value of the structure-function ratio.

This method has the advantage of being independent of the binning in ϕ and provides results also if applied to relatively small samples. However, the UML method requires large computation resources to perform the minimization over thousands of events, and it is not always easy to define the PDF and its normalization. In the case of the extraction of $F_{LU}^{\sin\phi}$ for kaon, the advantages appeared more relevant than the disadvantages, so the UML was selected.

3.2.2 UML fit validation

The UML fit was implemented using the ROOT::Math::Minimizer class, which allows the minimization of a function depending on one or more parameters. The software was validated on the $e\pi^+X$ data acquired during Run Group A (RG-A), in the same experimental configuration of RG-B but using Hydrogen instead of Deuterium as a target. To validate the analysis, the structure-function ratio $\frac{F_{LU}^{\sin\phi}}{F_{UU}}$ is extracted as a one-dimensional function of x_B, z, and p_T and compared with the published result [38]. The validation process was performed using the baseline CLAS12 reconstruction software, excluding the RICH, to have the same phase space of the original analysis. The comparison of the results is shown in Figures 3.3a, 3.3b, and 3.3c. Despite the plots suggest a non-uniform systematic difference between the UML and published results, the trend of the functions is the same. The discrepancy is likely due to differences in the event selection of the two samples of pions. To validate this idea, a comparison between UML and binned fit was applied to the sample selected by the author, obtaining similar results. The plots are

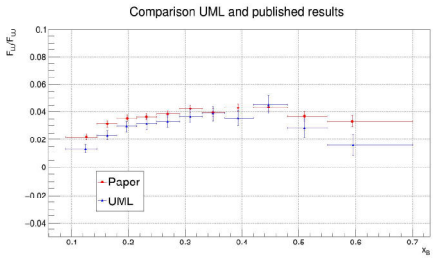

(a) Comparison as a function of x_B.

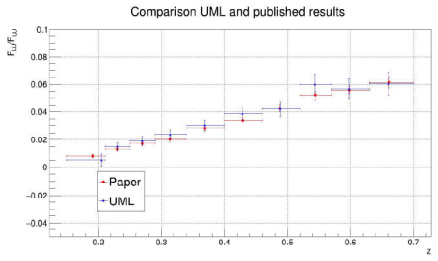

(b) Comparison as a function of z.

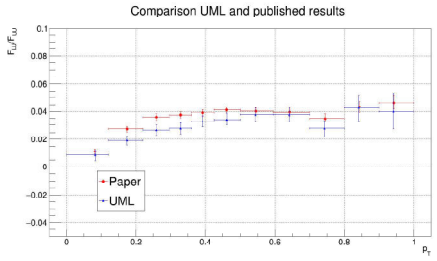

(c) Comparison as a function of p_T.

Figure 3.3: One-dimensional comparisons of the $\frac{F_{LU}^{\sin\phi}}{F_{UU}}$ obtained by the UML fit and published results on pion data. The plots show a small systematic difference between the two analyses. The one-dimensional plot as a function of Q^2 was not shown because it was not inserted in the Reference [38].

shown in Figure 3.4. Indeed, a small systematic difference is visible between the two methods. In principle, the UML fit should be more reliable because it does not suffer the binning effects, it has been used to obtain any other results shown in the following. In any case, a systematic related to the extraction method was evaluated and described in the following.

3.3 Systematic errors

The discussion of the systematic errors is still partially incomplete because the analysis could start only a few months before writing this document. Indeed the new version of the CLAS12 reconstruction software, the so-called Pass2, became available only after Summer 2023. Moreover, the CLAS12 simulation still does not include a RICH description compatible with Pass2, making the estimation of the systematics more complex. In any case, the present results focus on a subsample of the RICH data and are limited in statistical precision. A detailed systematic evaluation is not essential at this stage and will be evolved as needed. The systematic related to CLAS12 were derived from internal documents of the collaboration [50] and from the Reference reporting the CLAS12 results of pion BSA [38], being the two SIDIS analyses the same except for the selected hadron. The systematic related to the identification

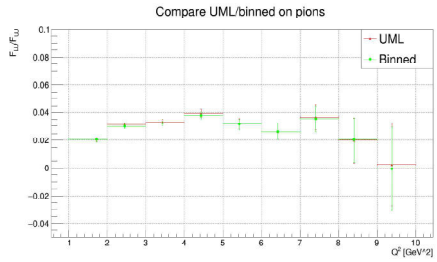

(a) Comparison as a function of Q^2.

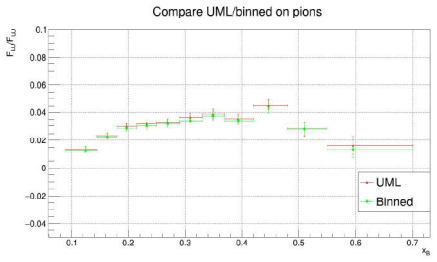

(b) Comparison as a function of x_B.

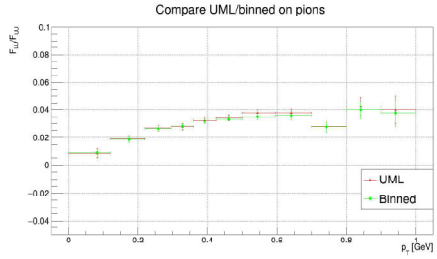

(c) Comparison as a function of p_T.

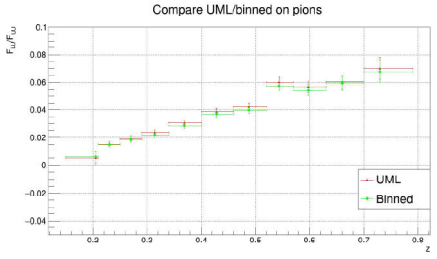

(d) Comparison as a function of z.

Figure 3.4: Comparisons between the $\frac{F_{LU}^{\sin\phi}}{F_{UU}}$ obtained by the UML fit and the binned fit as one-dimensional function in electron and hadron variables. The results were computed on the same sample of pions obtained using the baseline CLAS12 software. A small systematic difference is observed and accounted for in the systematics.

of the kaon, which is related to the main subject of this thesis, was evaluated by exploiting the results of the pion contamination on the kaon sample study described in Section 2.4.

3.3.1 Main systematic uncertainties from CLAS12 measurements

Beam polarization uncertainty

The beam polarization was approximately weekly measured during the CLAS12 data taking. The measurements were performed using a Moller polarimeter, with a typical systematic error of 2%. This value has to be added in quadrature to the corresponding statistical error computed for the data sample considered. The statistical uncertainty associated with the RG-B data was 1.5%. The total uncertainty on the beam polarization is therefore

$$p_b = (84.8 \pm (stat)1.5 \pm (sys)2.0)\% = (84.8 \pm 2.5)\%. \tag{3.17}$$

The relative uncertainty on the beam polarization is used to define the correspondent systematic uncertainty on the structure-functions ratio:

$$\frac{\delta \frac{F_{LU}}{F_{UU}}}{\frac{F_{LU}}{F_{UU}}} = \frac{\delta A_{LU}^{\sin\phi}}{A_{LU}^{\sin\phi}} = \frac{\delta BSA}{BSA} = \frac{\delta p_b}{p_b} = 2.9\% \tag{3.18}$$

Acceptance and bin migration effects

The acceptance effects should be studied using the Monte Carlo (MC) by introducing a controlled asymmetry and comparing the structure-function ratio obtained using the generated and reconstructed particle by the simulation. This study could not be carried out because the RICH volume is not yet available in the CLAS12 MC. It is assumed that the estimation made for the pion cases can be a reasonable value, that can be used for this preliminary analysis. Because the two analyses are performed on different phase spaces, the relative uncertainty is increased by a factor of 2 as a safety margin. The relative uncertainty in the pion cases was set to 2.7%, and it is set to be 5.4% for this kaon study.

Radiative effects

The emission of a radiative photon in the scattering process introduces a mismatch between the virtual photon energy and the reconstructed value, this causes a bias on the SIDIS kinematic. Currently, there are no tools available to accurately estimate radiative effects for SIDIS BSA. The cuts on y and on MM, combined with the accessible values of z and p_T, minimize the contaminations from the radiative tail of exclusive events. Moreover, the radiative effects are expected to be small in SIDIS processes thanks to the

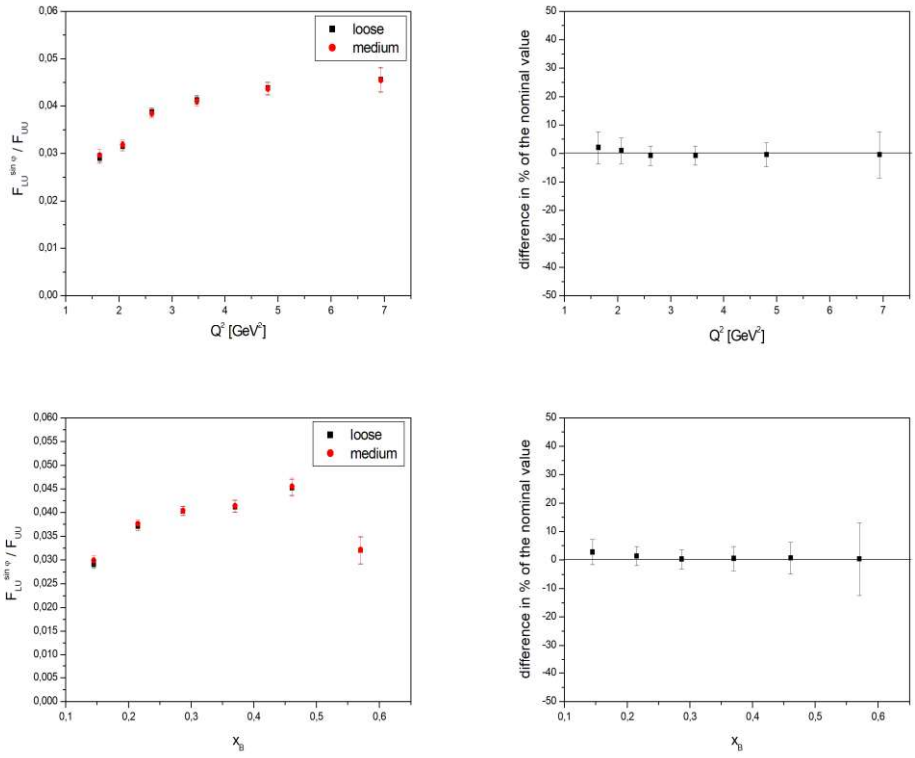

Figure 3.5: Plots describing the study on the effect the PCAL fiducial cut, taken from the CLAS12 RG-A common analysis note [50].

requirement of at least one hadron in the final state. For the case of pion, an estimation of the upper limit of the effect was performed using the dedicated software, setting this value at 3%. The analogous study for kaon is formally missing, but it is reasonable to expect a comparable effect; thus, for this preliminary study, the value estimated for pion was used.

Effects of fiducial cuts

The same fiducial cuts were applied to both the helicity states, and this effect was expected to be small. The main effect is related to the fiducial cut applied to the PCAL. By comparing the structure-function ratio for $e\pi^+X$ obtained by applying the loose and the medium cuts, as shown in Figure 3.5, the difference was found to be always less than the 5% and compatible with 0. As a consequence, this effect is neglected.

PID electron systematic effect

A possible source of systematic is the misidentification of negative pions as electrons. The diagonal and the ECAL fiducial cut reduce contamination to

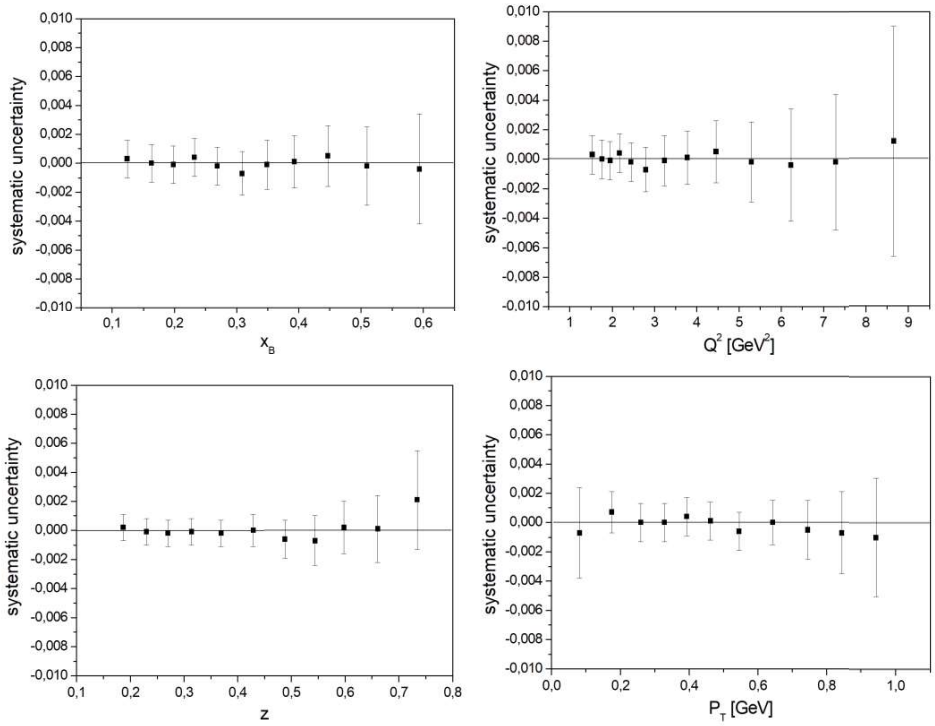

Figure 3.6: Systematic uncertainty associated with the π^- contamination into the e^- sample, taken from the CLAS12 RG-A common analysis note [50].

about 2%. The systematic uncertainty associated with the pion contamination into the electron sample can be estimated with the MC. It is assumed that the effect is largely independent of the positive hadron particle and, therefore, can be used for this preliminary kaon analysis. The relative uncertainty, as a function of x_B, Q^2, z, and p_T is shown in Figure 3.6. The effect is always comparable with zero, then it is neglected.

Extraction method systematic effect

Despite the previous consideration of expecting the UML fit theoretically better than the binned fit, it was decided to evaluate a systematic uncertainty depending on the extraction method, in case something in the implementation was not working as expected. For this reason, the systematic uncertainty was evaluated using the pion sample, which has larger statistics, to minimize the statistical fluctuations. The uncertainties were estimated from the comparison shown in Figure 3.4. The plots of the difference between the results obtained with UML and binned methods were fitted using a linear dependence. This allows the estimation of a possible constant term and dependence on the variable of interest. The linear functions describing the systematic uncertainty

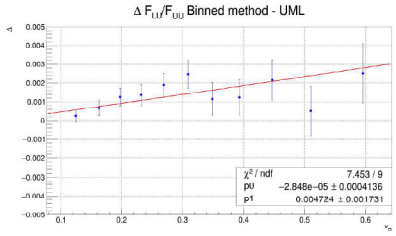

(a) Difference between UML and binned extraction results as a function of x_B.

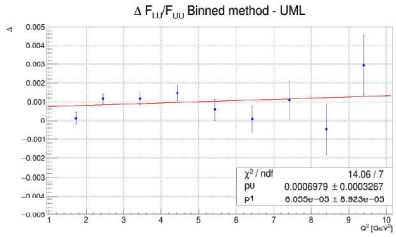

(b) Difference between UML and binned extraction results as a function of Q^2.

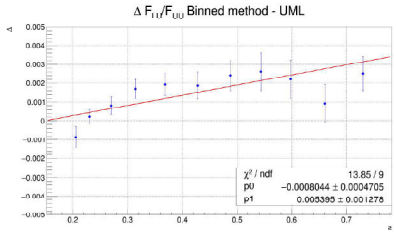

(c) Difference between UML and binned extraction results as a function of z.

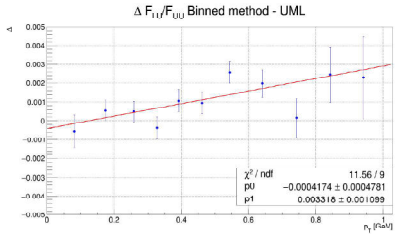

(d) Difference between UML and binned extraction results as a function of p_T.

Figure 3.7: Estimation of the systematic uncertainties related to the results extraction method.

are shown in Figure 3.7. To apply the systematic, it was computed bin-by-bin and introduced in the global uncertainty. To summarize it in a single value, the average of the relative error associated with the extraction method is 2.4%.

3.3.2 Systematic uncertainty caused by the kaon sample contamination

The systematic uncertainty on the structure-function ratio caused by the π^+ contamination of the K^+ sample was evaluated by exploiting the results of the study described in Section 2.4. The effect of pion contamination on the structure-function ratio (the ratio with F_{UU} is implicit) can be described by using:

$$F_{LU}^{meas} = F_{LU}^{K} + \delta F_{LU}^{cont} = F_{LU}^{K} + \left(\frac{N_\pi}{N_K} \Delta_{F_{LU}} \right) \tag{3.19}$$

where N_π is the number of pions contaminating the kaon sample, N_K is the number of kaons constituting the sample after removing the contamination, and $\Delta_{F_{LU}}$ is the difference between the structure-function obtained in pion or kaon SIDIS

$$\Delta_{F_{LU}} = F_{LU}^{\pi} - F_{LU}^{K}. \tag{3.20}$$

Because in this analysis the statistical error is dominating, it was decided to estimate an upper limit to this systematic uncertainty by taking a 50%

uncertainty $\Delta_{F_{LU}} \simeq F^{\pi}_{LU}/2$.

The F^{π}_{LU} used to evaluate the systematic was obtained from the $e\pi^+X$ events satisfying the same selection criteria applied to the kaon sample; in particular, the pion was recognized by the RICH. These selection criteria were determined to select a comparable phase space. The plots showing the systematic uncertainty as a one-dimensional function were fitted with a first-order polynomial to highlight trends. The linear function was used to estimate punctually the systematic uncertainty. The systematic as a one-dimensional function of the electron and hadron variables are reported in Figures 3.8a, 3.8b, 3.8c, and 3.8d.

In the four-dimensional analysis, the uncertainty derived from PID was estimated using the one-dimensional functions calculated at the mean value of the corresponding variable (computed for the bin) and averaging over the four dimensions. The systematic uncertainty on the structure-function ratio associated with the contamination of kaons from pion is included in the range between 0.0002 and 0.001, at least one order of magnitude less the current statistical uncertainty. This fact justifies the approximation of using the upper limits obtained identifying ΔF_{LU} with the 50% of the structure-function obtained from pion. Being this systematic effect small, it was simply introduced in the global uncertainty of the measurement without applying a specific correction. To do it, the systematic was computed bin-by-bin and summed in quadrature with other uncertainty sources. To summarize it in a single value, the average of the relative error associated with the pions contamination in the kaon sample is 1.9%.

3.3.3 Global systematic uncertainty

The global systematic uncertainty is computed by adding all the sources of systematic uncertainty in quadrature. Table 3.2 recaps the results described previously. The relative systematic uncertainty introduced by the non-RICH related sources is evaluated to be 7.1%. The RICH PID average systematic relative uncertainty is 1.9%, then minor but not negligible if compared with other sources. Thus, introducing this last effect, the relative global uncertainty became 7.4%. This value is still of the second-order effect with respect to the statistical uncertainty despite it being based on conservative estimates.

3.4 Results

The analysis is still partially incomplete because the Pass2 data became available only after summer 2023[2]. However, the aim of this study was to

[2]The work will not remain unfinished. It was not possible to complete it before the end of the Ph.D., but the author will continue to work with the CLAS12 data and conclude the analysis, aiming to achieve a publication.

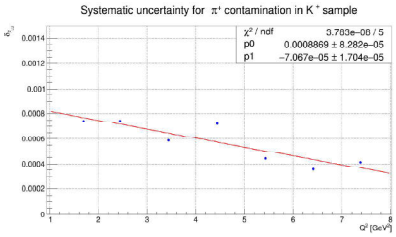

(a) Relative uncertainty associated with pion contamination into kaon sample.

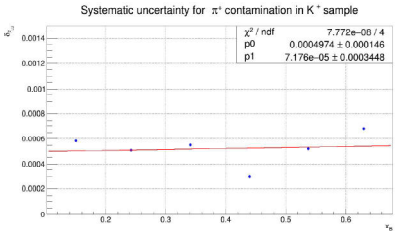

(b) Relative uncertainty associated with pion contamination into kaon sample.

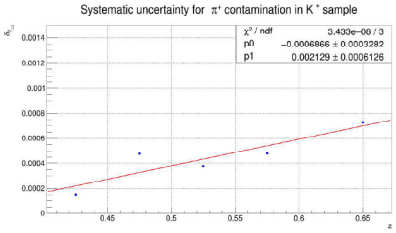

(c) Relative uncertainty associated with pion contamination into kaon sample.

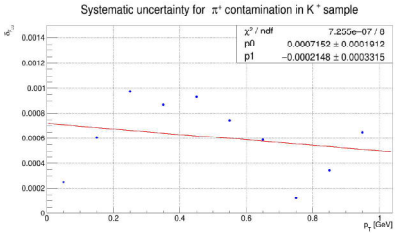

(d) Relative uncertainty associated with pion contamination into kaon sample.

Figure 3.8: Estimation of the PID systematic uncertainties related to the pion contamination into the kaon sample.

Uncertainty source	Average relative systematic uncertainty
Beam polarization	2.9%
Acceptance and bin migration	5.2%
Radiative effects	3.0%
Fiducial cuts	$\sim 0.0\%$
π^- contamination on e^-	$\sim 0.0\%$
Results extraction method	$\sim 0.0\%$
Extraction method	2.4%
Systematic excluding RICH	7.2%
π^+ contamination on K^+	1.9%
Total systematic uncertainty	7.4%

Table 3.2: Recap of the contribution to the systematic uncertainty.

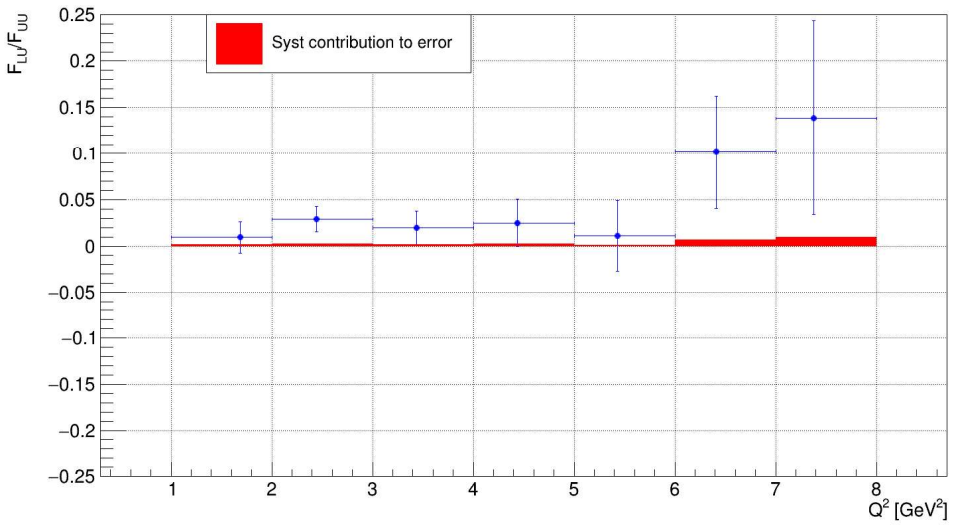

Figure 3.9: $F_{LU}^{\sin\phi}/F_{UU}$ as a function of Q^2. The red area shows the contribution of the total systematic uncertainty to the measurement error.

show that the BSA exists for kaons and it is detectable at CLAS12, and that an efficient PID identification based on RICH introduces only a small systematic uncertainty on the measurement. An analogous analysis was performed on data taken from CLAS12 RG-A, which ran the experiment in the same configuration of RG-B but using a Hydrogen instead of Deuterium target. The results from RG-A data are shown in Appendix A.

3.4.1 One-dimensional results

The one-dimensional results are shown as a function of the relevant electron and kaon variables in Figures 3.9, 3.10, 3.11, and 3.12. They show that the asymmetry is detectable using the CLAS12 spectrometer for kaons identified by the RICH. The red area indicates the total systematic uncertainty, which is a second-order effect with respect to the statistical uncertainty. Despite the limited statistical precision, the plots show the asymmetry tends to zero for vanishing z and p_T, as expected from theory.

3.4.2 Four-dimensional results

A four-dimensional binning was applied to the kaon sample because multidimensional analysis can provide useful information to constrain the theoretical models. The binning procedure was made in two steps: first, the sample is divided into three bins of the electrons' kinematical variables, which are represented in Figure 3.13a, and second, each of them is divided into four or six bins in the hadron variables, as shown in Figures 3.13b, 3.13c, and

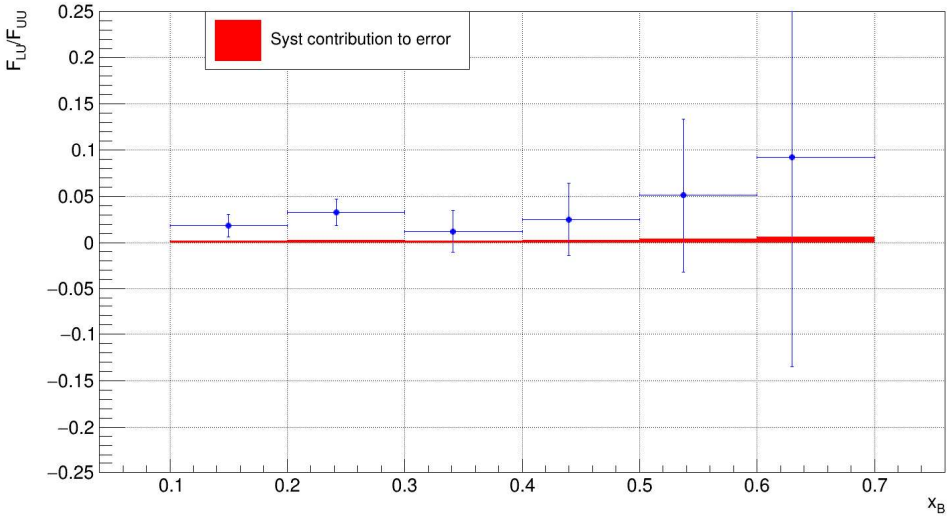

Figure 3.10: $F_{LU}^{\sin\phi}/F_{UU}$ as a function of x_B. The red area shows the contribution of the total systematic uncertainty to the measurement error.

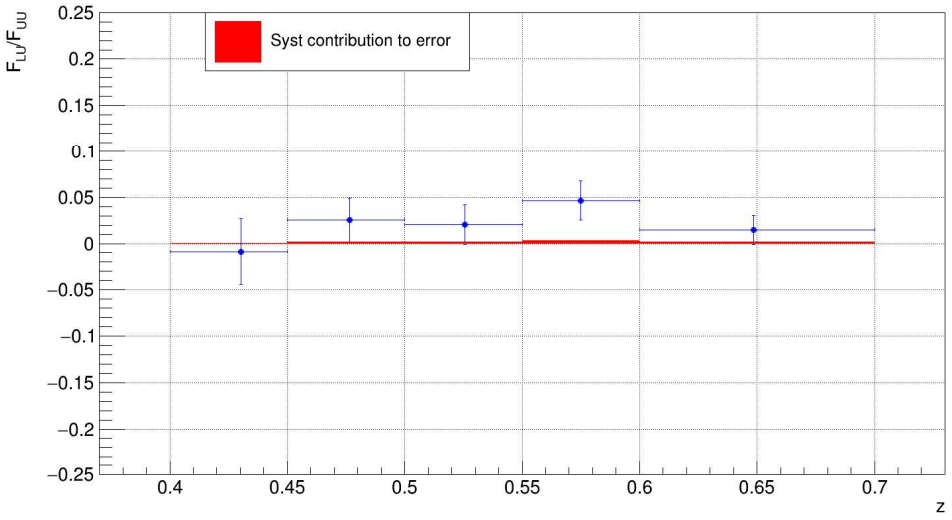

Figure 3.11: $F_{LU}^{\sin\phi}/F_{UU}$ as a function of z. The red area shows the contribution of the total systematic uncertainty to the measurement error.

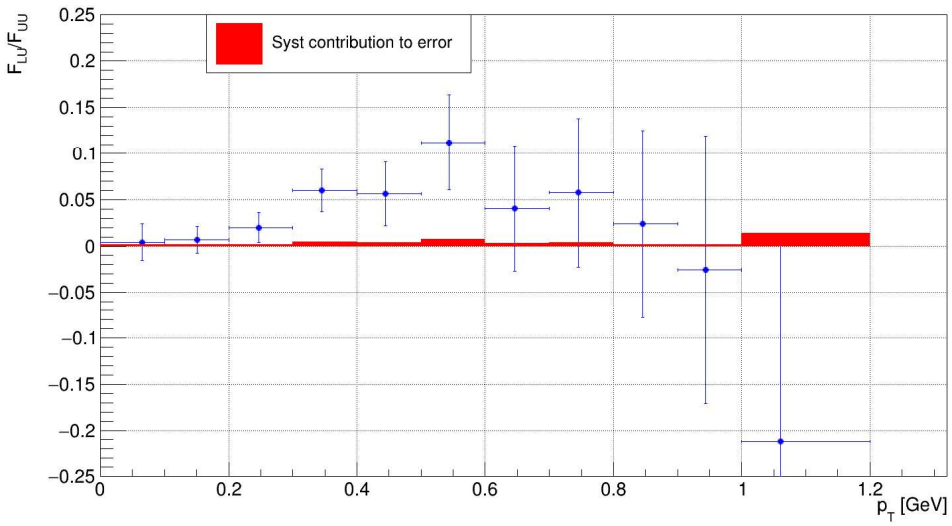

Figure 3.12: $F_{LU}^{\sin\phi}/F_{UU}$ as a function of p_T. The red area shows the contribution of the total systematic uncertainty to the measurement error.

3.13d. The main criteria were to maximize the number of bins but maintain sufficient statistics in the order of $\sim 10^4$events-per-bin.

The results as a function of p_T for each bin in the electron variables and hadron z are shown in Figures 3.14, 3.15, and 3.16. The plots show a behavior more consistent with theory for higher Q^2 bins, where the asymmetry tends to zero for small p_T and z, but the statistical error remains large. Increasing the statistics and the phase space in the future will provide possibilities to make more definitive conclusions.

3.4.3 Comparison between pion and kaon

It is possible to compare the $F_{LU}^{\sin\phi}$ structure-function obtained from SIDIS pion and kaon. The pion sample was selected, requiring the hadron to be identified by the RICH to obtain a phase space comparable with the kaon sample. All the selection criteria previously described for the kaon sample were applied to the pion sample.

The one-dimensional comparison of the structure-function obtained from pion and kaon is shown in Figure 3.17. Generally, the results obtained from analyzing the two samples are close, but especially the kaons are dominated by the statistical uncertainty. More reliable results could be obtained in future studies with the completion of the RICH alignment extending the accessible angle range up to the design value of 26° and analyzing the full statistics.

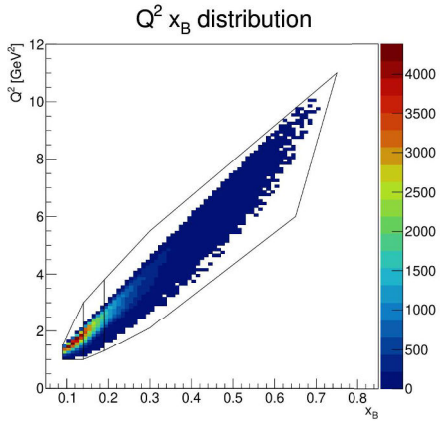

(a) Binning applied to the Q^2, x_B variables for kaons.

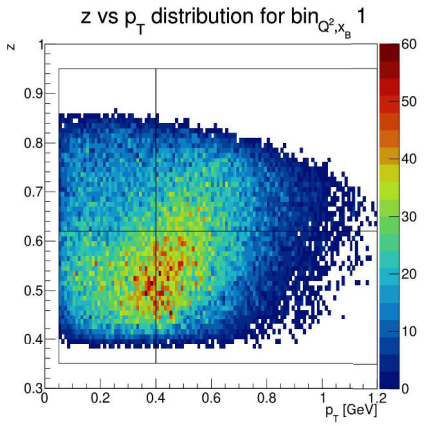

(b) Binning applied to the z, p_T variables for the first bin of Q^2, x_B.

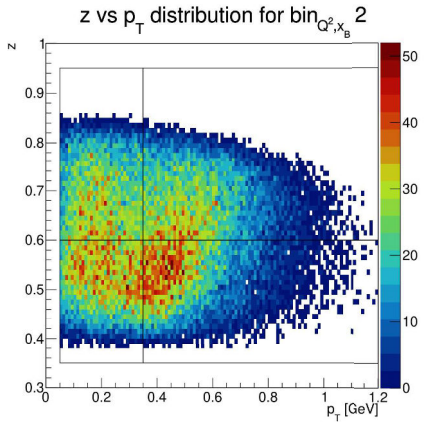

(c) Binning applied to the z, p_T variables for the second bin of Q^2, x_B.

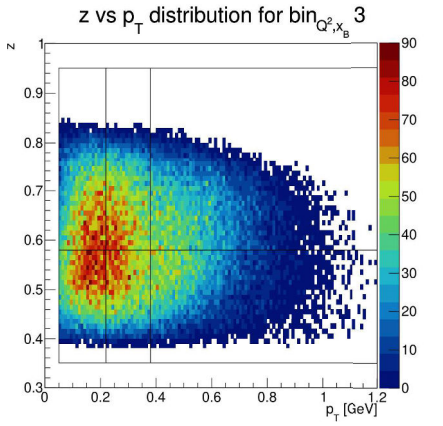

(d) Binning applied to the z, p_T variables for the third bin of Q^2, x_B.

Figure 3.13: Distribution of events in the four-dimension of interest.

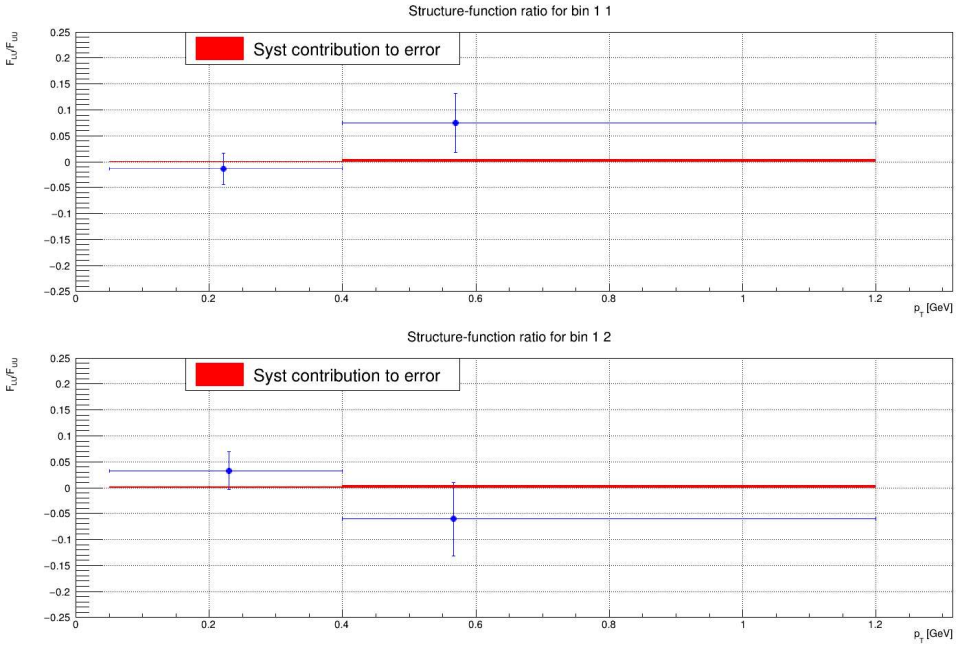

Figure 3.14: $F_{LU}^{\sin\phi}$ as a function of p_T, for the first bin on the electron variables and the two bins in z. The mean values and bin extremes are $Q^2 = 1.6(1.0, 3.0)$, $x_B = 0.12(0.09, 0.14)$ for both plots and respectively $z = 0.52(0.35, 0.62)$ and $z = 0.71(0.62, 0.95)$ for top and bottom. The x-coordinate of each point shows the mean value of p_T, and the correspondent error bar shows the bin width.

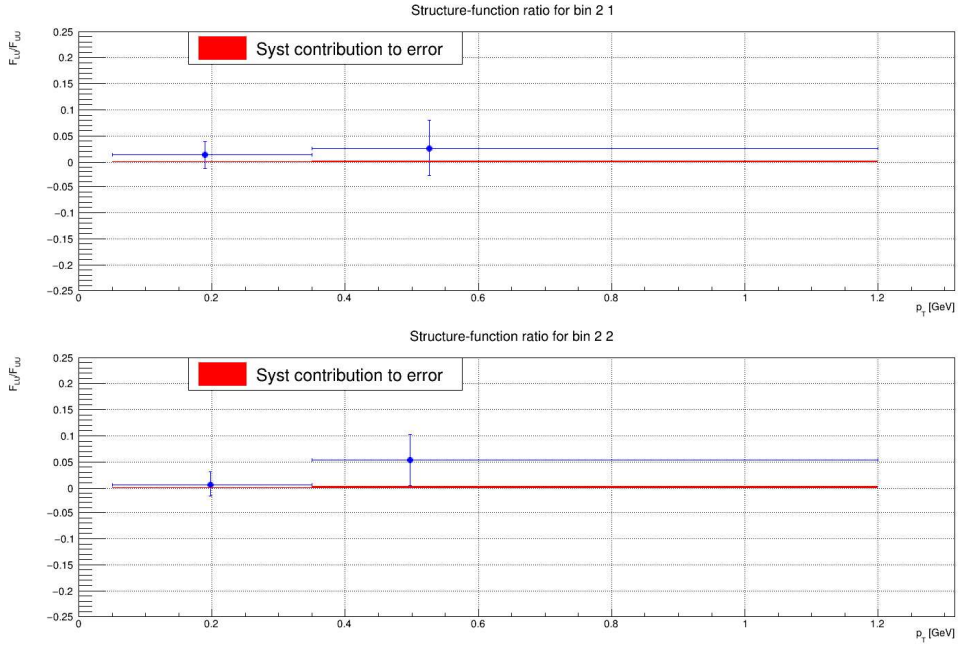

Figure 3.15: $F_{LU}^{\sin\phi}$ as a function of p_T, for the second bin on the electron variables and the two bins in z. The mean values and bin extremes are $Q^2 = 2.1(1, 3.8)$, $x_B = 0.16(0.14, 0.19)$ for both plots and respectively $z = 0.52(0.35, 0.60)$ and $z = 0.70(0.60, 0.95)$ for top and bottom. The x-coordinate of each point shows the mean value of p_T, and the correspondent error bar shows the bin width.

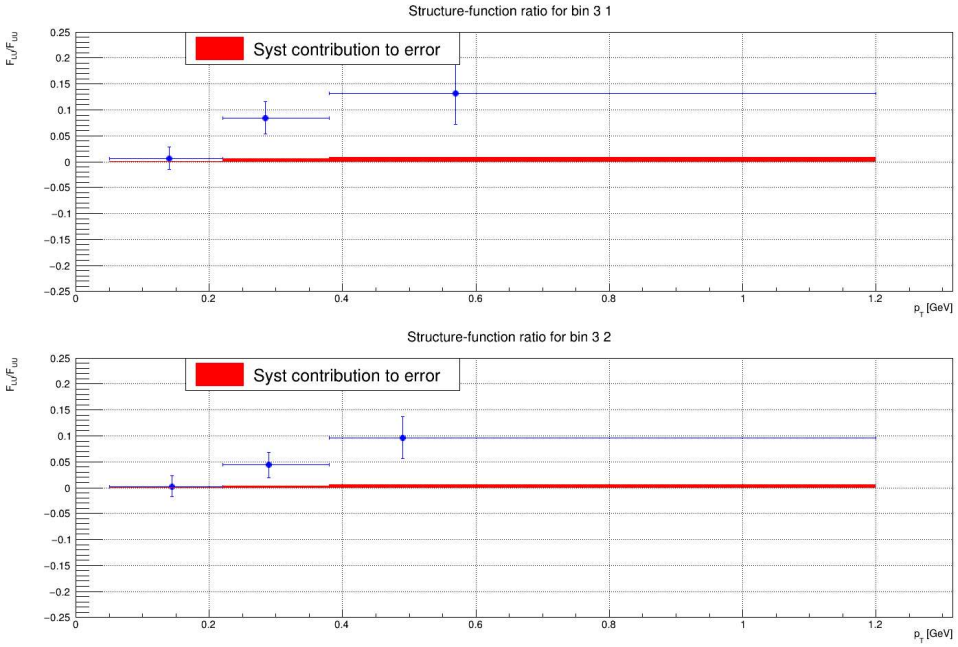

Figure 3.16: $F_{LU}^{\sin\phi}$ as a function of p_T, for the third bin on the electron variables and the two bins in z. The mean values and bin extremes are $Q^2 = 3.7(1.3, 11.0)$, $x_B = 0.28(0.19, 0.75)$ for both plots and respectively $z = 0.51(0.35, 0.58)$ and $z = 0.68(0.58, 0.95)$ for top and bottom. The x-coordinate of each point shows the mean value of p_T, and the correspondent error bar shows the bin width.

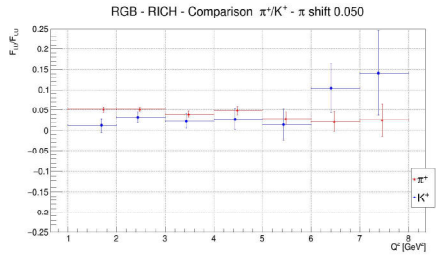

(a) Comparison as a function of Q^2.

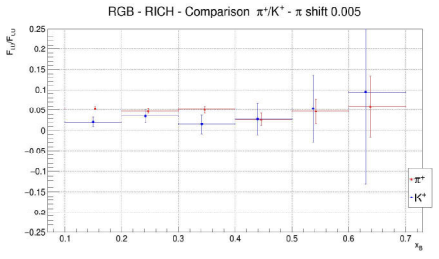

(b) Comparison as a function of x_B.

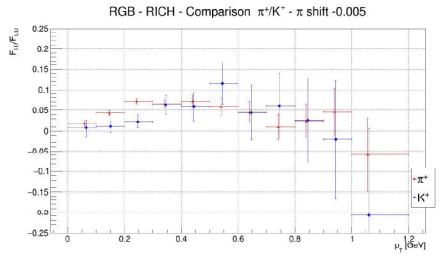

(c) Comparison as a function of p_T.

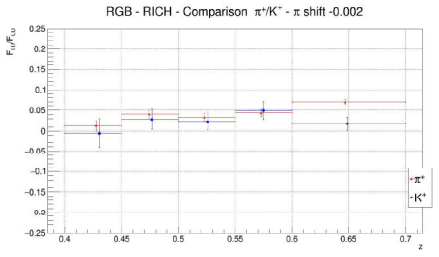

(d) Comparison as a function of z.

Figure 3.17: $F_{LU}^{\sin\phi}/F_{UU}$ obtained from pion and kaon samples identified by the RICH. The points for pion are slightly shifted along the x-axis to not overlap the error bars

3.4.4 Comparison with literature results

A preliminary comparison with results available in literature was done with HERMES measurement from Reference [51] and COMPASS measurement from Reference [52]. The results from HERMES are specifically obtained from kaon SIDIS, while COMPASS published results of positive mixed hadrons.

The mean values of kinematic variables are reported in Figures 3.18, 3.20, and 3.22. They show the capability of CLAS12 to extend the phase space to a higher x_B region. The kinematic regions are not easylly comparable, and more interesting information shall be available once the CLAS12 multi-dimensional analysis will be completed by running over all the available statistics and extending the kinematic region covered by the RICH when the software alignment will be completed.

The structure-function comparison are shown in Figure 3.19, 3.21, and 3.23. Despite all the limitations of the present analysis, CLAS12 results are comparable with the measurement of HERMES and COMPASS, and for several bins, show that the high-luminosity of CLAS12 allows a reduction of the statistical error. The addition of the second RICH module is expected to further reduce the impact of statistical error on kaon SIDIS measurement, allowing to obtain high-precision information to constraint theoretical models.

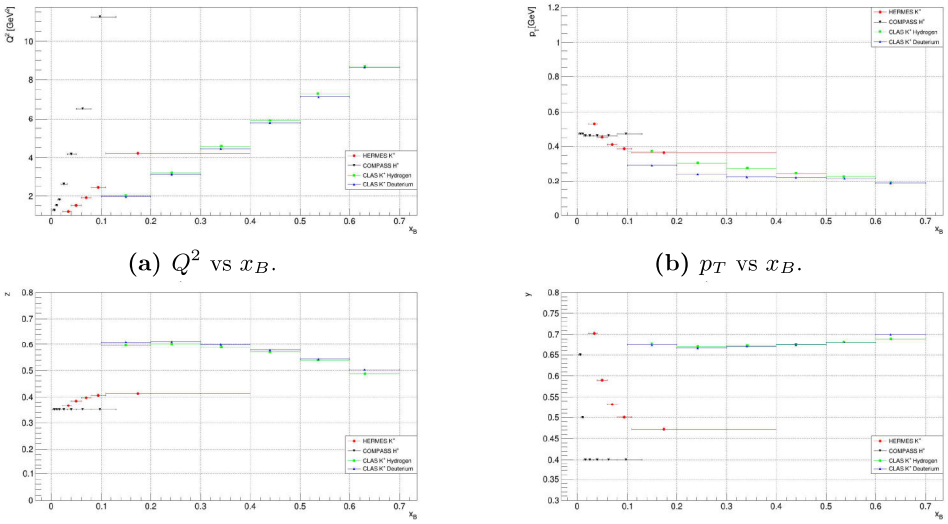

(a) Q^2 vs x_B.

(b) p_T vs x_B.

(c) z vs x_B.

(d) y vs x_B.

Figure 3.18: Trends of the kinematic variables Q^2, p_T, z, and y as a function of x_B for the results of experiments COMPASS, HERMES, and CLAS12. The y-axes of the plots are extended at least to the values achievable with CLAS12.

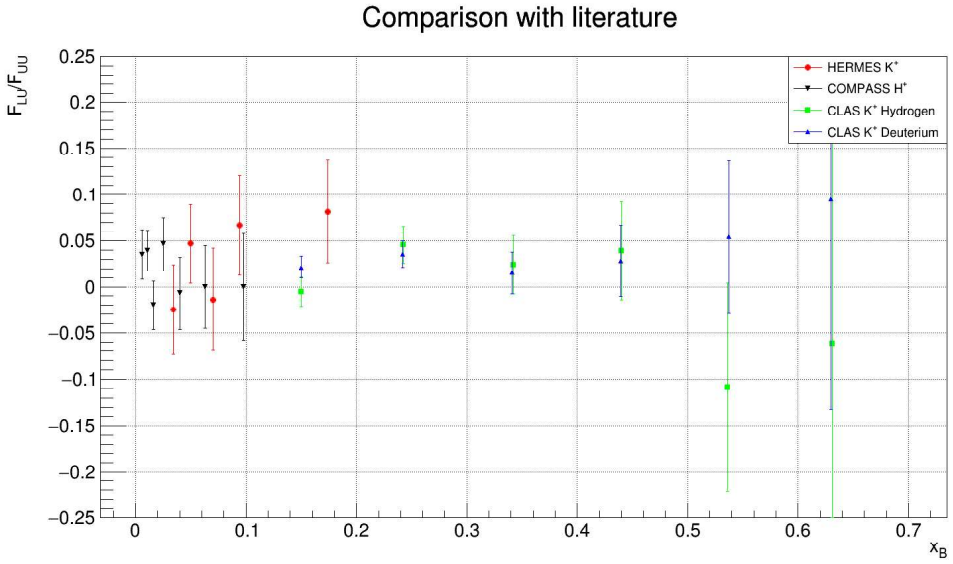

Figure 3.19: Structure-function measured from COMPASS positive mixed hadrons data [52], HERMES K^+ data [51], and CLAS12 RG-A and RG-B K^+ data, expressed as a function of x_B. The bin width bars were removed to make the plot more readable; they are the same as shown in Figure 3.18.

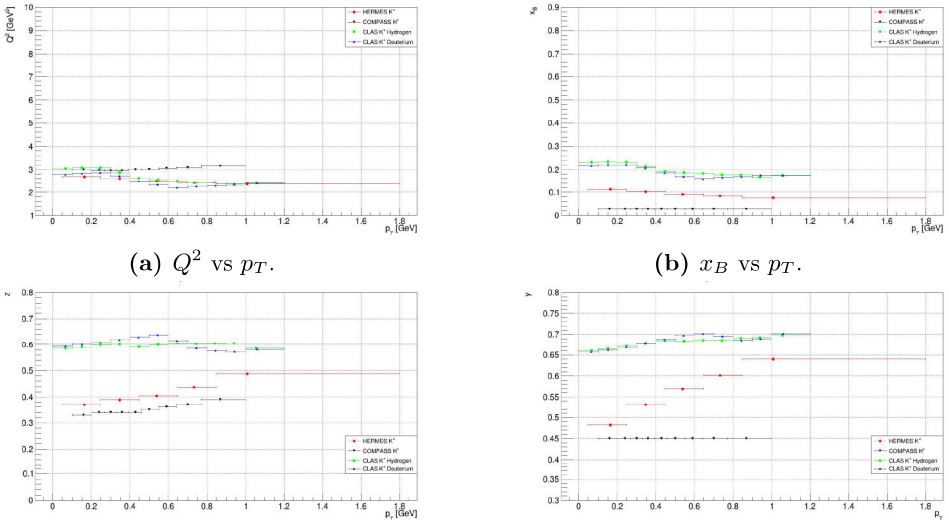

(a) Q^2 vs p_T.

(b) x_B vs p_T.

(c) z vs p_T.

(d) y vs p_T.

Figure 3.20: Trends of the kinematic variables Q^2, x_B, z, and y as a function of p_T for the results of experiments COMPASS, HERMES, and CLAS12. The y-axes of the plots are extended at least to the values achievable with CLAS12.

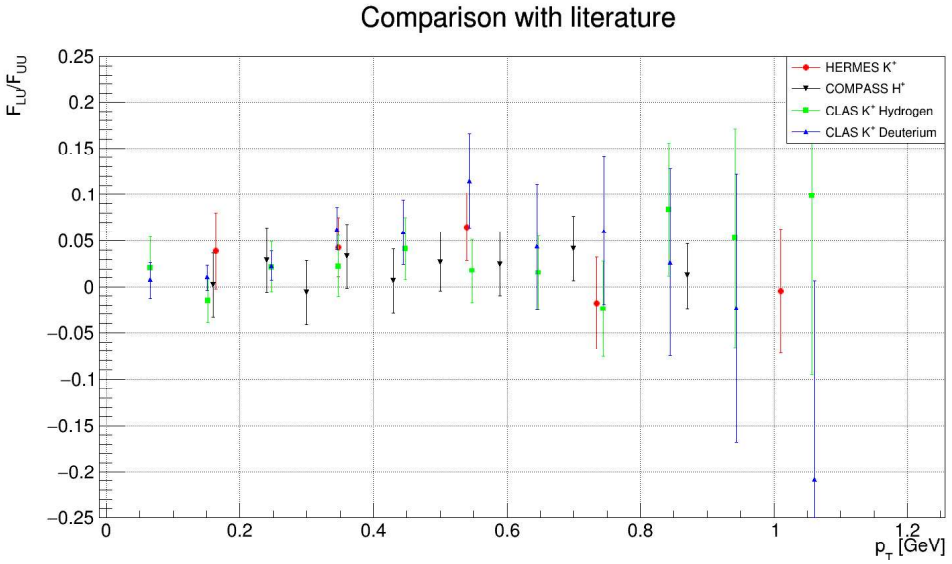

Figure 3.21: Structure-function measured from COMPASS positive mixed hadrons data [52], HERMES K^+ data [51], and CLAS12 RG-A and RG-B K^+ data, expressed as a function of p_T. The bin width bars were removed to make the plot more readable; they are the same as shown in Figure 3.20.

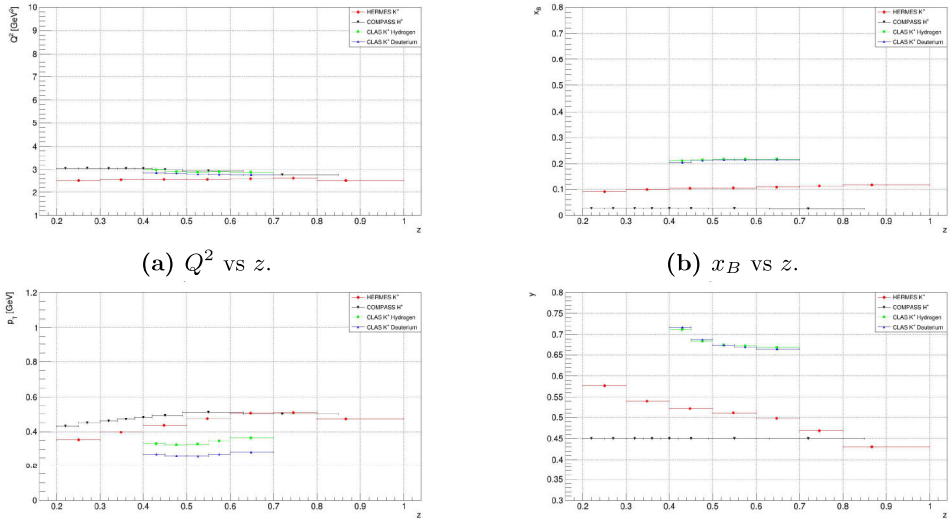

(a) Q^2 vs z.

(b) x_B vs z.

(c) p_T vs z.

(d) y vs z.

Figure 3.22: Trends of the kinematic variables Q^2, x_B, p_T, and y as a function of z for the results of experiments COMPASS, HERMES, and CLAS12. The y-axes of the plots are extended at least to the values achievable with CLAS12.

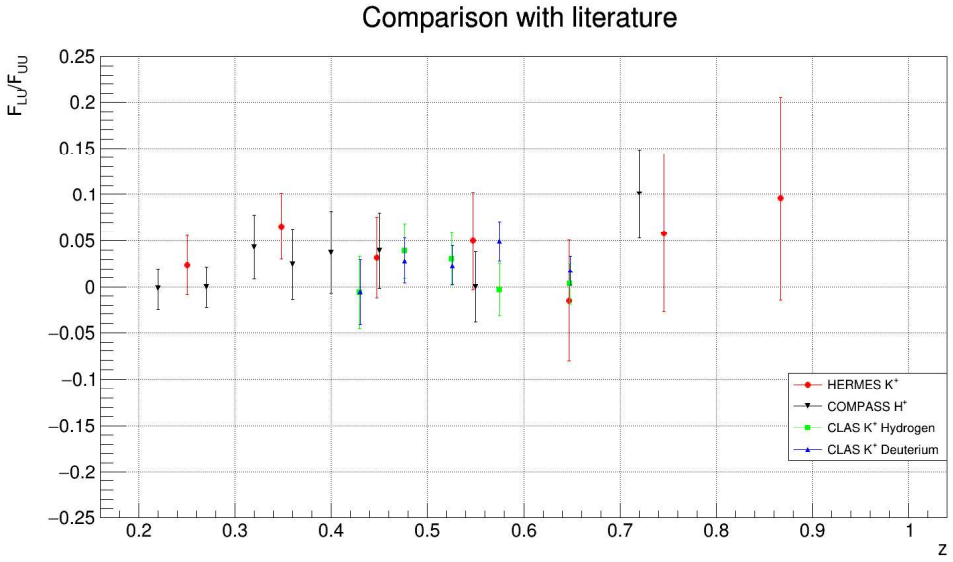

Figure 3.23: Structure-function measured from COMPASS positive mixed hadrons data [52], HERMES K^+ data [51], and CLAS12 RG-A and RG-B K^+ data, expressed as a function of z. The bin width bars were removed to make the plot more readable; they are the same as shown in Figure 3.22.

3.4.5 Future SIDIS studies using the CLAS12 RICH

This Chapter showed that from CLAS12 data it is possible to extract beam spin-asymmetries for SIDIS kaon despite the limited statistics analyzed. In the immediate future, the analysis will be extended to the full sample of recorded data on Deuterium, including several runs acquired with the torus in opposite polarization and more favorable for positive hadron acceptance. Moreover, the completion of the RICH alignment, made possible with the Pass2 reconstruction software, will permit to almost double the phase space covered up to the design value of 26° in polar angle. To ultimate the measurement, the data for kaons with momentum lower than 3 GeV, identified by the standard CLAS12 PID, can be included to further extend the phase space. The addition of the second module of the detector, which occurred in 2022, will increase the available statistics, allowing us to divide the data in more dense bins, providing more information to constrain the TMDs.

This study demonstrates the capability of the RICH to efficiently identify hadrons in the high-momentum range of CLAS12, between 3 GeV/c and 8 GeV/c. RICH information will help several studies that are ongoing on kaons, like the measurement of other terms of the SIDIS cross-section or the dihadron spin-asymmetries including at least one kaon. Moreover, the study of the high-momentum SIDIS kaons provides access to the high z region, and to the possibility of ancillary investigations, for example, about the role of vector mesons.

Chapter 4

The EPIC dual-radiator RICH

This Chapter focuses on Electron-Ion Collider (EIC), designed to be the world-leading facility to explore QCD. EIC goals are to provide precision 3D imaging of nucleons and nuclei, solve the proton spin and mass puzzle, investigate the quark and gluon confinement, and measure the peculiar correlations of quarks and gluons in the nuclear matter. The author significantly contributed to the development of the dual-radiator Ring Imaging Cherenkov (dRICH) for the Electron-Proton/Ion Collider Experiment (ePIC), a key component for identifying the hadrons produced in the EIC collisions. In particular, the author contributed to the studies based on the dRICH prototype performed along several test beams between 2021 and 2023. He developed the analysis software and the simulation framework, characterized the aerogel radiator samples, and was responsible for the tracking system during the data acquisition. The results obtained by the prototype are comparable with the expectation derived from the simulation and satisfy the requirements for the experiment.

4.1 The EPIC experiment at the Electron-Ion Collider

The EIC [20] is the new large-scale accelerator machine, which will be built at Brookhaven National Laboratory (BNL) in Long Island, New York, USA. The EIC will collide high-energy electron beams with high-energy proton and ion beams. The EIC will exploit high-intensity polarized beams to investigate QCD's new frontiers. The main design requirements of the EIC are:

- Beams of various ion species, from proton to uranium;
- Highly polarized beams $\sim 70\%$;

- Variable e+p center-of-mass energies in the range $20 \div 140\,\text{GeV}$;
- High collision electron-ion luminosity $10^{33} \div 10^{34}\,\text{cm}^{-2}\text{s}^{-1}$;
- Up to two general-purpose detectors.

These features will be accomplished using an electron storage ring with up to 18 GeV beam energy and a hadron storage ring operating at energies between 41 GeV and 275 GeV (protons), or 41 GeV and 110 GeV/nucleon (ion). The two beams will collide at a crossing angle of 25 mRad, allowing a quick separation, to bring focusing beam elements close to the interaction point and keep the synchrotron radiation background low. The EIC will replace the Relativistic Heavy Ion Collider (RHIC), the machine at BNL that is in operation until 2025. A scheme of the new accelerator is represented in Figure 4.1.

The first detector will be run by the 2022-born Electron-Proton/Ion Collider Experiment (ePIC) collaboration and located at the collider interaction point IP6. The ePIC collaboration includes 171 institutions from 24 countries and more than 500 participants. According to the scheme in Figure 4.2, ePIC will consist of a barrel-shaped central detector built around a 2 T solenoidal magnet, a far-forward electron detector, and a far-backward hadron spectrometer. These three detectors contribute to cover the whole phase space of the asymmetric lepton-hadron collision. Indeed, the three components of the experiment can see very different particles in terms of both momentum and particle types.

The magnet

The ePIC magnet will be the MAgnet with Renewed COils (MARCO), a 3.5 m long superconductive solenoid measuring 2.84 m of bore diameter at room temperature, providing a 2 T on-axis field directed along the beamline. The MARCO magnet will operate at 4.5 K.

The tracking and vertexing system

The ePIC tracking has to efficiently recognize patterns, provide a low material budget not exceeding $5\%X_0$, work inside the magnetic field, satisfy the geometrical constraints imposed by the solenoid in the barrel volume, and disentangle signal from the background. The system under development is a concept detector based on silicon and gaseous tracking technologies to ensure satisfactory space resolution, space point coordinates redundancy, and good time resolution. In particular, it will be based on the Monolithic Active Pixel Sensor (MAPS) tracker, providing a spatial resolution less than 5 µm (3 µm for vertex layer), and Micro-Pattern Gas Detectors (MGPDs), that can be implemented as µMEGAS or µRWELL to provide redundancy and a time resolution better than 10 ns.

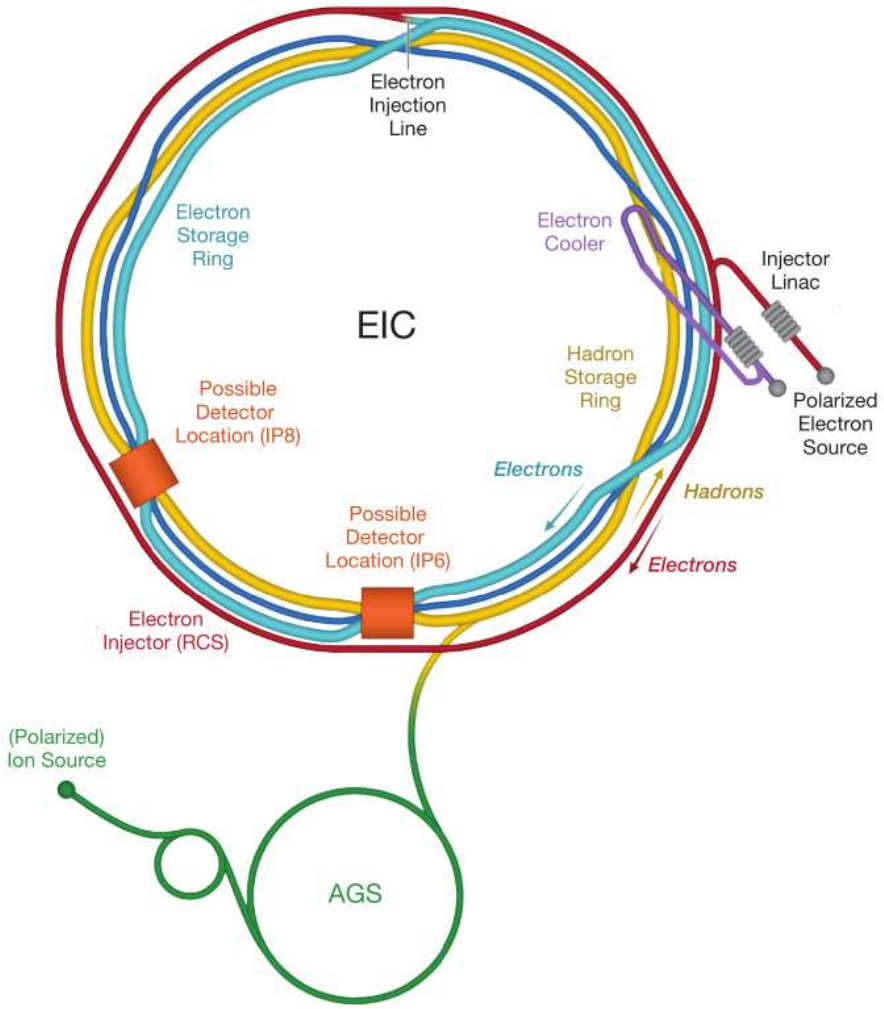

Figure 4.1: Scheme of the Electron-Ion Collider. The ePIC experiment will be located at the interaction point IP6.

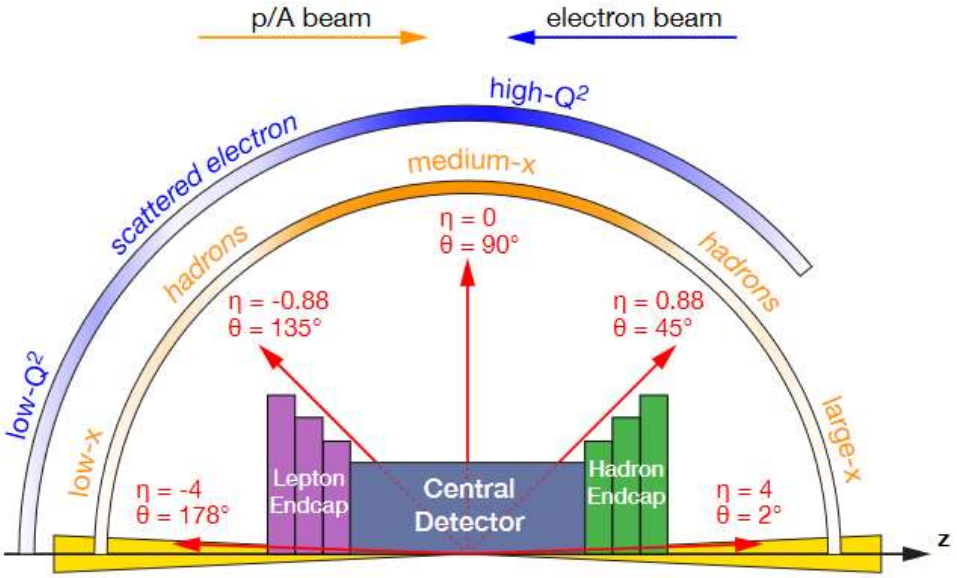

Figure 4.2: Scheme of the ePIC detector

The calorimetry system

The ePIC calorimetry system has to measure the particle's energy, provide continuous acceptance over the entire rapidity spectrum, be insensitive to the magnetic field, and operate up to the maximum luminosity in the expected background conditions. It must also contribute to distinguish electrons and photons and measure the particle's angle and position.

The Barrel Electromagnetic Calorimeter (bECAL) requires an energy resolution better than $\frac{7\%}{\sqrt{E}} \oplus 1\%$ and a fine granularity for good $\gamma - \pi^0$ separation. It has to measure energy down to 100 MeV and up to 10 GeV. These requirements must be achieved in a minimal space due to the geometrical constraints imposed by the solenoid. The detector will be a sampling calorimeter based on 6 layers of Astropix sensors alternated with 5 layers of lead and scintillating fibers readout by SiPM on both sides. The Astropix are SiPM developed for the Amego-X NASA missions and they are used for electromagnetic shower imaging. The scintillating fibers are used to profile the longitudinal dimension. The design allows to obtain a deep but still very compact calorimeter ($\sim 17X_0$ in 40 cm), an excellent energy resolution ($\frac{5.2\%}{\sqrt{E}} + 1\%$), an unrivaled low-energy electron-pion separation by combining energy measurement and imaging, and an exceptional position resolution. Moreover, the bECAL is deep enough to serve as the inner layer of the hadronic calorimeter.

The Barrel Hadronic Calorimeter (bHCAL) aims to precisely reconstruct the jet energy, provide a secondary determination of scattered electron kinematics, and help in muon identification. Moreover, it will also serve as

part of the solenoid flux return. The bHCAL will be realized by refurbishing the sPHENIX outer HCAL, a cylinder of 1.9 m inner and 2.6 m outer radius, 6.5 m long, made by 32 sectors including 48 towers of scintillators.

The Backward Electromagnetic Calorimeter (eECAL) plays a crucial role in almost every physics channel because it is responsible for detecting and measuring the kinematic of the scattered electron in the backward region, with rapidity $-3.5 < \eta < -1$. In particular, its goals are to separate electrons and pions, to provide a suitable resolution for electron detection at large $|\eta|$, to measure photons with good resolution, and to separate the 2γ from π^0 at high energy. The requirements for this detector are:

- Energy resolution of $\frac{2\%}{\sqrt{E}} + (1 \div 3)\%$;
- Pion suppression $1 : 10^4$;
- Minimum detection energy 50 MeV.

The eECAL comprises ~ 2850 $20 \times 20 \times 20\,\mathrm{cm}^3$ PWO crystals that fill a disk around the beamline. Each crystal will be read by 16 SiPMs connected to the front-end electronics. One of the most critical points regards the cooling system; thermal studies are ongoing to find the best solutions for efficiently cooling the system.

The Backward Hadronic Calorimeter (eHCAL) shall provide the functionality of a tail catcher for the electromagnetic calorimeter for electron identification and for the jet kinematics measurement at small x_B. The detector is made by ten alternating layers of 4 cm-thick stainless steel and 4 mm-thick plastic scintillator Kuraray SCSN-81. The scintillator's light will be extracted by 0.83 mm wavelength shifter fibers and detected by SiPMs. The front-end electronics will be selected in common with the other calorimetry systems.

The Forward Electromagnetic Calorimeter (hECAL) shall cover the pseudo-rapidity range $\sim 1 < \eta < 4$, achieve an energy resolution of $\frac{10\% \div 12\%}{\sqrt{E}} + 2\%$, provide a good π^0/γ separation up to 50 GeV, and contribute to the jet reconstruction. Moreover, it has to work in a magnetic region with expected neutron fluxes up to 10^{12} n/cm^2. It will be a sampling calorimeter of tungsten and scintillating fibers.

The Forward Hadronic Calorimeter (hHCAL) shall measure the energy with a resolution of $\frac{50\%}{\sqrt{E}} + 10\%$, with a minimum detected energy of 500 MeV. A high-granularity sampling calorimeter will cover the whole azimuthal angle by alternating small scintillator tiles and absorbing layers.

Particle Identification System

The Particle Identification (PID) system plays a key role in QCD studies needing flavor sensitivity, particularly for SIDIS. A plot reporting the phase

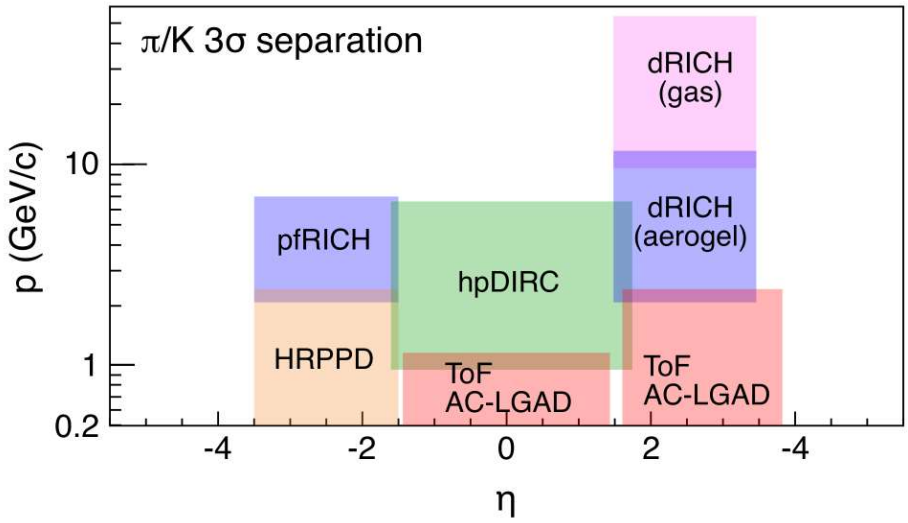

Figure 4.3: Phase space that needs to be covered by each PID subsystem.

space that needs to be covered by each PID subsystem is shown in Figure 4.3. In the backward direction, the proximity-focusing RICH (pfRICH) will provide a 3σ separation between π and K up to 7 GeV. Moreover, using the High Rate Picosecond Photo-Detector, the pfRICH will provide a 20 ps-resolution time measurement for a time-of-flight analysis and a spatial resolution of ~ 1 mm. The TOF will provide 3σ separation of low momentum pion and kaon in the barrel ($-1.4 < \eta < 1.4$, $0.2 < p < 1.2$ GeV/c) and in the forward endcap ($-1.74 < \eta < 3.83$, $0.2 < p < 2.3$ GeV/c).

The high momentum hadrons will be detected in the barrel by the high-performance Detection of Internally Reflected Cherenkov light (hpDIRC), a fast-focusing DIRC using a high-resolution 3D reconstruction. It will be made of 120 radiator bars producing Cherenkov light with the photons reflected over a focusing lens, an expansion volume, and the photo-detector. It will provide a 3σ separation for π/K up to 6 GeV and for e/π up to 1.2 GeV.

This work focuses on the design of the dual-radiator Ring Imaging Cherenkov (dRICH), a compact and cost-effective solution for broad momentum coverage at forward rapidity essential for SIDIS physics. It will interpolate the measurements of the Cherenkov angles of photons, produced by relativistic particles crossing two different radiators, to identify charged hadrons in the ePIC hadronic endcap. The dual-radiator unconventional design is due to most intriguing challenges of this detector: to identify charged hadrons in the extended momentum range between 3 and 50 GeV. Indeed, this momentum range bridges the few-GeV momentum region where the radiator is aerogel is the natural radiator and the high-momentum region where the gas radiator should be used. The dRICH will identify particles

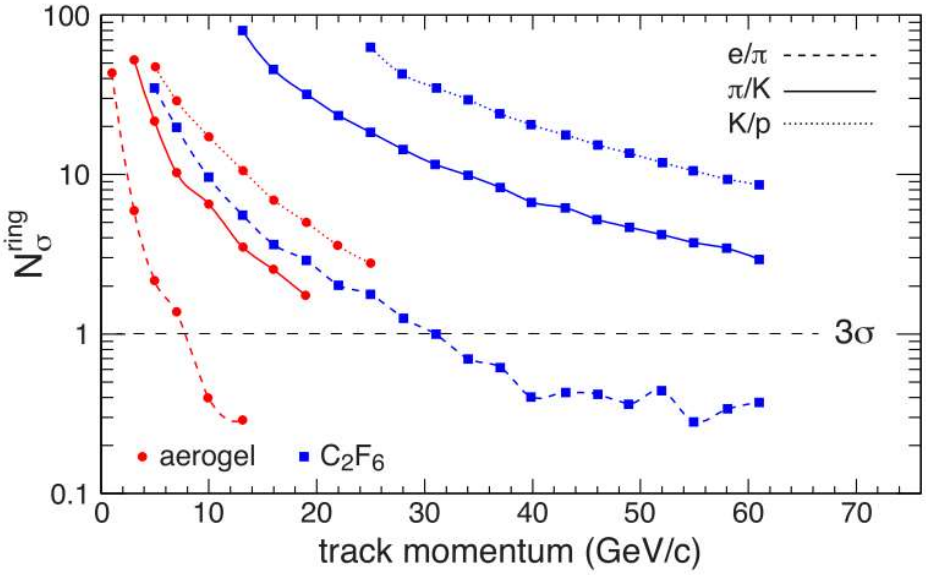

Figure 4.4: Expected separation achievable from the dRICH for a variety of particle species. Combining the aerogel and gas information provides uninterrupted PID across the full range.

in the pseudo-rapidity range $1.5 < \eta < 3.5$ and help identify electrons with momenta lower than 15 GeV/c. This detector should cope with the peculiar challenge of working in a high magnetic field, in the order of 1 T, so the magnetic-insensitive Silicon Photomultipliers (SiPMs) sensors are expected to be used. The usage of SiPM introduces a different issue related to the radiation damage that will occur on the sensors, increasing their dark count: a study on the recovery of the sensors via high-temperature annealing was performed and described later in this work. The expected performance of the detector is described in Reference [20] and is reported in Figure 4.4.

The dRICH will be located in the hadronic endcap, between the MARCO magnet and the calorimeter. To fit in the limited available space between them is another challenge for the dRICH. Currently, the detector is designed as a cylindrical shape for a total length of 120 cm and a maximum radius of 180 cm. A sketch of the dRICH is shown in Figure 4.5. It will be divided into six identical sectors, each of them containing the radiators, spherical mirrors, and photosensors.

The rest of the Chapter will describe the ongoing studies on the mitigation of SiPM radiation damage and the performances achieved with the dRICH prototype assembled in Ferrara in 2021.

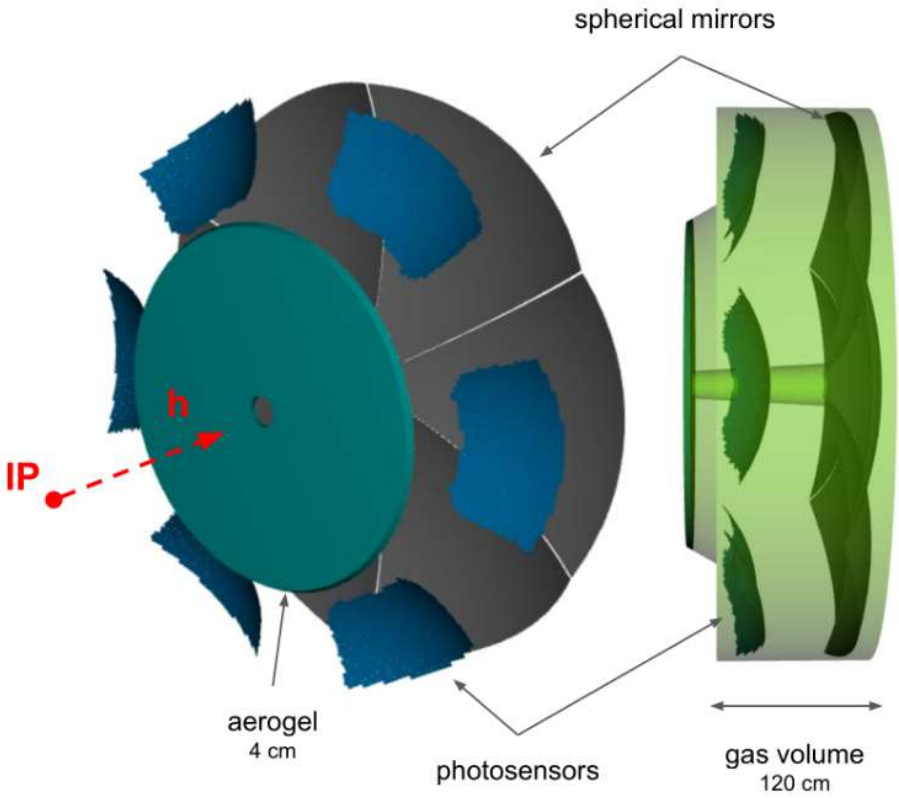

Figure 4.5: Sketch of the ePIC dRICH.

4.2 The recovery of SiPM radiation damage via annealing

It is expected that during the lifetime of the ePIC experiment, the photosensors of the dRICH will receive radiation in the order of $10^{11}\,\mathrm{n_{eq}/cm^2}$, which will dramatically affect the Dark Count Rate (DCR), increasing it over the acceptable rate of $\sim 300\,\mathrm{kHz}$. This value corresponds to an expected number of background hits at the level of the signal hits (photon) from aerogel. Several options are available to maintain the DCR to an acceptable level, namely by reducing the SiPM operating temperature (cooling), using the timing information of high-precision Time-to-Digital converter electronics (gating), and recovering the radiation damage with high-temperature annealing cycles (curing) [53]. The cooling and gating procedures are well known and will be used for the dRICH; the curing via annealing has been the subject of dedicated tests since 2021 and has provided positive indications that confirmed the possibility of using it for the final detector [54]. The following SiPM sensors have been studied:

- Hamamatsu S13360-3050VS and S13360-3025VS;
- Hamamatsu S14160-3050HP and S14160-3015PS;
- Fondazione Bruno Kessler (FBK) NUV-HD-CHK and NU-HD-RH prototype devices;
- Onsemi MICROFJ-30035.

The SiPM sensors have been irradiated on several occasions between 2021 and 2023 in the experimental room of the Trento Proton Therapy facility; this was done with 140 MeV protons produced in a large and uniform irradiation field [8]. The NIEL-scaling hypothesis is used to normalize the proton fluence to the corresponding 1-MeV neutron equivalent [55]. A dedicated collimator system was designed to deliver the uniform irradiation field in a 3 mm wide slit such that, thanks to a precision micrometric translation system, a single column of sensors (6 or 8 SiPM) in a matrix is irradiated at a given time.

Two pictures of the custom boards are shown in Figure 4.6. For each board, three different columns have been exposed at three different levels of irradiation: 10^9, 10^{10}, and $10^{11}\,\mathrm{n_{eq}}$. The fourth column was used to control the background neutrons generated by the scattering system and the collimators. Background neutrons received by each board are estimated to correspond to $\sim 2 \div 3 \times 10^8\,\mathrm{n_{eq}}$. The sensors were characterized in a climate chamber, which provides a stable room temperature of $-30\,^{\circ}\mathrm{C}$ to control the background DCR. The characterization station is shown in Figure 4.7.

The effect of the irradiation is represented in Figure 4.8, which shows the increase of the dark current and DCR of the SiPM as a function of the

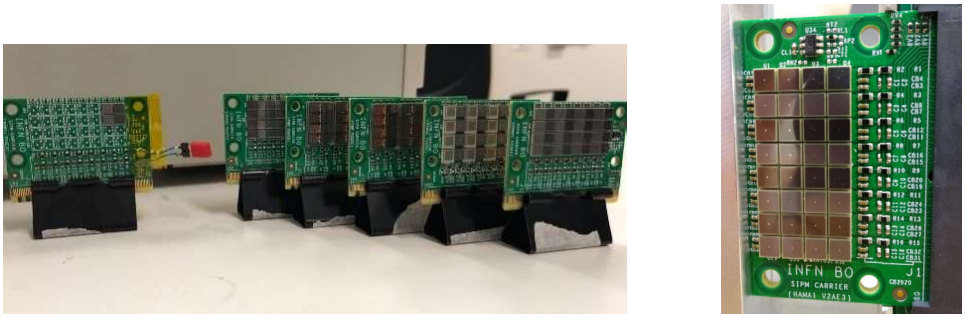

Figure 4.6: On the left, picture of the boards used for irradiation and annealing campaign. On the right is a close view of one board of SiPM. Each board hosts up to 32 sensors of $3 \times 3\,\mathrm{mm}^2$ area.

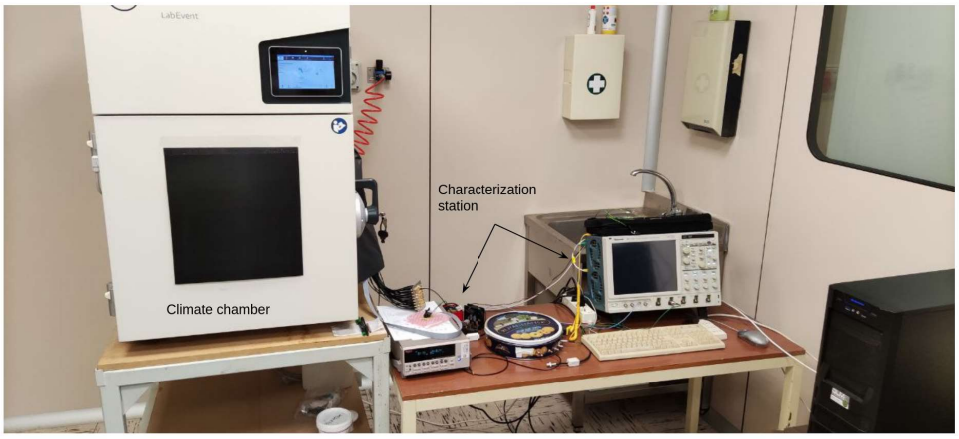

Figure 4.7: The climate chamber and the characterization station used to test the SiPMs in the clean room at INFN Ferrara.

radiation dose. There is a linear increase of current with respect to the dose. The first annealing test was performed using an oven, which is shown in Figure 4.9, and with a staged temperature increase, carrying out various sensor characterizations between each phase of $\sim 50\,\mathrm{h}$ annealing time. The results of these measurements are reported in Figure 4.10, which shows the value of the DCR during this long annealing period compared with the results of Reference [53]. In the legend of this plot, the label "Hama" indicates one of the SiPM by Hamamatsu tested by the author, "C" and "D" identify the row of the board, i.e. the size of the sipm pixel, "3" and "4" identify the column of the board, i.e. the radiation dose received of 10^{10} or $10^{11}\,\mathrm{n_{cq}}$ respectively. The label "Milano" identifies the curves taken from the Reference paper [53] for different doses of irradiation. The vertical lines show the time then the temperature was changed and the value of the temperature itself. The points conventionally placed at $-100\,\mathrm{h}$ represent the DCR before the irradiation at Trento.

The SiPMs tested in Ferrara showed the same behavior as the reference results, confirming a curing factor ~ 20 during the annealing. The systematic comparison of the annealing effect on different sensors is shown in Figure 4.11. It can be noted that the Hamamatsu S13360-3050VS features the lowest DCR before the irradiation and before and after the annealing, which makes it the most promising candidate to be used for the dRICH detector.

After the start of ePIC operation, removing the sensors from the detector for the required annealing cycles in the oven will be very complex. So, preliminary tests of online in-situ annealing made directly polarizing the SiPM are being performed. The online procedure consists of cycles of 30 min at high temperature (up to $175\,^{\circ}\mathrm{C}$) each time the sensor received an integrated dose of $2 \times 10^8\,\mathrm{n_{eq}}$. The sensor's temperature should not overcome the value of $180\,^{\circ}\mathrm{C}$, which is the choosen operating limit to preserve the entrance window protective layer and was kept under control using a thermal camera, as shown in Figure 4.12a. The comparison between the oven and the online annealing is reported in Figure 4.12b and shows that the online annealing permits a rapid reduction of the DCR by one order of magnitude. The oven annealing performance is better by a factor of 2, but the online procedure has several advantages:

- it is ~ 100 times faster;
- it can be done in-situ, without removing the sensor from the detector;
- it can be repeated many times.

Consequently, the final design of the dRICH detector will probably account for several online annealing phases and, at most, few extraordinary maintenance operations when sensors are removed for long annealing in the oven.

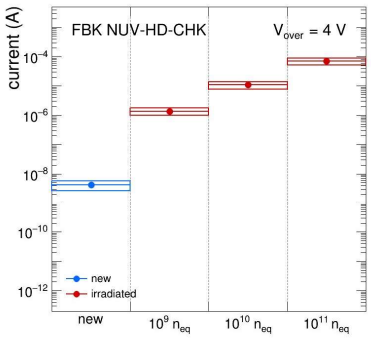

(a) Dark current of a SiPM as a function of the irradiation dose received. It increases linearly with the dose. Plot taken from Reference [54]

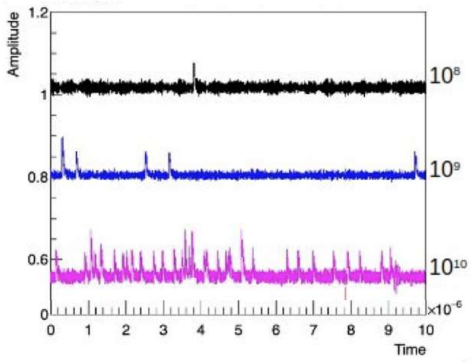

(b) Snapshot of the signal of SiPMs which received a different dose of radiation. Each spike corresponds to at least one photo-electron contributing to the dark count. Clearly, increasing the dose leads to larger DCR.

Figure 4.8: Effects of the irradiation on dark current and DCR.

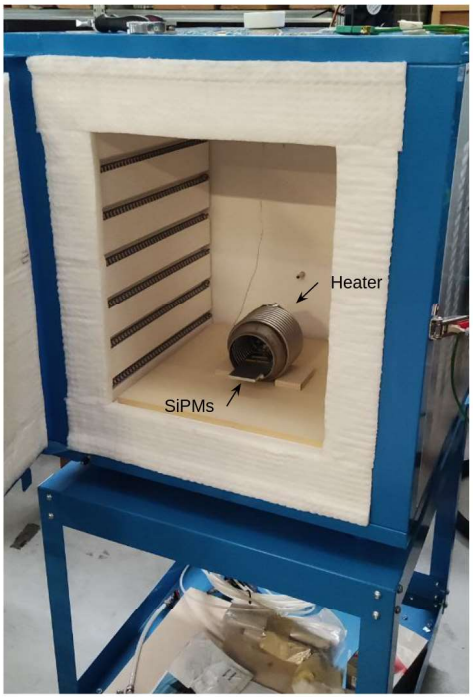

Figure 4.9: The oven used to perform the first annealing in the laboratory of INFN Ferrara.

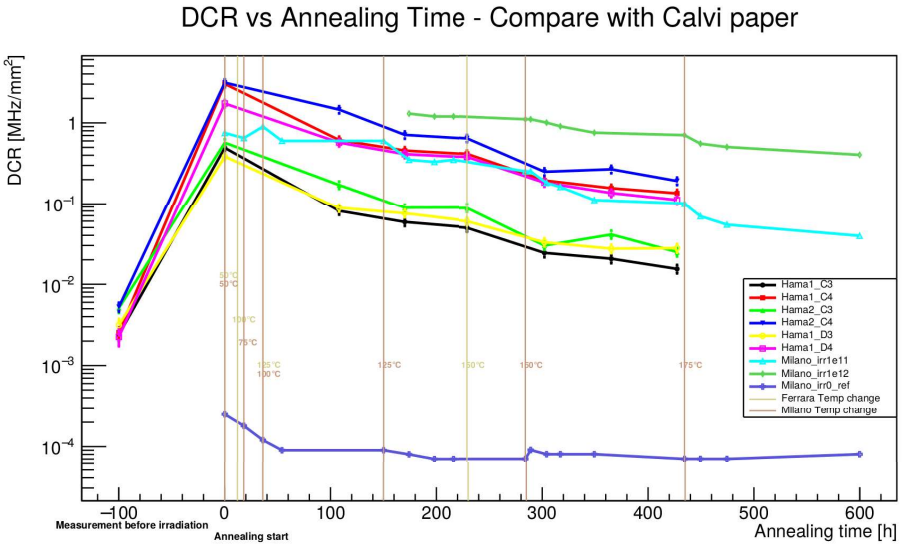

Figure 4.10: Results of the first annealing test using the Ferrara oven and characterization test. The results are compared with Reference [53]. See the text for an explanation.

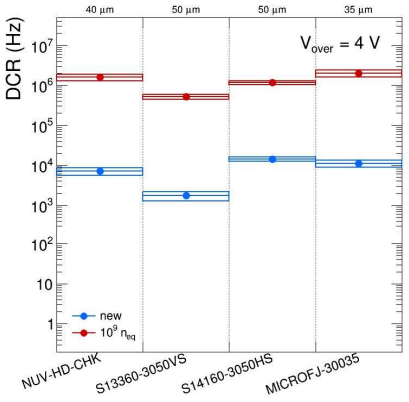

(a) Dark count rate measured for different sensors when they were new and before the annealing).

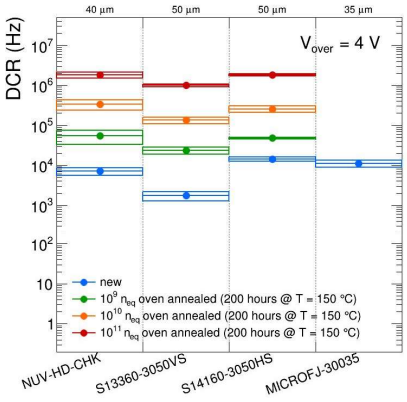

(b) Dark count rate measured for different sensors and different irradiation dose after 200 h of annealing at 150 °C.

Figure 4.11: Results of irradiation and annealing on different sensors, from Reference [54]

(a) Picture of the thermal camera measuring the directly polarized SiPM. The sensor can reach more than 175 °C, but has not to overcome the value of 180 °C.

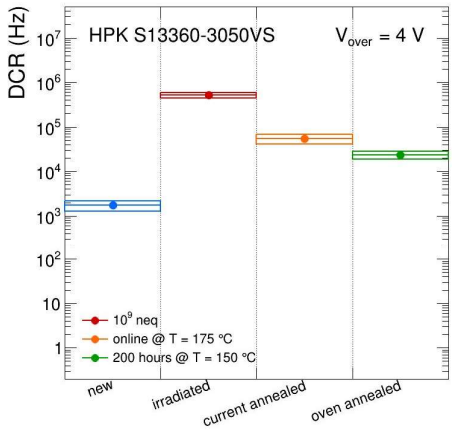

(b) Comparison of the dark count rate measured for the same kind of sensor applying 30 min online ("current") or 200 h oven annealing.

Figure 4.12: Temperature control during the online annealing and results of the annealing performed through the direct polarization of the sensors. Images taken from Reference [54]

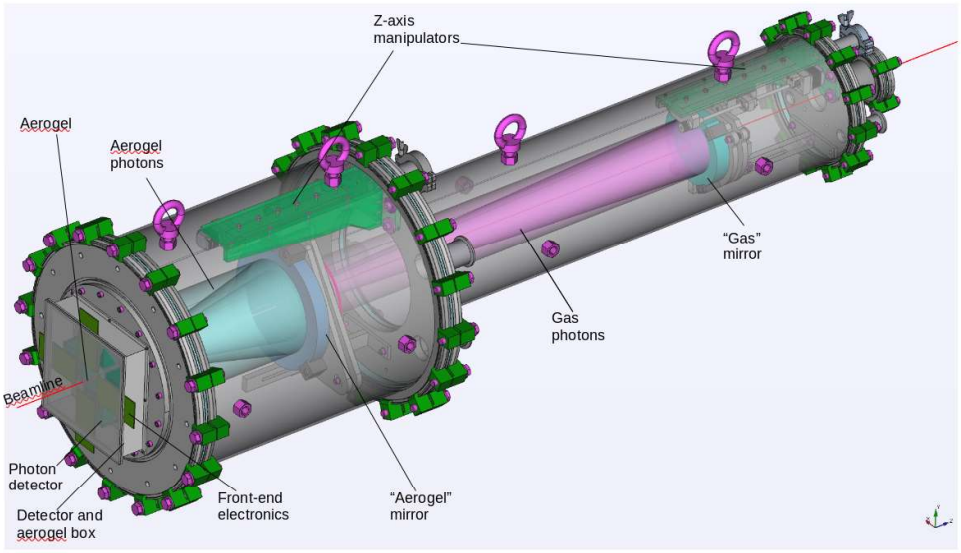

Figure 4.13: dRICH prototype scheme.

4.3 The dual-radiator RICH prototype

A prototype [56] of the dRICH detector was built in Ferrara in the summer of 2021, aiming to serve several test beams in the following years. On a lower scale, it reproduces the expected behavior of the entire dRICH detector. It was used to test the hadron separation capabilities that can be achieved with different options and quality of the components.

4.3.1 Design

A scheme of the prototype is reported in Figure 4.13. A charged particle crossing the prototype from left to right starts passing through the aerogel ($n \simeq 1.02$), producing a Cherenkov-photon cone with an aperture of about 11 °. The photons are reflected by a first spherical mirror and focused on the photon detector array. Then, the particle passes through the gas ($n \simeq 1.00085$), which fills the detector volume and produces a Cherenkov-photon cone with an aperture of about 2 °. The first mirror has a central hole to allow the photons produced at small angles in the gas to fly towards a second spherical mirror and be focused back on the same photon detector array. The information from the two imaged Cherenkov rings, combined with the beam momentum and particle tagging provided by the beam instrumentation, is used to study the dRICH identification of pions, kaons, and protons in the momentum range from 3 GeV/c up to 50 GeV/c.

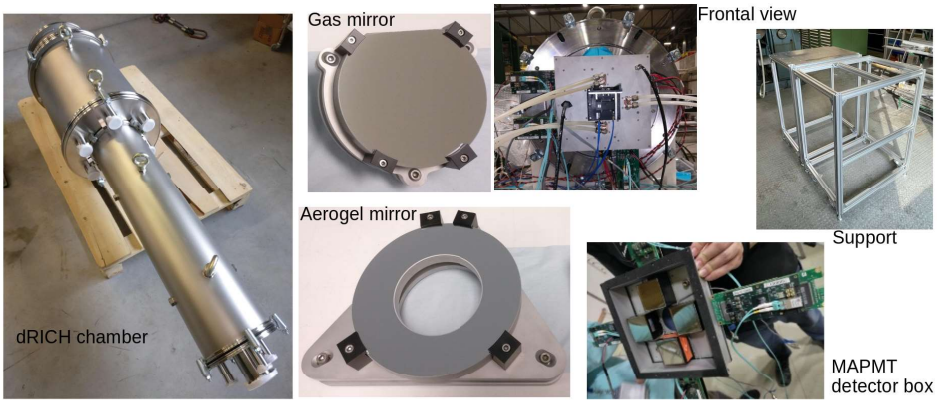

Figure 4.14: Collection of pictures of the prototype components

Mechanical structure

The dRICH is 1.3 m long and is composed of two sections: a 50 cm long cylinder with a 50 cm diameter and a 80 cm long extension with a 25 cm diameter. This volume, called the "gas chamber", is filled with the C_2F_6 radiator gas. It has to bear under-pressurization (vacuum), allowing efficient exchange between air and the gaseous radiator, and preserve light tightness, allowing the single-photon operation mode of photo-sensors. Moreover, it includes the mechanics for regulating the angle and position of the mirrors along the detector axis. The radius of curvature of each mirror was designed to collect the light produced over the full radiator length and focus it onto the detector surface. The mechanical support of each mirror can be pre-aligned using three different screws and, without opening the detector, can be moved along the detector axis using a step motor to finely regulate the focus position. A series of pictures of the dRICH components is shown in Figure 4.14.

Detector box

In front of the prototype is the detector box, which hosts the photosensors with their sensitive faces pointed forward and separated from the gas volume by a 3-mm-thick acrylic window. For the prototype, three different kinds of detector boxes were used:

- The MAPMT box hosts four Multi-Anode Photomultiplier Tubes Hamamatsu H12700 (the same as the CLAS12 RICH), set as reference detectors to study the prototype's performance;

- The MPPC box hosts three Multi-Pixel Photon Counters, matrices of SiPMs used during the first test beams as preliminary detectors to study the silicon-based sensors and their cooling system;

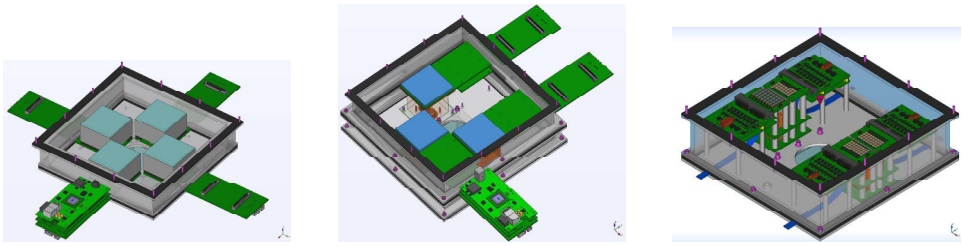

(a) MAPMT detector box. **(b)** MPPC detector box. **(c)** SiPM detector box.

Figure 4.15: Drawing of the three detector boxes.

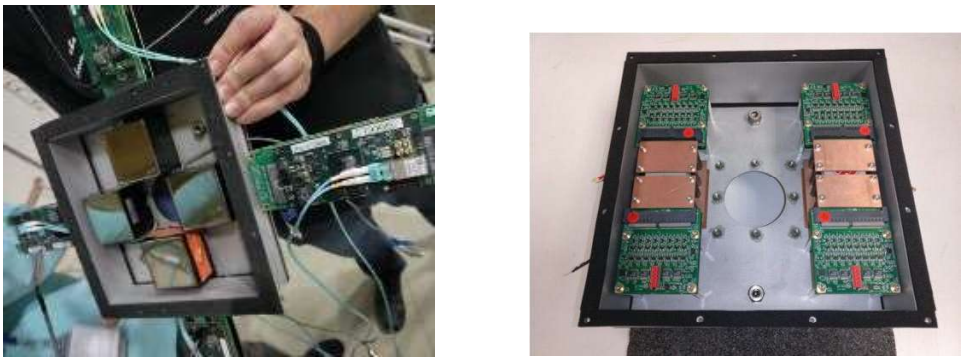

Figure 4.16: Pictures of the MAPMT (left) and the first version of SiPM (right) detector boxes.

- The SiPM box hosts custom matrices of various Silicon Photomultipliers (undergoing irradiation and annealing cycles) to evaluate the most suitable sensor for the EIC dRICH detector;

The detector boxes are sketched in Figure 4.15, and two pictures are in Figure 4.16. The data of the MAPMT and MPPC detector boxes are acquired using the Multi-Anode ReadOut Chip (MAROC) as done for the CLAS12 RICH. Instead, for the SiPM detector box, a streaming readout system based on A Low Power Chip for Optical Sensor Readout (ALCOR) was tested. Initially, the SiPM box was designed to host four small custom matrices used to study the annealing procedure. In the last version, it was modified to host up to 8 photon detection units for a total of 2048 readout channels, made following the current design of the dRICH detector and covering almost the entire ring.

Aerogel box

The aerogel box completes the mechanical structure. It is a 3D-printed black box containing the aerogel radiator placed upstream of the detector box on the beamline. Black rubber is used to seal the aerogel box to the detector box, preventing light leaks and creating a single volume filled with nitrogen

to avoid moisture. The box permits operation in the ePIC configuration with a 4-cm-thick layer of aerogel, but also to test other configurations with 2-cm or 6-cm-thick layers of aerogel.

Radiators

The nominal radiators are the C_2F_6 gas and the aerogel, with refractive index $\simeq 1.00085$ and $\simeq 1.02$, respectively. They present different challenges:

- C_2F_6 is a greenhouse gas, so its use is critical from the point of view of respecting the environment. For the prototype, the relatively small volume allows the use of a simplified recovering system. For the final detector, dedicated special recovery systems are foreseen. Solutions based on the use of pressurized noble gases or alternative gas mixtures are also being studied.

- Silica aerogel is a fragile material and not easy to handle, but in the group working on the dRICH, there is enough experience. The main issue regards the aerogel manufacturer. One of the most commonly used, the Budker and Boreskov Institute of Nuclear Physics (Russia); delivered the aerogel for the CLAS12, LHCb, HERMES and AMS-02 experiments. The invasion of Ukraine introduced insurmountable complications in dealing with this manufacturer. At the moment of writing this document, the candidate supplier is Aerogel Factory Co. [57], a new producer that emerged in 2021 as a spin-off of the Belle-II aerogel development at Chiba University, Japan. They declare the capability of producing aerogel in a wide range of refractive index, from 1.003 to 1.18, and are able to realize samples of good optical quality, which makes them a credible option for producing dRICH aerogel. Because there are different methods to produce aerogel, its properties can be very different, even slightly changing the refractive index. This makes necessary to conduct careful tests before deciding on the producer and take care to characterize each optical property.

This thesis deals with the Cherenkov angle resolution achieved with gas and aerogel radiators, but more attention is paid to aerogel because the author was mainly involved in its study. To evaluate the aerogel produced by the Aerogel Factory Co., several samples were characterized in the laboratory of INFN Ferrara group and tested using the prototype at CERN.

4.3.2 Aerogel characterization

Transmittance analysis

Table 4.1 reports a recap of the aerogel tiles studied. A Perkin Elmer UV/VIS spectrophotometer Lambda 650S was used to characterize the aerogel. The

Tile ID	Producer	Production year	Refractive index		Side [mm]	Width [mm]
			Nominal	Measured		
TSA2-1a	Japanese	2021	1.020	1.0206	50	20.5
TSA1-2b	Japanese	2021	1.020	1.0206	50	20.8
TSA1-3b	Japanese	2021	1.020	1.0199	50	20.8
TSA2-4a	Japanese	2021	1.020	1.0204	50	20.8
TSA3-1a	Japanese	2021	1.030	1.0301	90	21.1
TSA3-2a	Japanese	2021	1.030	1.0303	90	21.0
TSA3-3a	Japanese	2021	1.030	1.0304	90	21.3
TSA3-3b	Japanese	2021	1.030	1.0304	90	21.1
AG22J001	Japanese	2022	1.020	1.0210	50	20.5
AG22J002	Japanese	2022	1.020	1.0201	50	20.6
AG22J003	Japanese	2022	1.020	1.0207	50	20.4
AG22J004	Japanese	2022	1.020	1.0218	50	19.5
AG22J005	Japanese	2022	1.015	1.0152	50	19.9
AG22J006	Japanese	2022	1.015	1.0158	50	21.7
AG22J007	Japanese	2022	1.015	1.0158	50	21.4
AG22J008	Japanese	2022	1.015	1.0158	50	21.4
AG22J009	Japanese	2022	1.024	1.0260	50	21.3
AG22J010	Japanese	2022	1.024	1.0261	50	21.2
AG22J011	Japanese	2022	1.024	1.0232	50	19.1
AG22J012	Japanese	2022	1.024	1.0232	50	19.4
AG22J013	Japanese	2022	1.020	1.0205	110	20.3
AG22J014	Japanese	2022	1.020	1.0208	110	20.3
AG22J015	Japanese	2022	1.020	1.0208	110	20.4
AG22J016	Japanese	2022	1.020	1.0207	110	19.7

Table 4.1: Recap of the aerogel tiles tested using the prototype. The values of the measured refractive index were provided by the producer. If the ID reported is **bold**, the correspondent tile was used to form a 4-cm-thick layer of aerogel in the prototype measurement.

spectrophotometer measures the transmittance of the sample as a function of the photon wavelength. The transmittance was analyzed using the extended Hunt formula [58]

$$T(\lambda) = e^{-\frac{t}{\Lambda_T}} = e^{-t\left(\frac{1}{\Lambda_A}+\frac{1}{\Lambda_S}\right)} = Ae^{-\frac{Bt}{\lambda^8}}e^{-\frac{Ct}{\lambda^4}} \tag{4.1}$$

where T is the transmittance, t is the sample thickness, λ is the wavelength of the light, $\Lambda_{A,S}$ are respectively the Absorpion and Scattering length, and A, B, and C are fit parameters, the latter called Clarity. An example of fitted transmittance is reported in Figure 4.17. From this formula, it is possible to obtain the values of absorption and scattering length

$$\Lambda_S = \frac{\lambda^4}{C} \tag{4.2}$$

and

$$\Lambda_A = \frac{\lambda^8 t}{Bt - \lambda \cdot \ln A}. \tag{4.3}$$

The total transmission length is defined as

$$\frac{1}{\Lambda_T} = \frac{1}{\Lambda_A} + \frac{1}{\Lambda_S} \tag{4.4}$$

The main results are shown in Figures 4.18, 4.19, 4.20, 4.21, and 4.22. The first plot reports the nominal and measured refractive index; both were provided by the producer (and the precise numerical values are reported in Table 4.1). The second shows the mass density of the tiles as a function of the refractive index; clearly, there is a linear relation between them. The third shows the absorption length, which is not uniform for different tiles with the same refractive index. Such a variation is not critical because the absorption length is at least one order of magnitude longer than the scattering length, and then it has a second-order effect on the total transmission length. The last two plots describe the scattering and total transmission length, showing an almost linear correlation with the refractive index. This relation implies that in the studied range around the ePIC nominal refractive index, aerogel with a larger refractive index will have a larger yield of photons and better optical quality, and should result in a better single-particle resolution.

Not all the tiles characterized can be studied with the existing dRICH prototype. Indeed, the aperture of the Cherenkov cone produced by tiles with $n = 1.03$ is larger than the mirror acceptance, and the photons are not reflected onto the photo-detector. In addition, an aerogel with $n = 1.03$ has a poor momentum overlap with the gas radiator and is not suitable for the dRICH. The aerogel study is therefore limited to $n = 1.026$. The characterization results are used in the process of selecting the most uniform pairs of aerogel tiles to be tested with the prototype, in the anticipated ePIC configuration with a 4-cm-thick aerogel layer, corresponding to two stacked

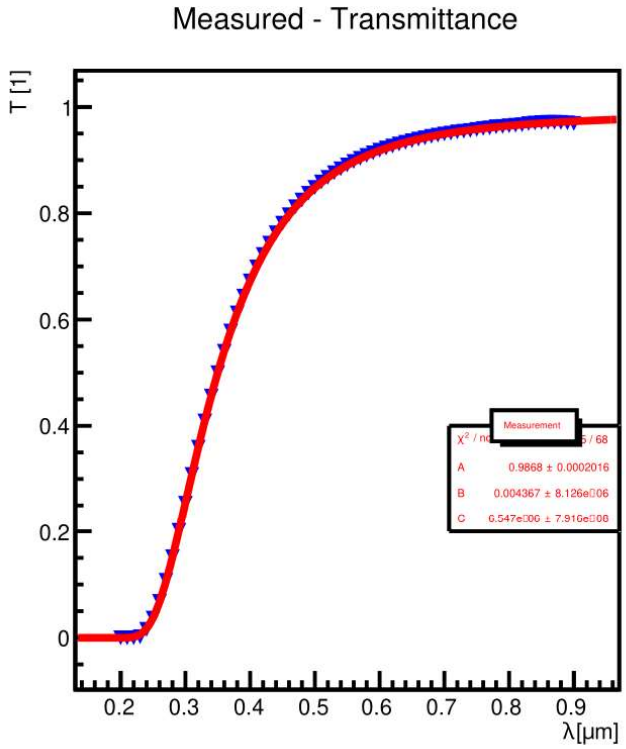

Figure 4.17: Measured transmittance (blue arrows) fitted using the extended Hunt formula (red).

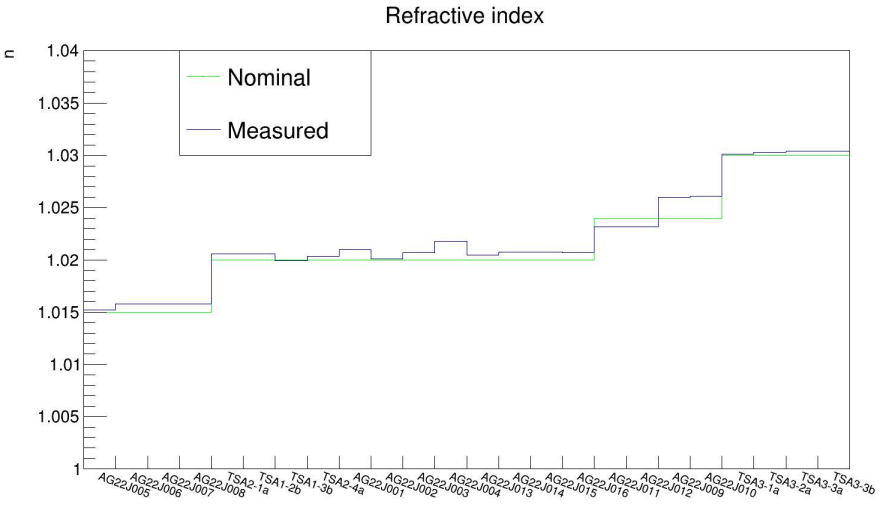

Figure 4.18: Refractive index of the aerogel tiles.

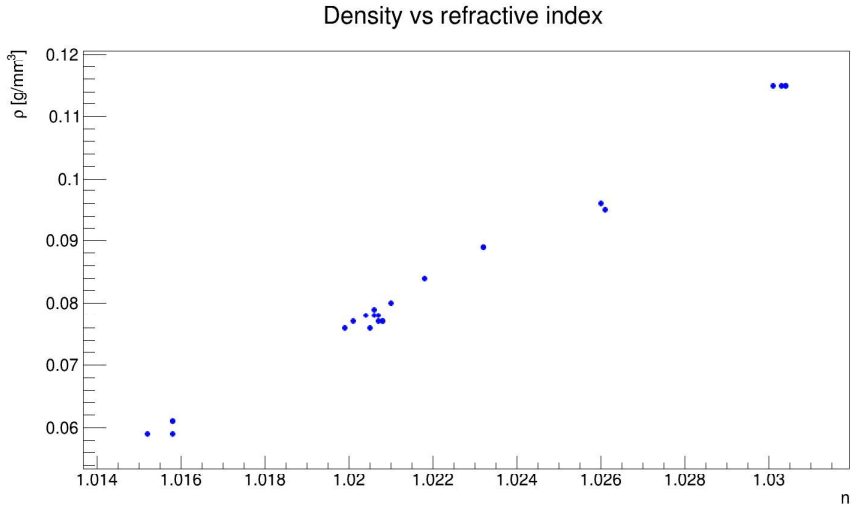

Figure 4.19: Density of the aerogel tiles versus the refractive index.

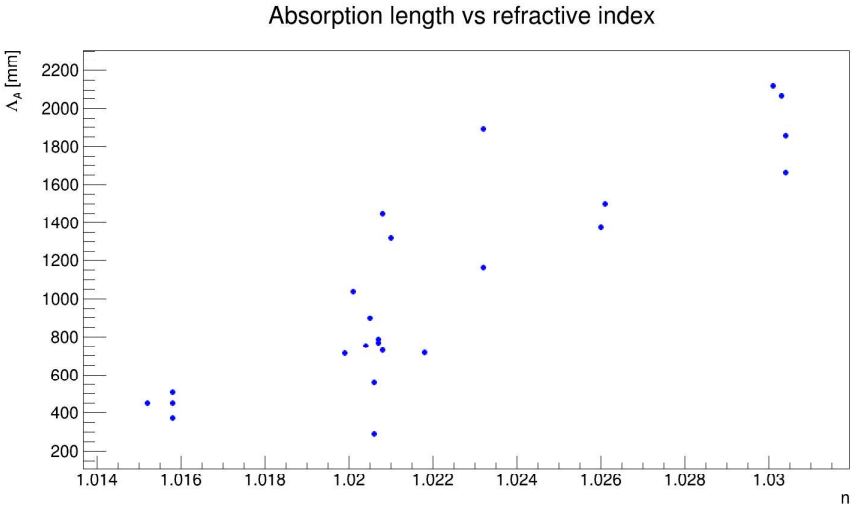

Figure 4.20: Absorption length of the aerogel tiles versus the refractive index.

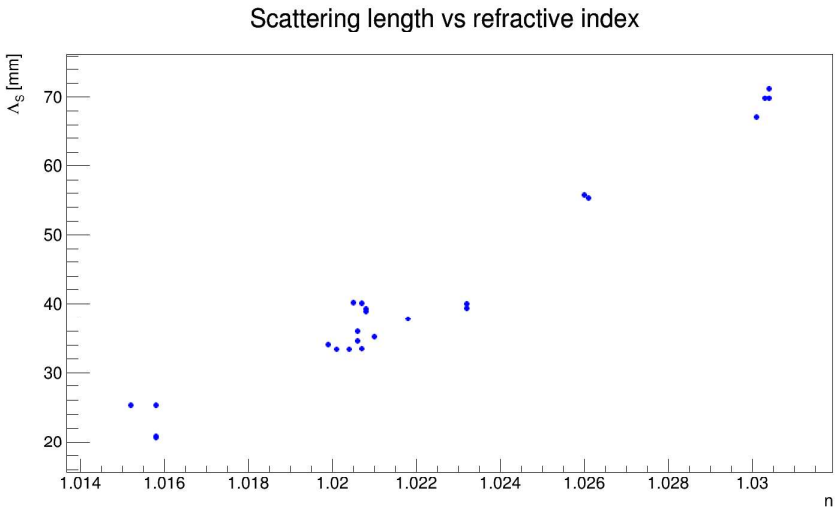

Figure 4.21: Scattering length of the aerogel tiles versus the refractive index.

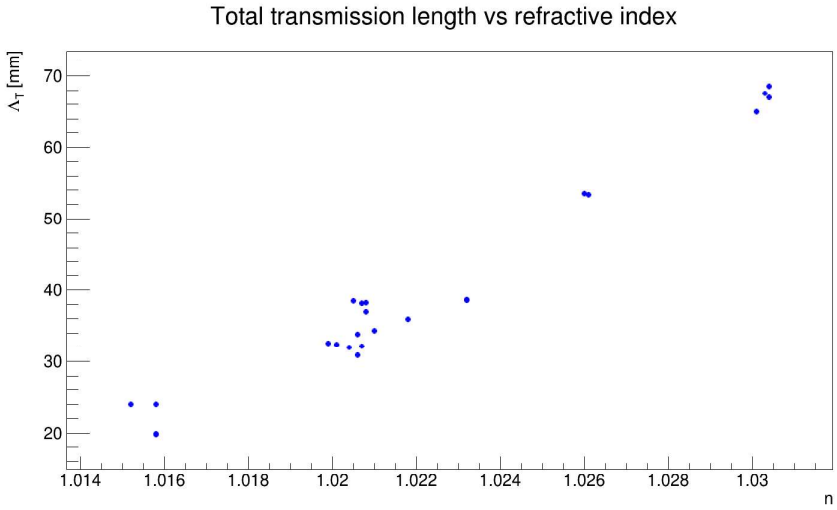

Figure 4.22: Total transmission length of the aerogel tiles versus the refractive index.

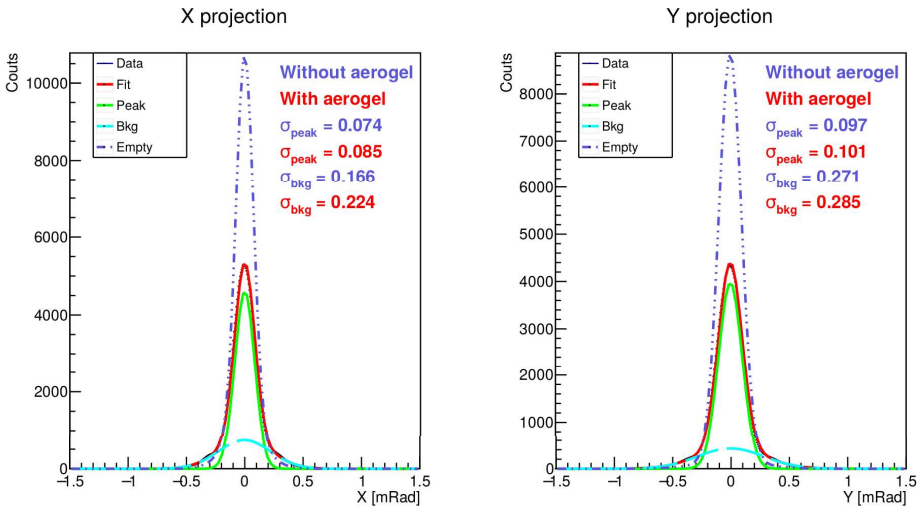

Figure 4.23: One-dimensional projection of the beam spot along x (left) and y (right) directions. In addition to the fit (red) and the two Gaussians (laser peak in green and halo in light blue), the curve of data without aerogel (dot-dashed blue) is reported.

tiles. The final selection was based on the uniformity of the refractive index and maximization of the total transmission length. These conditions led to the definition of the pair of tiles for each nominal refractive index to be used during the test beams with the prototype. The selected tiles are highlighted in bold characters in Table 4.1.

Forward scattering measurement

Local inhomogeneities in the aerogel density or its micro-structure can affect the light propagation in the aerogel volume. This effect can be studied with the enlargement of a laser beam spot passing through the aerogel sample, a phenomenon called forward scattering. It was studied by sending an attenuated laser beam through the sample directly to a CCD sensor, and acquired the beam spot for a grid of points along the aerogel surface. The comparison with the reference spot in the absence of the aerogel allowed the evaluation of the forward scattering. The analysis was conducted using the one-dimensional projection of the beam spot along the axes. These projections were fitted by a sum of two Gaussian functions associated with the laser spot and its halo. From plots in Figure 4.23, showing the mean of all the measurements compared with the reference curve, it is deducible that the forward scattering has a second-order effect on the laser spot.

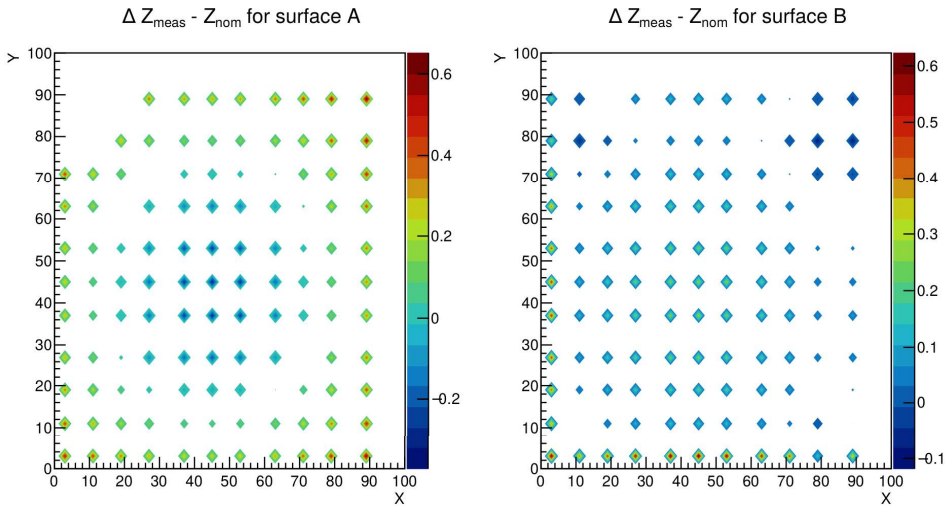

Figure 4.24: Difference between the measured thickness of aerogel and the nominal expectation. The left and right plots show the two faces of the same tile.

Aerogel metrology

Another step of the characterization is the measurement of the size of the aerogel tile, in particular thickness and planarity. The measurement was performed by the mechanical workshop of the INFN Ferrara and analyzed by the author. The result is shown in Figure 4.24. The distribution of the two faces of the same tile shows that one is concave and the other convex. This fact can explain the reason of a systematic difference in the Cherenkov angle values and resolutions obtained by swapping the exit surface (by an 180° rotation) of the aerogel tile. The plots showing the systematic differences are reported in Figure 4.25 and 4.26.

4.3.3 Simulation

For the ePIC dRICH, to achieve the requirements of a 3σ separation between pion and kaon in the high-momentum region, a resolution on the single-particle mean Cherenkov angle of 0.8 mRad for aerogel and 0.3 mRad for gas is needed. These requirements are taken from the dedicated talk at the last ePIC collaboration meeting, Reference [59]. The plots allowing to obtain these values are reported in Figure 4.27.

A simulation was developed using GEant4 Monte-Carlo (GEMC) [60, 61], a framework dedicated to the simulation of low and medium-energy particle physics, to evaluate the performance achievable with the dRICH prototype. A relatively simple model of the prototype was implemented using CAD drawings of the main elements and textual implementation of their physical

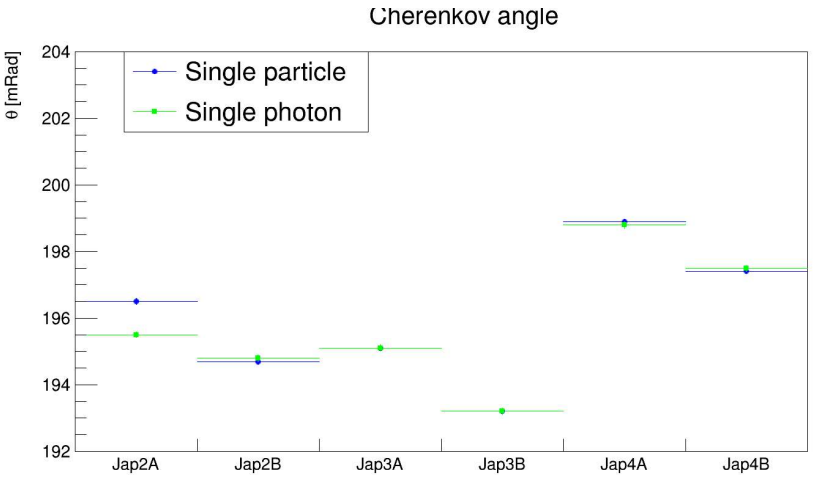

Figure 4.25: Cherenkov angle measured for different aerogel tiles with nominally the same refractive index. The letters A and B identify the selected entry face of the tile. Moving from side A to B results in a Cherenkov angle smaller by $\sim 2\,\mathrm{mRad}$.

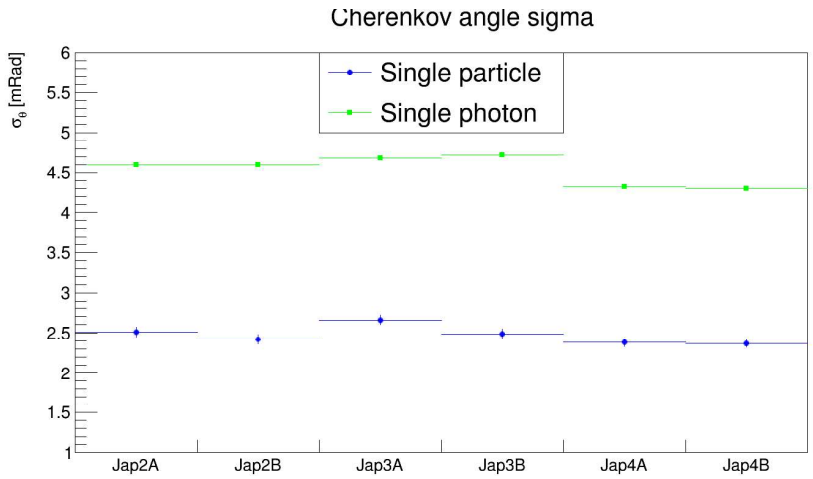

Figure 4.26: Resolution on the Cherenkov angle measured for different aerogel tiles with nominally the same refractive index. The letters A and B identify the selected entry face of the tile. Moving from side A to B results in obtaining the same or smaller resolution.

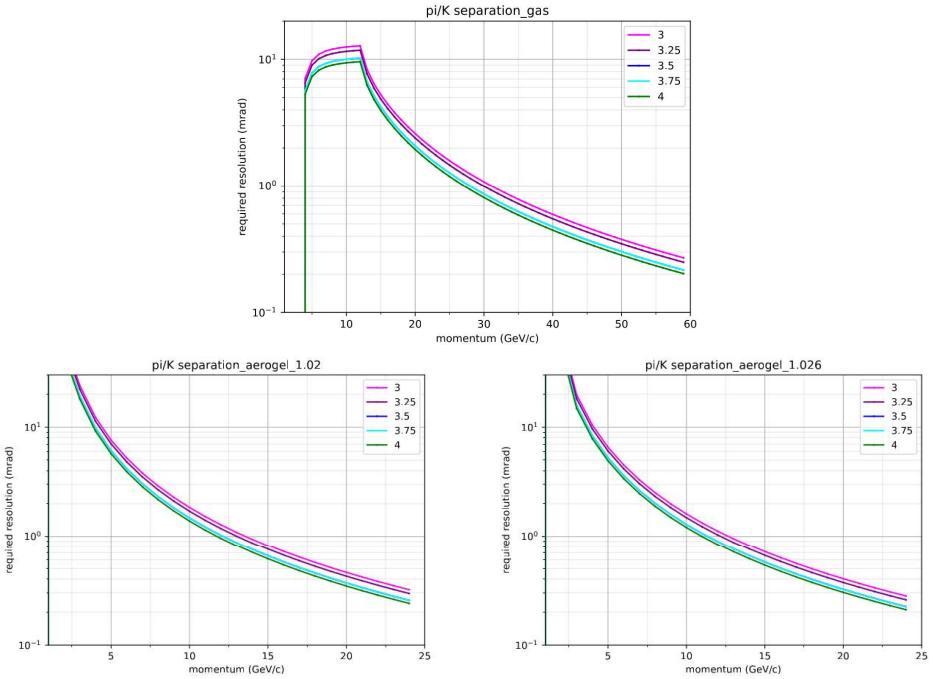

Figure 4.27: Plots of the single-particle Cherenkov angle resolution needed for the dRICH to achieve the required resolution of at least 3σ in the wanted momentum range, up to 50 GeV/c. The plots are taken from Reference [59].

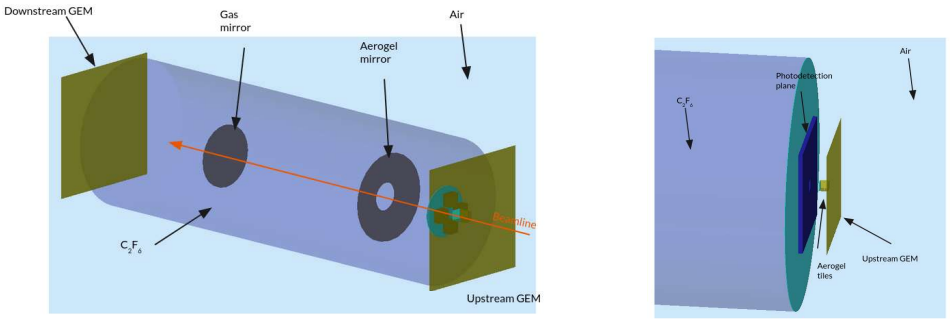

(a) Prototype simulation, full view

(b) Prototype simulation, detailed aerogel and photodetection area view

Figure 4.28: Prototype simulation draws.

properties (material, density) and optical properties like reflectivity (mirrors), Rayleigh scattering, refractive index, and total transmission length (aerogel and gas). The photo-detectors were simulated as a solid plane absorbing all the photons in a thin thickness; the effects of quantum efficiency and pixelation were applied during the analysis. The elements of the prototype model are shown in Figure 4.28. In addition to the main components of the dRICH, the simulation model includes two objects representing the GEM detectors composing the tracking system employed at the test beams. This model was used during the design phase to establish the value of some important parameters, like the curvature radius of the mirrors, and for the preliminary evaluation of the expected Chernkov angle resolution achievable with the prototype. The expected mean Cherenkov angle obtained from simulation as a function of the hadron momentum is shown in Figure 4.29. In the plot, the momentum regions needing the two radiators are highlighted.

The initial simulation did not perfectly reproduce the prototype; for example, the simulated beam was punctiform and with no divergence, or the background was negligible with respect to the real case. Thus, the results provided by the prototype simulation were too optimistic. Lately, the complete ePIC simulation was used to evaluate the Cherenkov angle resolution achievable by the prototype. It is based on the different contributions of the several error sources in a RICH detector:

- Pixel error, caused by the information loss due to the finite dimension of the photo-sensors pixel;
- Chromatic error, due to the dependence of the refractive index on the photon wavelength;
- Emission error, due to the uncertainty of the Cherenkov photon emission position inside the radiator;

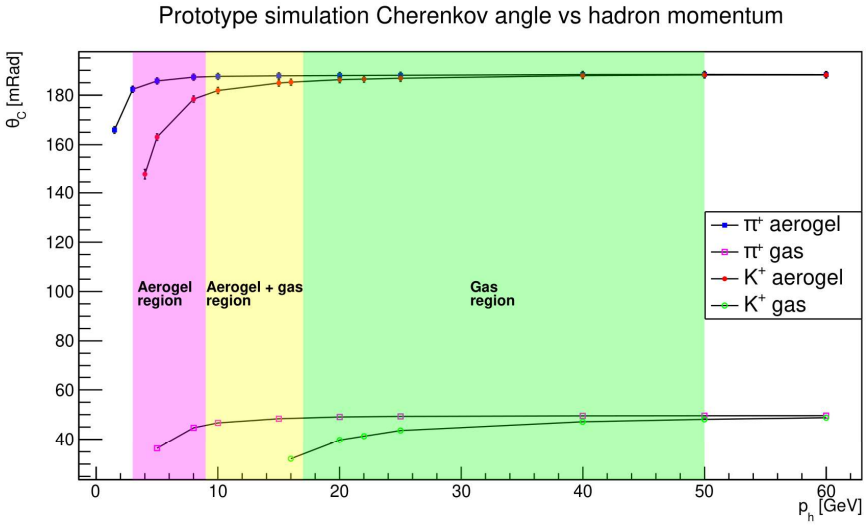

Figure 4.29: single-particle mean Cherenkov angle obtained from the simulation as a function of the hadron momentum, for positive pion and kaon. The error on the resolution was derived from Table in Figure 4.2. The magenta, yellow, and green areas highlight the region where the different radiators can be used to identify the particle.

- Tracking error, due to the global uncertainty associated with the track of the charged particle passing through the detector that accounts for the bending inside the radiator volume.

The values of these contributions can be found in Figure 4.30. It reports the estimated contributions to the Single PhotoElectron (SPE) resolution for the two radiators, divided into "Demo" (meaning prototype) and dRICH. The main difference between detector and prototype regards the contribution of the pixel error for aerogel. Indeed, in the dRICH the distance between aerogel and mirror is $\sim 1.2\,\mathrm{m}$, while for the prototype is $\sim 0.4\,\mathrm{m}$. It makes the relative uncertainty on the Cherenkov angle caused by the uncertainty on the photon hit position more relevant for the prototype.

According to the Table in Figure 4.30, for the ePIC dRICH, the expected SPE resolution are 2.3 mRad for aerogel and 1.0 mRad for gas. For the prototype, they are 3.0 mRad for aerogel and 1.1 mRad for gas. From SPE resolution, it is possible to obtain the resolution on the single-particle mean Cherenkov angle as

$$\sigma_{sing\_part} = \sqrt{\left(\frac{\sigma_{SPE}}{\sqrt{N_{photons}}}\right)^2 + c_0^2} \tag{4.5}$$

where $N_{photons}$ is the number of photons detected per particle and c_0 is a possible systematic constant contribution to the resolution. In the following

1 p.e. error (mrad)		Aerogel		Gas	
		Demo	dRICH	Demo	dRICH
Pixel	(3mm pixel)	1.9	(0.6)	0.6	(0.5)
Chromatic	(300 nm filter)	1.8	(2.2)	0.6	(0.5)
Emission	(1 cm out of focus)	0.3	(0.3)	0.4	(0.6)
Tracking	(0.5 mrad)	0.4	(0.3)	0.4	(0.4)
Total		3.0	(2.3)	1.1	(1.0)

Figure 4.30: Table of the different contributions to the Cherenkov angle resolution. The values in the "demo" columns are theoretical estimations for the prototype, while the dRICH column is associated with the detector. The main difference regards the pixel effects for the aerogel because, in the prototype, the aerogel photons have to travel along a shorter path to fit into the limited active area.

	Aerogel	Gas
σ_{SPE} [mRad]	3.0	1.1
σ_{sing_part} [mRad]	1.3	0.25
$N_{photons}$	5.4	20

Table 4.2: Recap of the SPE and single-particle resolutions achievable according the simulation.

is described that from the prototype test, a non-zero constant term ($\sim$ 0.25 mRad) emerged for the gas section, while the same was compatible with zero for the aerogel. The expected number of photons per particle was taken by the prototype simulation because it better described the complex geometry with two different mirrors and the MAPMT used reference detectors, in particular their quantum efficiency different from SiPM. The number of photons per particle expected is 5.4 for aerogel and 20 for gas.

The evaluation of the prototype performance will be made by comparing the resolution achieved during the test beams with the values described in the last paragraph. A recap is contained in Table 4.2.

4.3.4 Test beams

The prototype was tested in several test beams at the European Council for Nuclear Research (CERN) between 2021 and 2023 using the experimental halls available at Proton Synchrotron (PS) and Super Proton Synchrotron (SPS), accelerators providing beams of charged mixed hadrons, respectively, with momentum up to 11.5 GeV and up to 200 GeV. Aiming the dRICH to distinguish particles with momentum up to 50 GeV and having the aerogel a refractive index larger than the C_2F_6 one, the test beams goals were:

(a) Picture of the photo-detector side of the SiPM detector box.

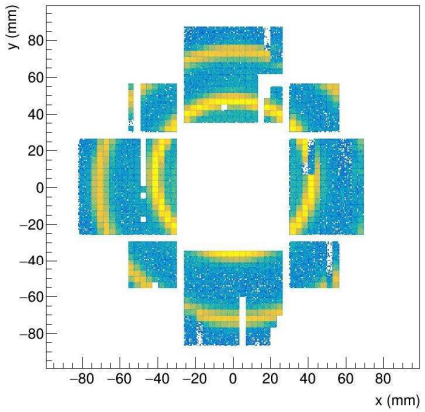

(b) The two rings obtained in the last test beam using the SiPM detector box.

Figure 4.31: The latest version of the SiPM detector box includes 4 readout units with 256 sensors and 4 readout units with 64 sensors for a total of 1280 readout channels.. It allows the detection of almost the whole two rings, both from aerogel and gas.

- on both the experimental location, to perform studies on several aerogel tiles with different refractive index and stack compositions, applying wavelength filters and exploiting the Cherenkov threshold detectors of the beam to identify particles of different species with the dRICH;

- at PS, study the momentum interval common to the two radiators with a beam extended in space and divergence;

- At SPS, to measure the resolution with saturated rings and well-collimated particles.

The test beams performed over almost 3 years were instrumental to the progressive evolution of the prototype technology and performance. During the first test beam in 2021, the dRICH prototype was successfully commissioned and the SiPM detector box was used mainly to operate the photosensors, their cooling system, and the data acquisition chain. In the 2023 Fall test beam, the latest version of the SiPM detector box, represented in Figure 4.31a, allowed to obtain the first almost complete imaging of the double-ring of photons with a ePIC driven readout plane, as shown in Figure 4.31b.

The MAPMT detector box was used during all the test beams to measure the prototype's performance and map the achievable resolution of aerogel and gas Cherenkov angles. The following sections will present the analysis developed and the results obtained.

Experimental setup

The test beam setup included a tracking system, a trigger apparatus, and external PID detectors from beam instrumentation; a picture of this is shown in Figure 4.32. The tracking is based on two Gas Electron Multiplier (GEM) detectors placed upstream and downstream of the dRICH. The GEM detects the position in which the beam crosses it, and the coincidence of the signals from the two detectors is used to find the track of the particle with a resolution better than 100 µm. The GEMs were a smaller version of those described in the Reference [62]. The GEMs had their power supplies providing high ($\sim 4\,\mathrm{kV}$) and low voltage, front-end boards, and data acquisition software; the author developed his expertise in operating the tracking system and became the expert-on-call since the 2022 test beams.

The trigger system was based on four finger scintillators measuring an area of $2 \times 1\,\mathrm{cm}^2$ each, two placed in front of the aerogel box and two just downstream of the prototype, and read with SiPMs. The components of each pair of scintillators work in coincidence to avoid random triggers. The logical AND and OR of the scintillator pairs were available for the trigger and could be selected from the control room without accessing the experimental hall. Being the GEMs' readout slower than the MAPMTs' readout, a busy signal was used to veto new triggers until GEMs were ready to acquire. This configuration allows the offline pairing of the track with the corresponding dRICH event.

Figure 4.33 reports the plots relative to the tracking system from two runs acquired at the two accelerators, showing clear differences. The beam profile and the divergence of the SPS beam are smaller than the PS beam. At PS, the coincidence with the trigger scintillators is also used to limit the beam profile, which could also be larger than the one shown in Figure 4.33b; instead, at SPS, the beam spot is smaller than the area covered by the trigger system.

The test beam setup included an external PID apparatus consisting of two (at PS) or three (at SPS) gaseous threshold Cherenkov detectors. They can host various gases and adjust the inner pressure, modifying the refractive index. This procedure permits setting a threshold for the mass of the particles producing the Cherenkov photons for a given beam momentum. Particles lighter than the threshold will produce light inside the detector, while heavier particles will not. Combining the information from various detectors with different settings makes it possible to tag different species of particles. For example, a detector activation scheme for the PS is reported in Table 4.3. The signals provided by the trigger signal and the beam Cherenkov were read using a special adapter board coupling them to the MAROC, the same readout of the MAPMT. This allowed us to handle them easily with the same data acquisition software as the photo-detector signals.

The MAPMT box design supports two different configurations, called

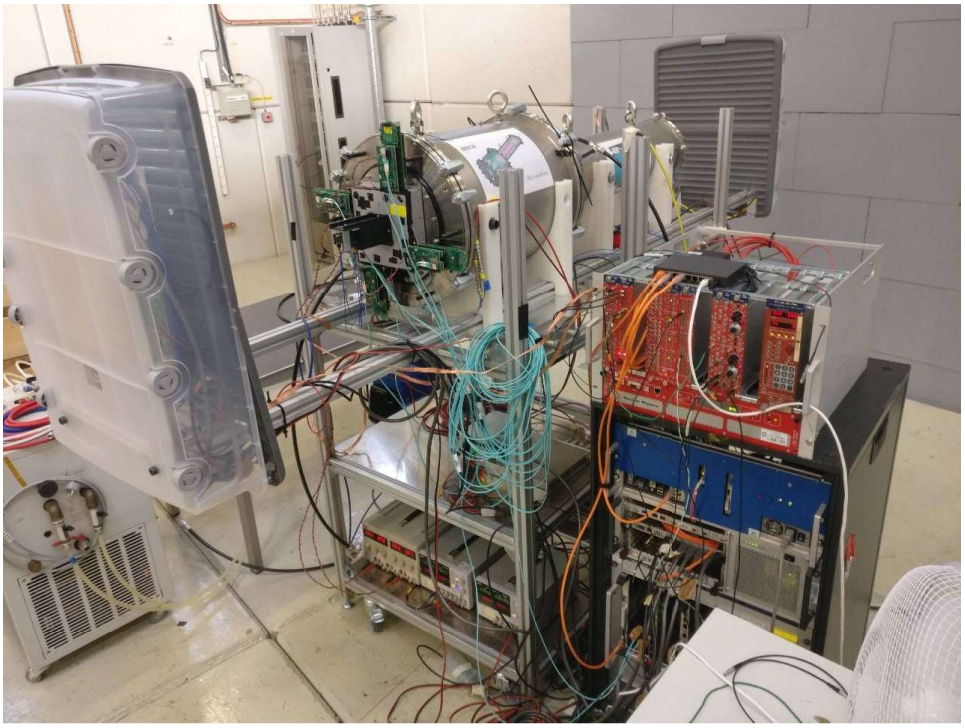

Figure 4.32: Experimental setup of the 2023 test beam at PS. The beam income from the left side. From the left to the right of the picture, it is possible to find the upstream GEM, inserted in the safety box to mitigate the high-voltage risk; the mechanical structure sustaining the detector, which is adjustable in height and inclination; the aerogel container, that is the small 3D-printed black box; the MAPMT box, in the "corner" configuration as deductible from the position of the electronic boards; the cylinders constituting the dRICH, which are filled of C_2F_6; and the second GEM inside the safety box. Also visible are the light blue optical fibers, for the communication of the MAROC readout with the storage; the power supplies, both for the readout electronic and for the tracking; the black pipe of the gas distribution system; the electronics boards handling and merging the tracking, trigger, and beam Cherenkov signals. The beam Cherenkov detectors are part of the beamline upstream of the prototype and are not visible.

Particle	Threshold $\leq m_K$	Threshold $\leq m_p$
π	✓	✓
K	✗	✓
p	✗	✗

Table 4.3: Example of beam Cherenkov threshold settings. The combined information permits the identification of the hadron passing the detector.

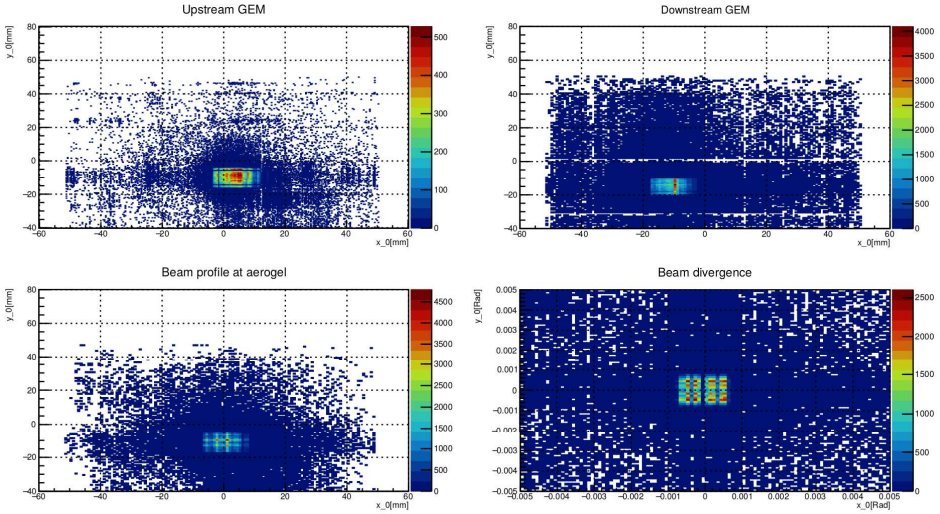

(a) The tracking plots for one run at SPS.

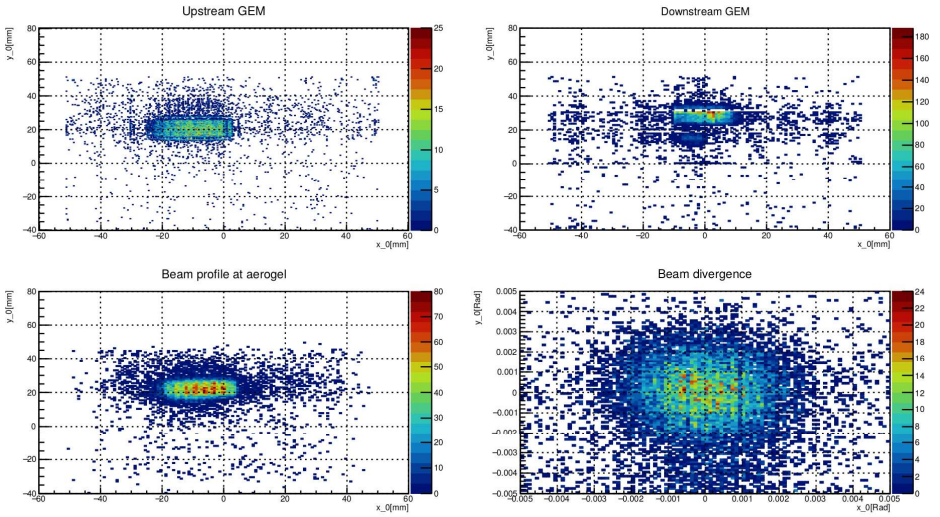

(b) The tracking plots for one run at PS.

Figure 4.33: The top plots show the beam profile in the two GEMs; the bottom plots show the extrapolated beam profile at the aerogel position and the divergence of the beam. Comparing the 4.33a and 4.33a plots, it is visible that the beam spot at SPS is smaller than at PS, and also it is smaller than the trigger $20 \times 10\,\mathrm{mm}^2$, although there is a larger background. Moreover, the divergence of the SPS beam is less than half of the PS beam. The GEM allows cleaning the data sample from spurious events with secondary interactions (high-angle traces).

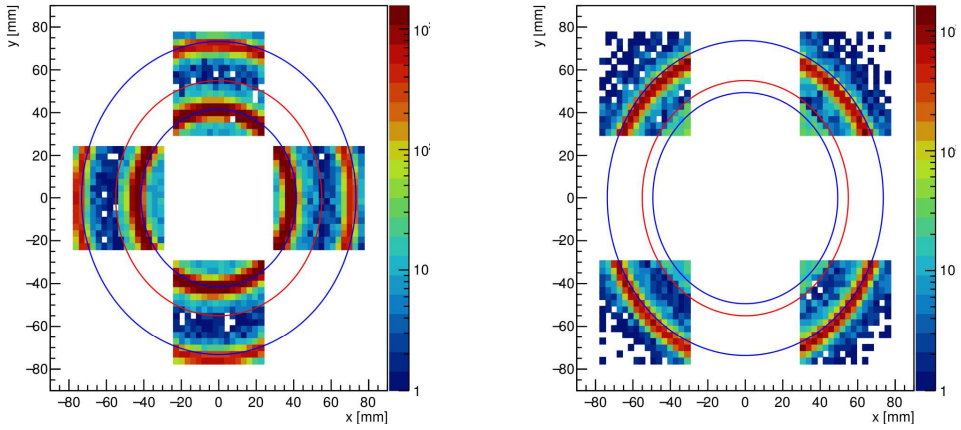

(a) Cumulated rings in the cross configuration.

(b) Cumulated rings in the corner configuration.

Figure 4.34: The two configurations of the MAPMT detector box. On the left, the two rings produced in gas and aerogel are visible. On the right, the ring produced by the aerogel is in the center of the photo-detectors and the gas ring is outside acceptance. The blue circles are the ring reconstructed during the analysis for gas (inner) and aerogel photons (outer), and the red one is the geometrical selection that is part of the photon assignment to the corresponding radiator.

cross, with the photo-detectors placed close to the side of the central aerogel tile, and *corner*, with the photo-detectors placed at the corner of the aerogel tile. The two configurations were used because the MAPMTs in the cross configuration cover almost the whole gas ring but only $\sim 40\%$ of the aerogel ring; moreover, the aerogel ring is close to the external edge of the photodetection area for the nominal refractive index of the original design ($n = 1.020$). The corner configuration permits covering the rest of the aerogel ring, and to study aerogel with a larger refractive index (1.023, 1.026) characterized by better transparency properties but does not provide acceptance for the gas ring. The plots of the rings acquired in cross and corner configurations are visible in Figure 4.34.

Data analysis

The author wrote the data analysis software in `C++`, using the analysis framework ROOT by CERN. The software is based on modular logic, so new information can be added at each step, allowing access to them along the entire analysis chain. It was designed this way because the software has been developed over the years, starting from the first test beams in 2021, making it easier to introduce modifications. The software performs the following operations:

- Reconstruction of the photon hits by coupling the signal falling and rising edges and applying time calibration;
- Selection of real photons based on the hit duration (time-over-threshold);
- Distinction of the photons produced in aerogel and gas based on their time-of-flight and a geometrical cut on the radius;
- Selection of ring photons using the time-coincidence technique;
- Computation and application of a primary correction of photon position for small misalignments of the mirrors, computing the mean ring center for each run based on the distribution of the hit position;
- If the tracking information is available, computation and application of a secondary correction of the position of each photon based on the misalignment of the beam particle from the nominal axis of the beamline;
- Averaging over the photon information associated with the particle, computation of the mean Cherenkov angle and time;
- Computation of the single-photon resolution, single-particle resolution, and its relation with the number of photons detected;
- When the beam Cherenkov detectors are available, computation of the same results for tagged particle species.

The assignment of photons to the ring is carried out in two steps. A preliminary distinction is based on a geometrical selection by defining "gas photons" as those with a radius lower than 55 mm and "aerogel photons" as the others. This permits the identification of two time-coincidence peaks, with a detectable difference of ~ 7 ns; the standard deviation of both peaks being ~ 1.2 ns. After calibration time-coincidence is the main criterion for assigning the photons to the right ring. Figure 4.35 summarizes the operation performed by the software on the hit. The first plot is the distribution of the start and end time of the hit, selecting only hits satisfying the requirements on the duration. The distribution of the time-over-threshold duration is shown in the second plot, where the green line represents the selection to exclude the short signal generated by cross-talk. The third is the two-dimensional plot showing the correlation between the photon arriving time and the hit duration. The fourth plot shows the time coincidence peak. The last two plots show the improvement in timing applying the calibration.

The main condition to be satisfied to consider a ring as good is that it includes at least 3 photons. A second selection is based on the divergence of the beam track, which is estimated as the trajectory angular difference with respect to the line connecting the center of the beam spots in the two GEMs.

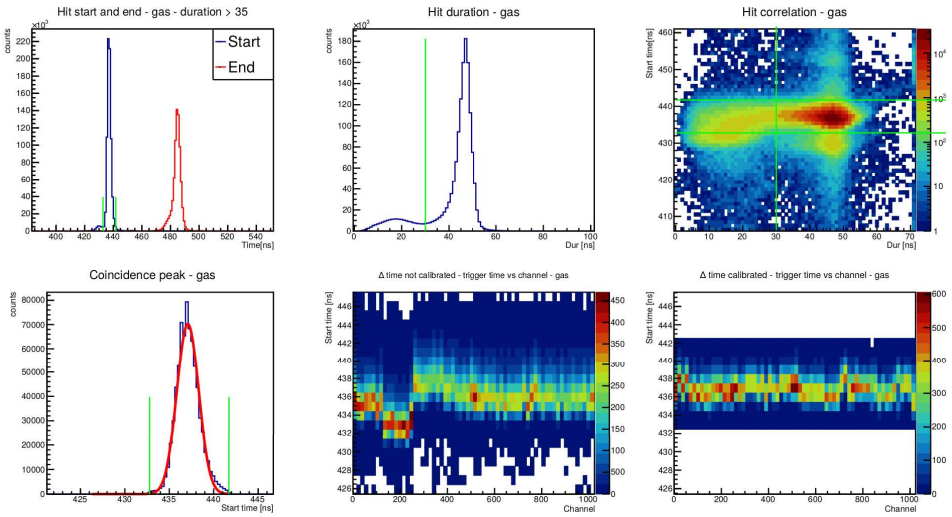

Figure 4.35: Plots summarizing the analysis operation to identify and assign the photon hits to the gas ring. Explanation in the text.

Incident particles with a polar angle larger than 2 mRad are removed from the sample.

The primary correction on the photon position was developed to compensate for small misalignments of the mirrors with respect to the detector axis. The correction starts from the computation of the mean optical center of the event, obtained by averaging the x and y coordinates of all the photons hitting the MAPMTs. This operation is made separately for gas and aerogel rings because the mirrors are not coupled, so they can affect the photon direction differently. The mean center is taken as the origin of the ring coordinate system, and the position of the photons is shifted accordingly.

The event-by-event correction based on the particle track divergence with respect to the beam axis was developed after the first test beam when a correlation between the particle incident angle and the ring position was noted. This permits the extrapolation of the correct center of the ring associated with the particle, by composing the global correction plus the projection of the single particle emittance.

The data acquired using a mixed-hadron beam of 120 GeV, momentum at which both the aerogel and gas rings are saturated for any particle species, are considered to explain the typical output of the analysis. In Figure 4.36, the first plot shows the distribution of the single-particle mean Cherenkov angle, the mean time of the photons associated with the particle, and the distribution of the number of photons for the particle. The first of these distributions is fitted with a Gaussian, whose mean value is taken to be the Cherenkov angle associated with the particle momentum, and the standard deviation is taken to be its resolution. The first and the second rows show the

results for gas (on top) and aerogel (bottom). From these plots is possible to compare the prototype results and the values expected from simulation, whose pseudo-data were adapted to be analyzed by the same software.

Additional results produced by the analysis are shown in Figure 4.37. The left ones are the distribution of the reconstructed Cherenkov angle of each photon associated with the ring for gas (on top) and aerogel (bottom), fitted again using a Gaussian function where the mean corresponds to the Cherenkov angle and the standard deviation with the single-photon resolution. The right plots show the single-particle resolution as a function of the number of photons associated with the ring. This graph is fitted with the function

$$\sigma_{sing\_part}(n_\gamma) = \sqrt{\frac{p_0^2}{n_\gamma} + p_1^2} \tag{4.6}$$

where parameter p_0 represents the single photon resolution, the best resolution achievable with only one photon, and p_1 is the asymptotic single-particle resolution, the minimum value achievable in an ideal situation of infinite photons. These plots allow the comparison of the SPE resolution obtained from two different methods and the analysis of the possible residual contribution to the resolution: a non-zero p_1 value signals systematics effects like misalignment or non-uniform detector response. The specific results for aerogel and gas and their comparison with simulation are commented in the next Section.

4.4 Results of the prototype studies

In this section, the measured performances of the prototype are reported and compared with the expected values provided by the simulation. The simulation described in section 4.3.3 is the newest version of the prototype simulation. It has been described because of its importance in the design phase and because the author developed it. Despite being the last version, it is still optimistic and reproduces the prototype only partially. This implies that its simulated resolution is better than the one achievable with the prototype. The resolution achieved with the prototype is then compared with the values reported in Table 4.2.

4.4.1 Results for gas ring

The data selected to study the gas resolution were acquired at SPS using the mixed-hadrons 120 GeV beam. The SPE resolution measured is consistent with the estimation described in Section 4.3.3 because it is 1.1 mRad for both the alternate methods (Gaussian RMS of the SPE distribution or parameter p_0 in the fit of the resolution per track as a function of the number of detected photons). The parameter p_1 assumes non-zero values (0.24 mRad). It signals

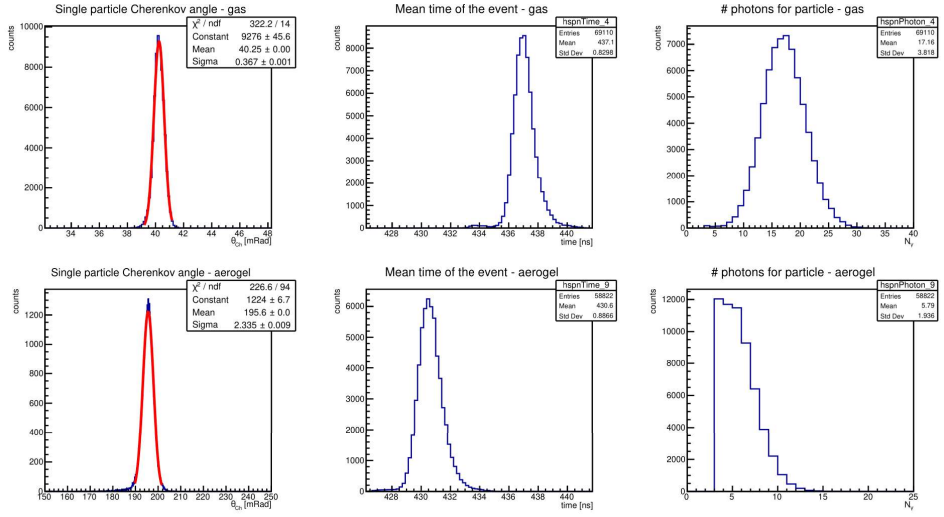

Figure 4.36: Example of the results of the prototype analysis, for the case of a 120 GeV beam of mixed hadrons. From left to right: the distribution of single-particle mean Cherenkov angle, the distribution of the mean time of photons, and the distribution of the number of photons for particle. In the top row are the plots for gas, and in the bottom row the plots for aerogel. In the rightmost column, the partial coverage of the aerogel ring is evident.

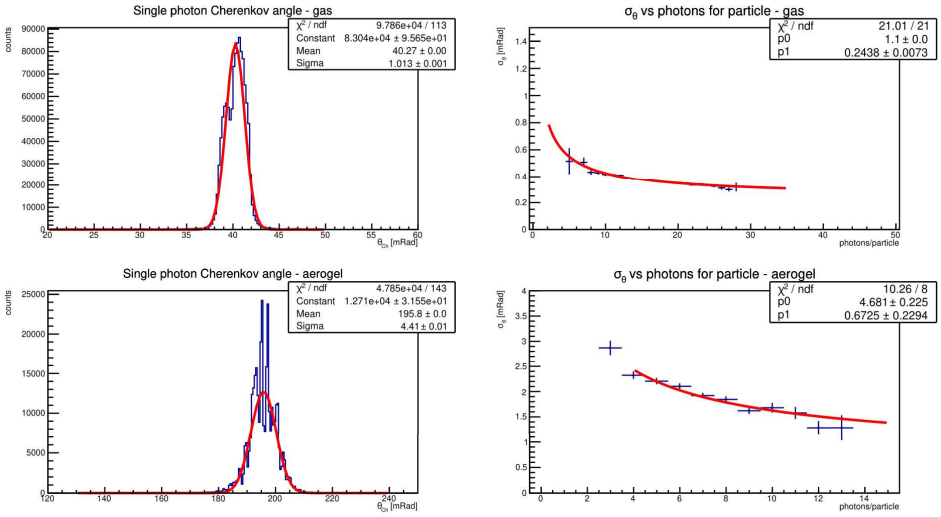

Figure 4.37: Example of the typical results of the prototype analysis, for the case of a 120 GeV beam of mixed hadrons. From left to right: the distribution of SPE Cherenkov angle resolution and the single-particle resolution vs the number of detected photons. In the top row are the plots for gas, and in the bottom row are the plots for aerogel.

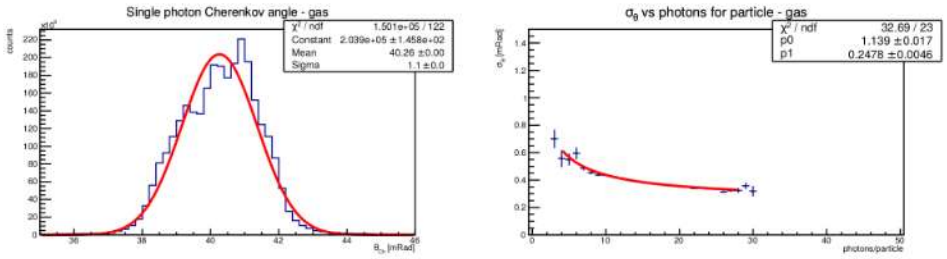

Figure 4.38: Single-photon results for gas ring. From left to right: the single-photon mean Cherenkov angle, and the single-particle resolution as a function of the number of photons detected.

systematic effects like non-uniform detector response or a misalignment not recovered by the applied corrections.

The plots of the single-particle mean Cherenkov angle and of the number of photons detected per particle are reported in Figure 4.39. The best single-particle resolution achieved with the prototype is 0.35 mRad, which is almost 1.5 times the expected values reported in Table 4.2. By considering the non-zero constant term, the expected single particle resolution became 0.35 mRad, which is comparable with the measured value. The non-zero p_1 values could mean that both a misalignment and a systematic non-uniformity concur in the prototype. The measured values could improve further by applying a most refined reconstruction algorithm, like the ray-tracing algorithm developed for the ePIC dRICH simulation, and testing the prototype with the SiPM detector box because the silicon-based sensors are less sensitive to the chromatic contribution to the error rather than the MAPMT thanks to the different quantum efficiency range. Introducing a more sophisticated reconstruction algorithm can also help to understand the origin of the constant term, which has not yet been reproduced in the prototype simulation. The mean number of photons detected from the prototype is smaller than the expectation from the simulation, 17.1 compared to 20.3.

4.4.2 Results for aerogel ring

The data selected to study the aerogel ring were acquired using a negative mixed-hadrons beam at 10 GeV. For this momentum value, the dominant component of the beam is constituted by pions, while kaons and antiprotons are in the order of a few percent. Although the aerogel ring is not fully saturated, this negative beam provided the best combination between a clean pion sample and luminosity to acquire enough statistics during the August 2023 test beam. Figure 4.40 shows the single-photon Cherenkov angle distribution and the plot of single-particle resolution as a function of the

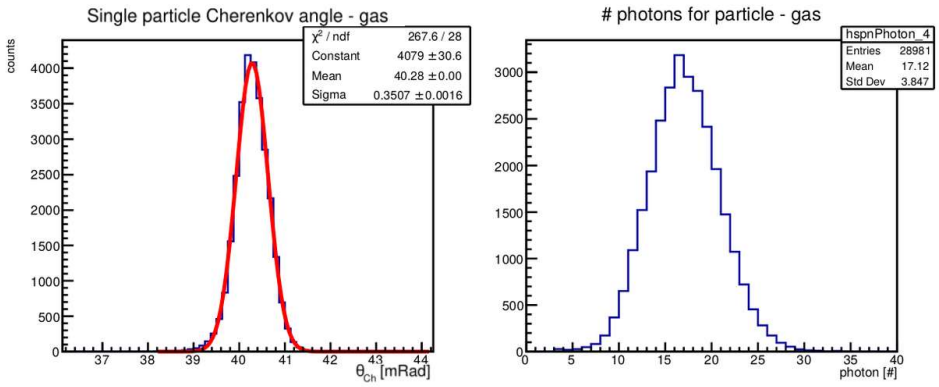

Figure 4.39: Single-particle results for gas ring. From left to right: the single-particle mean Cherenkov angle, and the number of photons detected.

number of detected photons per particle, and Figure 4.41 shows the single-particle mean Cherenkov angle and the number of photons per particle plots, In both Figures, the first row reports the results obtained using the aerogel with refractive index $n = 1.026$, and the second uses the design aerogel with refractive index $n = 1.020$. These results of the aerogel sample with two different refractive indices were reported because the aerogel with a larger refractive index showed better performance in the resolution and number of photons, as expected from the results of the characterization performed in the laboratory, while the other is the original design value expected for the ePIC dRICH.

The most reliable of SPE resolutions for aerogel were obtained from the standard deviation of the leftmost column in Figure 4.40 because of the low number of points in the rightmost column plots. Indeed it makes the curve more approximable with a linear dependence, resulting in a lack of accuracy. This is confirmed by the relative errors on parameter p_0 (Equation 4.6), which are one order of magnitude larger than the case of the gas ring.

The single-photon and single-particle resolutions achieved using the $n = 1.026$ aerogel are 3.4 mRad and 2.0 mRad, while for the $n = 1.020$ aerogel are 4.7 mRad and 2.8 mRad. The comparison value reported in Table 4.2 are 3.0 mRad and 1.2 mRad. The SPE resolution achieved with the $n = 1.026$ aerogel was close to the expected performance. A deeper and more completed analysis will be performed using the SiPM detector box in the last version, which covers almost the full aerogel ring, allowing the detection of more photons. The values of the p_1 tell us that the constant term present for the gas is zero for the aerogel. This is possible because the two rings are decoupled in the prototype, and then it is possible that there is a systematic effect on the gas section that is not present in the aerogel section. Regarding

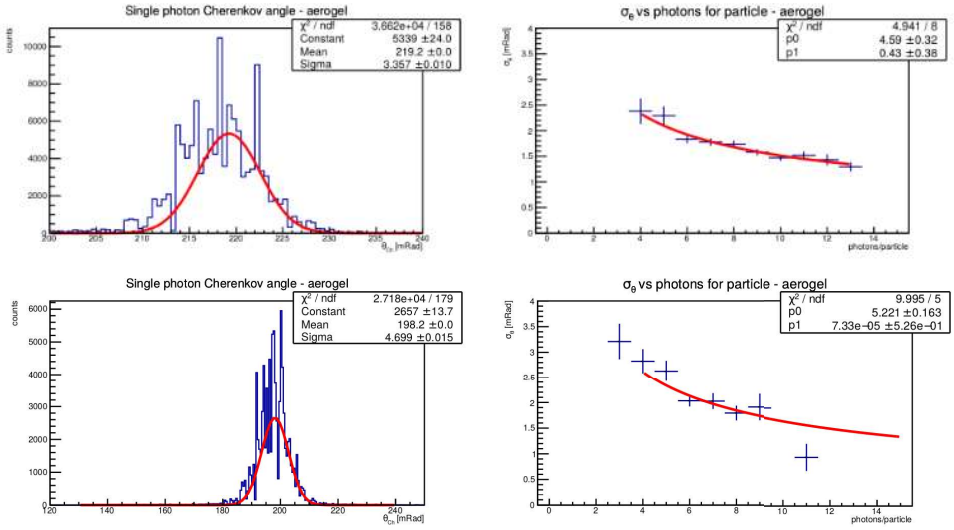

Figure 4.40: Single-photon results for aerogel ring. From left to right: the single-photon Cherenkov angle, and the single-particle resolution as a function of the number of photons detected. On the top row are plots showing the best resolution obtained using tiles with refractive index $n = 1.026$; in the bottom row are plots showing the results obtained using tiles with refractive index $n = 1.020$.

the number of photons, there is an agreement between the simulation and the data acquired for $n = 1.020$ aerogel with a mean of 5.2 photons while using the $n = 1.026$ aerogel 8.0 photons for particle are detected, a larger value as expected from the results of radiator characterization.

The numerical results are summarized in Table 4.4. It shows that the prototype performance almost satisfies the expectations in terms of SPE resolution for both gas and aerogel. The gas SPE resolution of 1.1 mRad has been obtained since the 2022 test beam. Alternative developments will be studied with the updated prototype designed to test alternate gas mixtures and non-greenhouse pressurized gases. For the aerogel ring, the best SPE resolution obtained till the 2022 test beams was about 4.5 mRad, 1.5 times worse than the expected value of 3.0 mRad. The study performed in the 2023 test beam, described in the following, achieved a SPE resolution of 3.4 mRad, which is close to the design goal.

Future developments of the reconstruction software, for example, by implementing a ray-tracing algorithm to reconstruct the single-photon path, will allow further refinements in the resolution study.

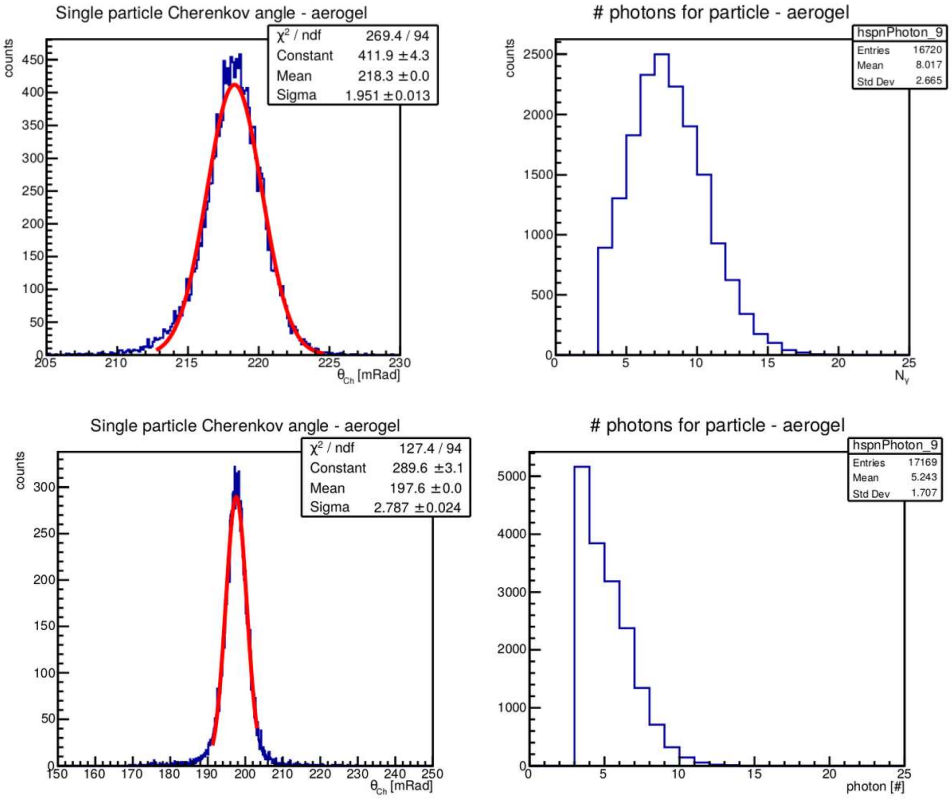

Figure 4.41: Single-particle results for aerogel ring. From left to right: the single-particle mean Cherenkov angle, and the number of photons detected. On the top row are plots showing the best resolution obtained using tiles with refractive index $n = 1.026$; in the bottom row are plots showing the results obtained using tiles with refractive index $n = 1.020$.

Summary table of the prototype performance					
Source	SPE σ [mRad]	Single-particle σ [mRad]	Photons/particle	p_0 [mRad]	p_1 [mRad]
Gas					
Data	1.10 ± 0.01	0.351 ± 0.002	17 ± 4	1.14 ± 0.02	0.248 ± 0.005
Simulation	1.1	0.25 (0.35 if constant term $c_0 \simeq 0.25$)	20 ± 4	N/A	N/A
Aerogel					
Data $n = 1.020$	4.70 ± 0.02	2.79 ± 0.02	5.2 ± 1.7	5.22 ± 0.16	0.0 ± 0.5
Data $n = 1.026$	3.36 ± 0.01	1.95 ± 0.01	8 ± 3	4.6 ± 0.3	0.4 ± 0.4
Simulation	3.0	1.3	5.4 ± 1.7	N/A	N/A

Table 4.4: Table summarizing the performance of the prototype. The error reported is the statistical error provided by ROOT for quantities extracted by a fit, and the standard deviation for the number of photons. A cut-off on the third digit is applied in case of small errors. For the simulations, the resolution values were provided in Table 4.2, and the expected number of photons was taken from the original simulation prototype. The parameters p_0 and p_1 for simulations were not considered reliable because of the excess of optimism of the prototype simulation and were not reported.

4.4.3 Aerogel study with the prototype

The goal of the August 2023 test beam was a detailed study of the aerogel resolution, having prior performed the laboratory characterization described in section 4.3.2. Using the aerogel samples from Aerogel Factory Co. highlighted in Table 4.1 and the two *corner* and *cross* configurations of MAPMTs, data were acquired for refractive index between $n_{min} = 1.016$ and $n_{max} = 1.026$. Figure 4.42 shows the measured single-photon and single-particle resolutions. From both plots, it is possible to see that by increasing the refractive index, the resolution improves; in particular, for $n = 1.026$, the SPE resolution measured is 3.4 mRad, which is the best result achieved. Figure 4.43a shows the number of photons for particle detected by the prototype as a function of the refractive index; as expected from the increasing of density and transmission Λ_T, aerogel with larger refractive index yields more photons. Figure 4.43b completes the results of this study, showing the measured Cherenkov angle that grows naturally with the increase of the refractive index. This study showed that aerogel with a larger refractive index provides more defined rings. Motivated by these results, the ePIC simulation group initiated a study to evaluate the impact of increasing the aerogel refractive index.

4.4.4 Studies using the beam PID system

The beam PID system described in section 4.3.4 permits to tag the hadron species passing through the detector with good efficiency and therefore the direct study of the prototype PID capability. For the gas component, this study used a beam of positive mixed hadrons with a momentum of 20 GeV and 50 GeV, covering the momentum range over which the identification is based on that radiator. The largest beam component is constituted by pions, followed by protons; the kaons are just a few percent, and they are detected by the prototype. The single-particle Cherenkov angle distribution for tagged hadron species is shown in Figure 4.44 and Figure 4.45. At 20 GeV, the kaon peak is clearly separated from the pion one. At 50 GeV, the proton peak appears, while the kaon starts to overlap with the pion peak. In both cases, a small inefficiency of the beam PID system is visible but does not affect the result.

The aerogel component was studied using beams of mixed positive hadrons with $6, 8$, and 10 GeV momentum. The plots are reported in Figure 4.46, Figure 4.47, and Figure 4.48. In this case, the beam Cherenkov had more inefficiencies, but the peaks of the three species are still visible. These data were acquired with the $n = 1.026$ aerogel, and the MAPMTs in the *corner* configuration, for which any information from the gas is lost. Comparing the three plots, the modification of the beam composition with the energy is also visible: protons became the major components at 10 GeV while the kaons represent always a small fraction (few percent).

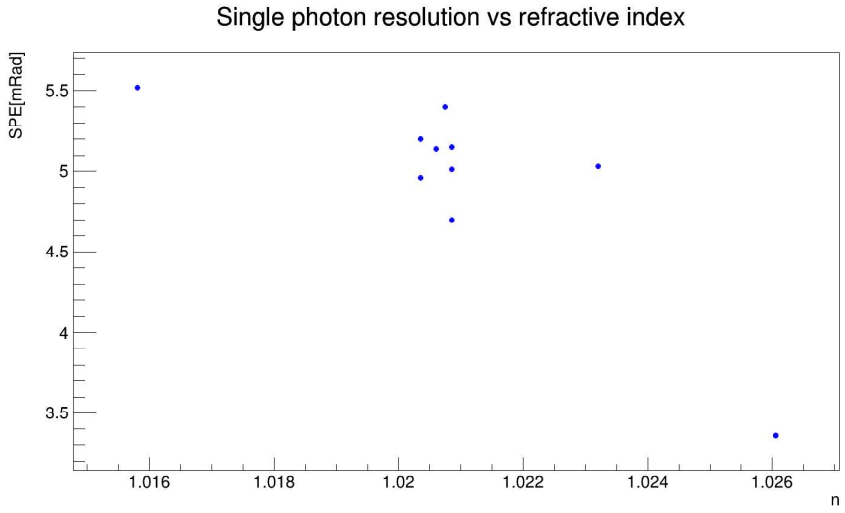

(a) Single photon resolution measured by the prototype using aerogel with different refractive index. The cluster of measurement at $n \simeq 1.020$ is due to the fact that several tiles with this refractive index were tested, and the result from the 2022 test beam was also included.

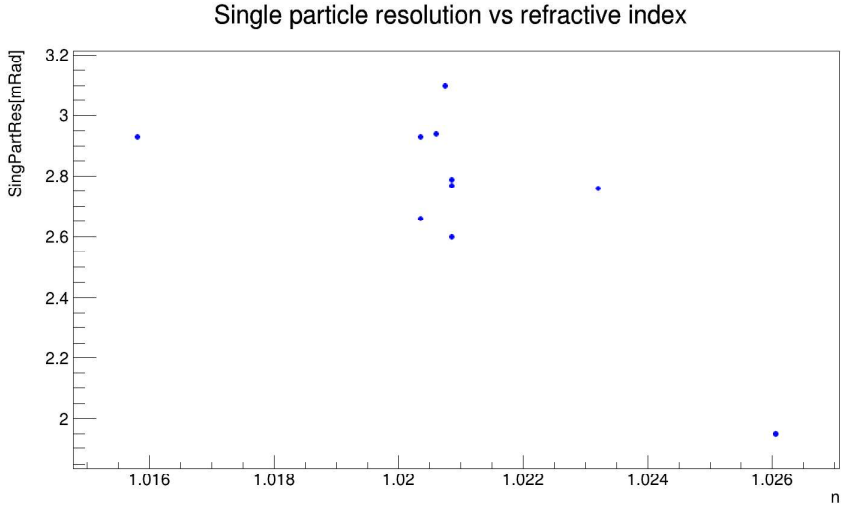

(b) Single-particle resolution measured by the prototype using aerogel with different refractive index. The cluster of measurement at $n \simeq 1.020$ is due to the fact that several tiles with this refractive index were tested, and the result from the 2022 test beam was also included.

Figure 4.42: Results of 2023 aerogel study

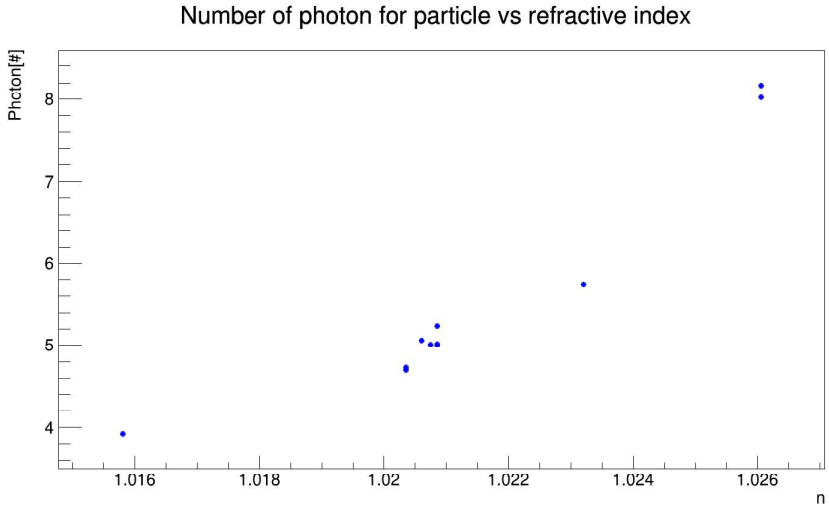

(a) The number of photons for particles detected by the prototype using aerogel with different refractive indices. The cluster of measurement at $n \simeq 1.020$ is due to the fact that several tiles with this refractive index were tested, and the result from the 2022 test beam was also included.

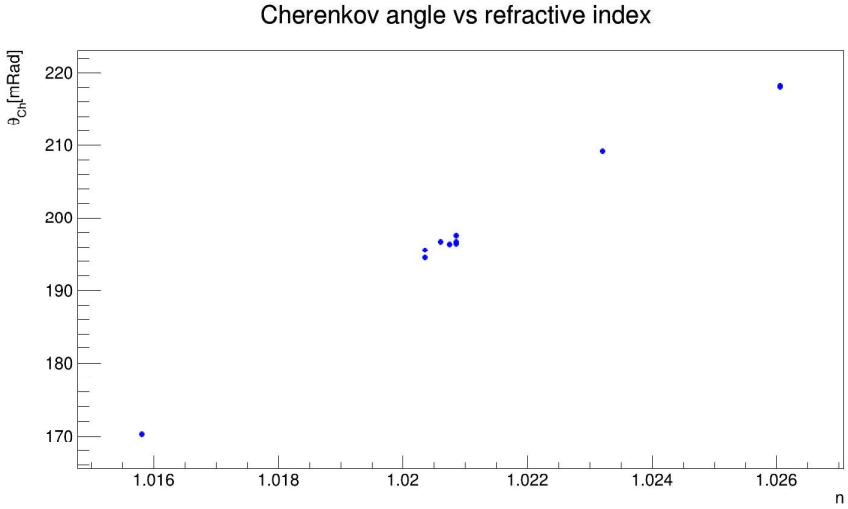

(b) Cherenkov angle measured by the prototype using aerogel with different refractive index. The cluster of measurement at $n \simeq 1.020$ is due to the fact that several tiles with this refractive index were tested, and the result from the 2022 test beam was also included.

Figure 4.43: Results of 2023 aerogel study

These results confirm the capability of the prototype to detect and identify different particle species.

4.5 Conclusions

The Electron-Ion Collider is designed to expand the frontiers of the known Quantum Chromodynamics. Colliding high momentum and highly polarized beams with a high luminosity will produce data allowing unprecedented studies of the nuclear structure and parton dynamics. This can be done by studying SIDIS reactions, which requires the detection of at least one hadron in the final state. The particle identification in the hadronic endcap of the ePIC experiment will be carried out by a dual-radiator Ring Imaging Cherenkov detector. The dRICH is being designed by a collaboration of several institutions led by INFN. This detector is facing two main challenges: the broad momentum range in which the hadron must be identified, and single-photon detection in high magnetic field. The moderate background radiation level expected at ePIC will progressively damage the selected magnetic-insensitive SiPM photosensors. A study on recovering the photodetectors perfomance via high-temperature annealing has provided good indications, suggesting the possibility of performing the cure directly in-situ without removing the SiPMs.

A dRICH prototype was realized and tested between 2020 and 2023 to support the detector design phase. It allowed to measure the optical performance using a reference photon detector. The double rings were detected using both a reference MAPMT detector and the SiPM, and the SPE resolution measured for gas and aerogel is similar to the values expected from the simulation. These results support the design and the feasibility of the dRICH detector for ePIC, and will be further validated with a new real-scale prototype.

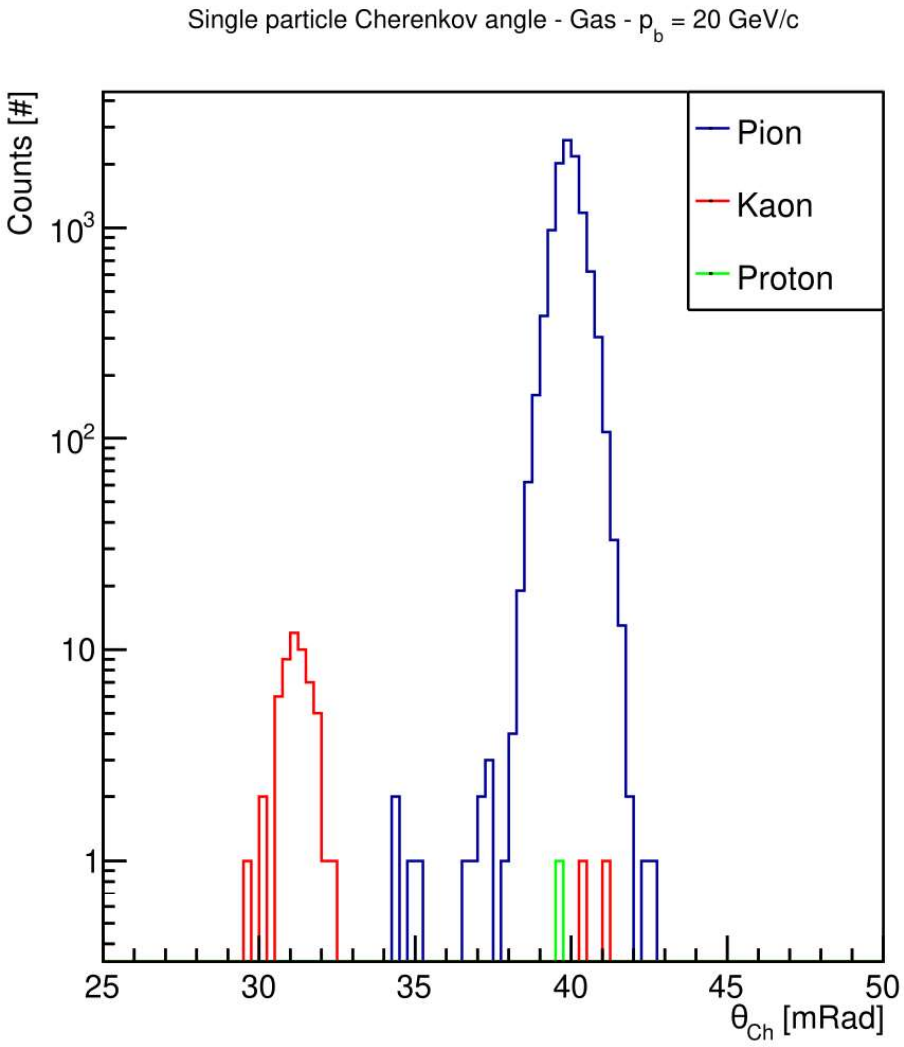

Figure 4.44: Distribution of the single-particle Cherenkov angle for gas photons, for particle species tagged by the beam PID system. At 20 GeV beam momentum, the kaon peak is clearly separated from the pion peak, while the proton does not produce a ring being below the Cherenkov threshold.

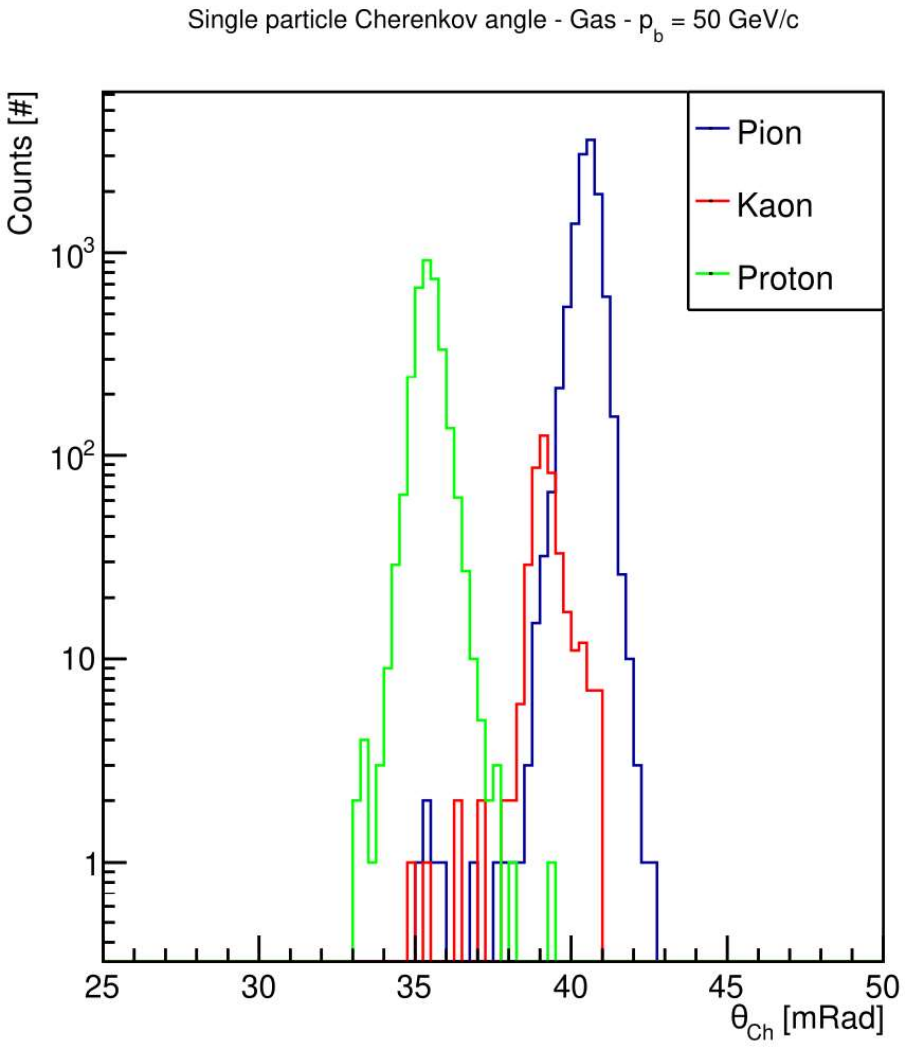

Figure 4.45: Distribution of the single-particle Cherenkov angle for gas photons, for particle species tagged by the beam PID system. At 50 GeV beam momentum, the kaon peak starts merging into the pion peak, while the proton peak is well separated from the others.

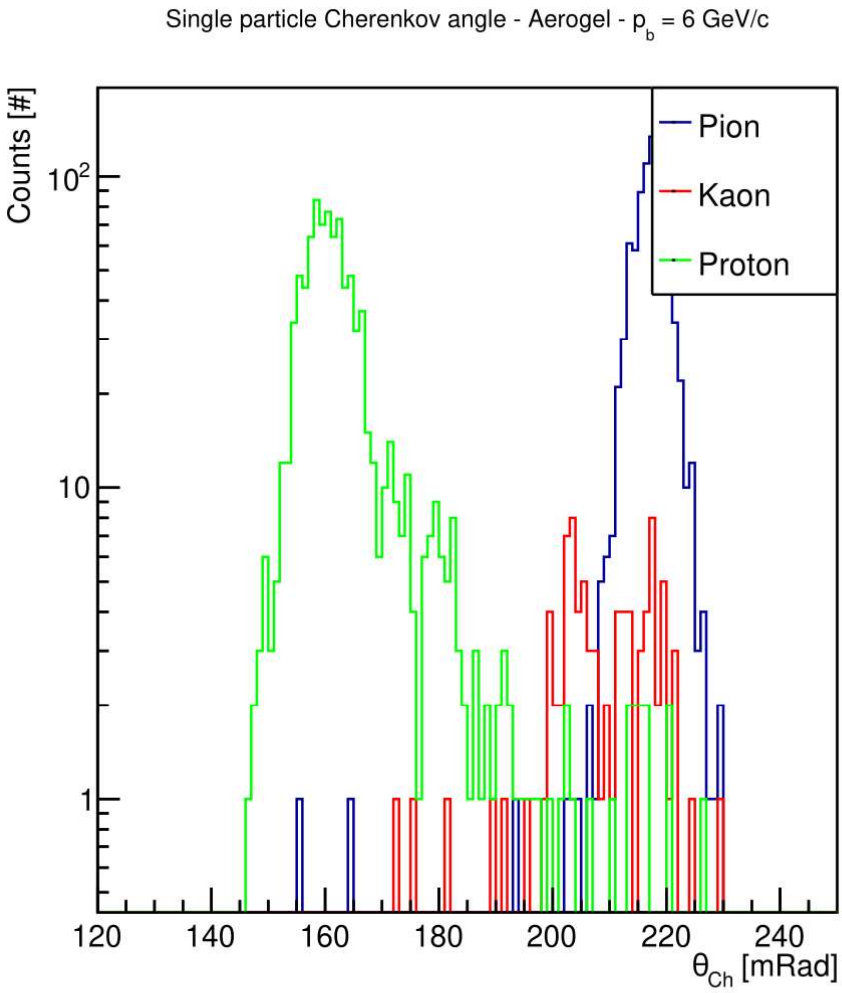

Figure 4.46: Distribution of the single-particle Cherenkov angle for aerogel photons, for particle species tagged by the beam PID system. At 6 GeV beam momentum, the proton peak is well separated from the others. The kaon peak is barely visible around 205 mRad, although it is diluted by the beam PID inefficiency.

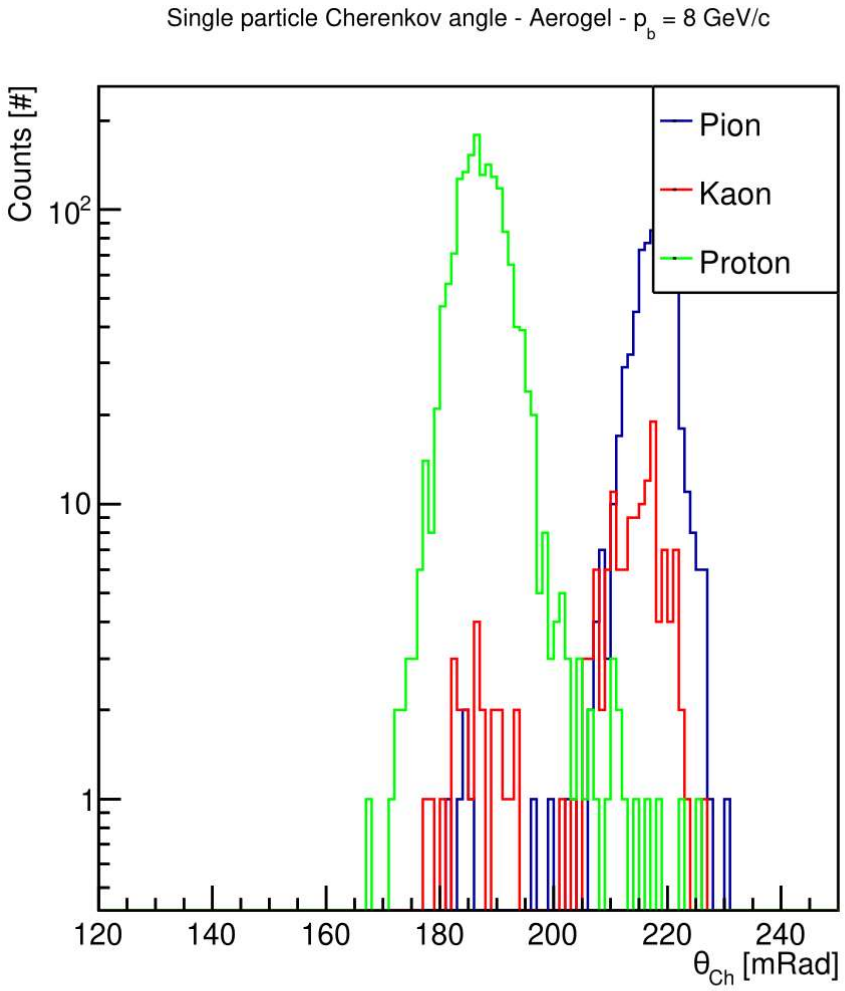

Figure 4.47: Distribution of the single-particle Cherenkov for aerogel photons, for particle species tagged by the beam PID system. At 8 GeV beam momentum, the proton peak is well separated from the others. Although the kaon peak is visible, it starts merging into the pion peak.

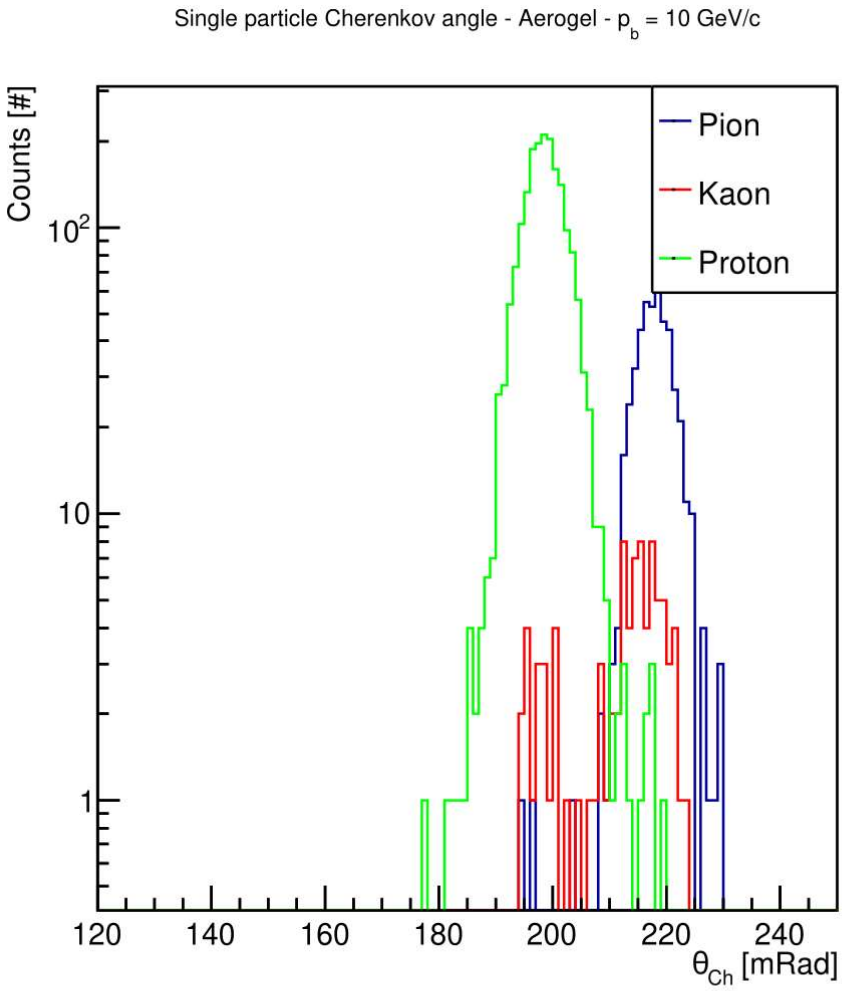

Figure 4.48: Distribution of the single-particle Cherenkov angle for aerogel photons, for particle species tagged by the beam PID system. At 10 GeV beam momentum, the proton peak is well separated from the others. The kaon peak results overlapping the pion peak.

Conclusions

The never-ending journey of understanding how matter is made has seen remarkable progress pursued by humankind. The last half-century has unlocked the possibility of exploring the nature surrounding us through new perspectives thanks to the results achieved in understanding atomic, nuclear, and nucleon structures. The advancement of theoretical knowledge and technical expertise, which are entangled aspects of science, has enabled access to the three-dimensional structure of nucleons by measuring the Transverse-Momentum-Dependent (TMD) Parton Distribution Functions (PDFs) and TMD Fragmentation Functions (FFs) (generically TMDs). This was like a Copernican revolution of subatomic structure studies, allowing us to overcome the traditional one-dimensional models. The Semi-Inclusive Deep Inelastic Scattering (SIDIS) is a powerful tool to access the transverse degrees of freedom of partons, providing low-scale information that are much more sensitive to the details of hadron's internal structure.

This document described the author's contribution in developing and installing Ring Imaging Cherenkov detectors, which combine the Cherenkov angle of photons produced passing through a radiator with the kinematic information to identify the charged particle species. They play a crucial role in SIDIS, in which at least one hadron is detected in the final state in addition to the scattered electron. Proper identification of the hadron provides information about the flavor of the parton involved in the interaction. The author's contribution focused on the Particle Identification (PID) detectors for the CLAS12 spectrometer at Jefferson Laboratory and for the ePIC experiment at the future Electron-Ion Collider (EIC) at Brookhaven National Laboratory (BNL).

Chapter 1 provides an overview of the theoretical basis of the TMD distributions, introducing the tools needed to extend the nucleon's structure investigation from the historical one-dimensional parton distribution to three-dimensional imaging.

In Chapter 2, the innovative RICH detector of the CLAS12 spectrometer was described. The hybrid-optics design, incorporating aerogel radiators, visible light photon detectors, and a focusing mirror system, allowed the instrument to fit into the limited space available in the CLAS12 Forward Carriage and minimize the detector's cost and material budget. The detector

was installed to improve the $\pi^{\pm}/K^{\pm}$ separation in the higher momentum range accessible with CLAS12 ($3 \div 8\,\mathrm{GeV}$). The author participated in the assembly and commissioning of the second detector module, having a major role in assembling and testing the front-end electronics, mounting and testing the photosensors, characterizing the spherical mirrors, cabling the detector services to the CLAS12 infrastructure, and performing the first functionality tests of the new module. Currently, the second RICH module is running and acquiring data together with the rest of the spectrometer. This Chapter also contains the efficiency study performed by the author on the first RICH module installed in 2018. The study was based on the final states that included a positive hadron eH^+X. By analyzing the missing mass and exploiting allowed or forbidden exclusive channels, it is possible to evaluate contamination of misidentified pions into the kaon sample, which was found to be less than 2% overall. This efficiency evaluation is essential because one of the RICH aims is to improve the high-momentum kaon identification, providing a clean sample for kaon SIDIS studies.

Chapter 3 focuses on the study of the Beam-Spin Asymmetry performed by the author. The SIDIS cross-section can be expressed as the sum of contributions related to different beam and target spin polarization combinations. The clean kaon sample identified by the RICH allows us to perform a preliminary measurement of the structure-function $F_{LU}^{\sin\phi}$, having reduced the pion contamination. Because the statistics of the kaon sample remain relatively low, the Unbinned Maximum Likelihood (UML) fit method was selected to extract the results. The analysis procedure was completed by the evaluation of the contribution to the systematic error introduced by the novel PID. The analysis is proposed as a case study for the measurements made possible at CLAS12 by the improved PID capability for the high-momentum hadrons achieved with the RICH installation. The preliminary results show the capability of measuring the BSA with CLAS12 despite the low statistics and do not contradict the previously published results. More completion results will be provided in the future, when the software alignment of the RICH will be complete increasing the available phase space up to the design polar angle of 26°. Moreover, some of the data have not been analyzed because they were acquired in a different torus configuration and require systematic uncertainty fine-tuning. In a less immediate future, the second RICH module increases the capability of acquiring more statistics with the same beamtime to further reduce the statistic uncertainty.

Finally, Chapter 4 described the studies on the PID for the ePIC experiment, which is currently under development for the future EIC at BNL. EIC will be the new world-leading electron-ion collider, aiming to unlock the frontiers of QCD. SIDIS will be one of the main topics of physics interest at the new ePIC experiment, aiming to provide high-precision three-dimensional images of the nucleon. The author was involved in the research and development of the dual-radiator Ring Imaging Cherenkov, a detector aiming to

identify charged hadrons in a broad momentum range ($3 \div 50\,\mathrm{GeV/c}$) and contribute to the electron identification while operating in a high-magnetic field ($\sim 1\,\mathrm{T}$). To cover the whole momentum range, which crosses the typical regions where aerogel and gas radiators are used, the dRICH will detect the photons produced by two different radiators and combine this information to identify the particle. Working in single-photon detection mode in a high-magnetic field poses an additional challenge because it excludes the use of Multi-Anode Photomultiplier Tube, a typical sensor for this application. The proposed solution is to use Silicon Photomultiplier because they are insensitive to the magnetic field. They can suffer radiation damage tough, which increases the Dark Count Rate, making operation in single-photon mode more complex. The author participated to the study of the possibility of curing sensors via high-temperature annealing, which provided promising results. The tests allowed the formulation of a working scheme for the detector based on several in-situ annealing cycles, performed by directly polarizing the sensors and exploiting the Joule effect, and a possible maintenance operation when sensors are removed for long annealing in the oven. The last part of the Chapter describes the dRICH prototype development and performance test. The author dedicated a significant effort to this activity, contributing to the design, implementing the prototype simulation, developing the reconstruction and analysis software, characterizing the prototype elements, participating in several test beams as responsible for the analysis software and the tracking system, and analyzing the collected data. The prototype results are comparable to the performance expected from the simulation, supporting the design and the feasibility of the ePIC PID subsystem.

The work described in this thesis represents the author's contribution to the development of innovative PID instrumentation, which plays a crucial role in SIDIS studies. In the near future, these studies are expected to provide unprecedented information about the nucleon's structure and inner dynamics, allowing new advances in the understanding of the true nature of matter.

Appendix A

Result from scattering off Hydrogen

Appendix A reports the results obtained by applying the same analysis procedure described in Chapter 3 to data of 10.2 GeV/c polarized electron beam scattering off a Hydrogen target. The plots of the one-dimensional, four-dimensional, and pion and kaon SIDIS comparison are shown.

The one-dimensional results are shown as a function of one of the electron and kaon variables in Figures 49, 50, 51, and 52. They show that the asymmetry is detectable using the CLAS12 spectrometer for kaons identified by the RICH. The red area describes the effect of the total systematic uncertainty, which is a second-order effect with respect to the statistical uncertainty. Despite the limited statistical precision, the plots show the asymmetry tends to be zero for small z and p_T, as expected from theory.

The same four-dimensional binning used for scattering off deuterium target data was applied. The results for the bins in the electron variables and the correspondent bins in z are expressed as a function of p_T and shown in Figures 53, 54, and 55.

The one-dimensional comparison of the structure-function obtained from pion and kaon is shown in Figure 56. Generally, the results obtained from analyzing the two samples are close, but especially the kaons are dominated by the statistical uncertainty. More reliable results could be obtained in future studies with the completion of the RICH alignment extending the polar angle range up to the design 26° and analyzing the full statistics.

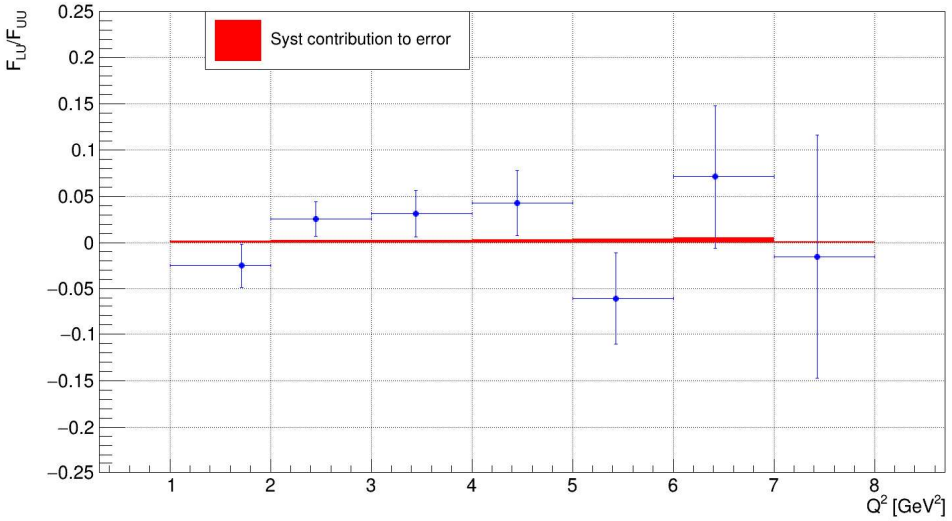

Figure 49: $F_{LU}^{\sin\phi}/F_{UU}$ as a function of Q^2. The red area shows the contribution of the total systematic uncertainty to the measurement error.

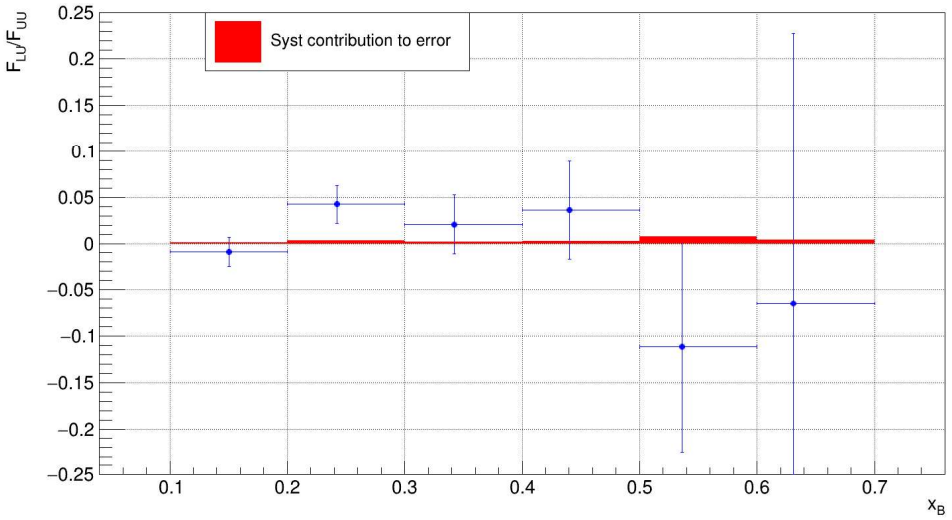

Figure 50: $F_{LU}^{\sin\phi}/F_{UU}$ as a function of x_B. The red area shows the contribution of the total systematic uncertainty to the measurement error.

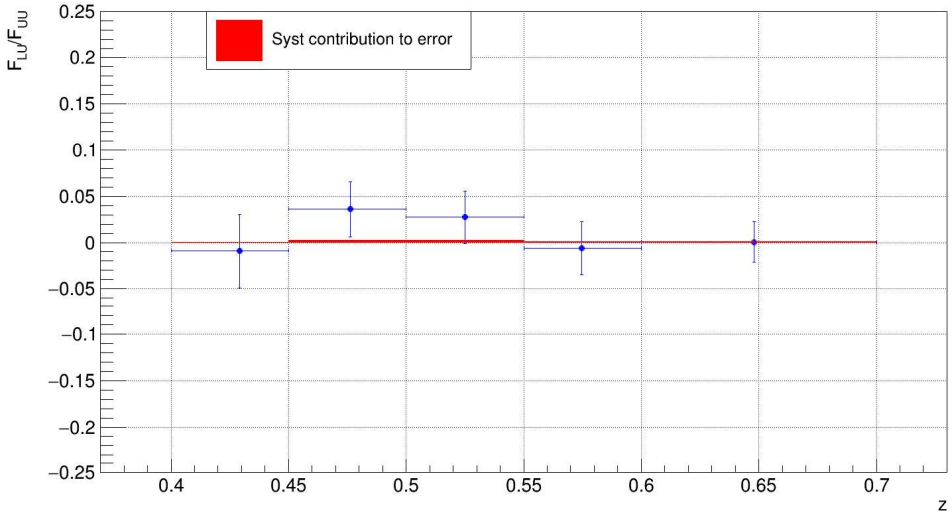

Figure 51: $F_{LU}^{\sin\phi}/F_{UU}$ as a function of z. The red area shows the contribution of the total systematic uncertainty to the measurement error.

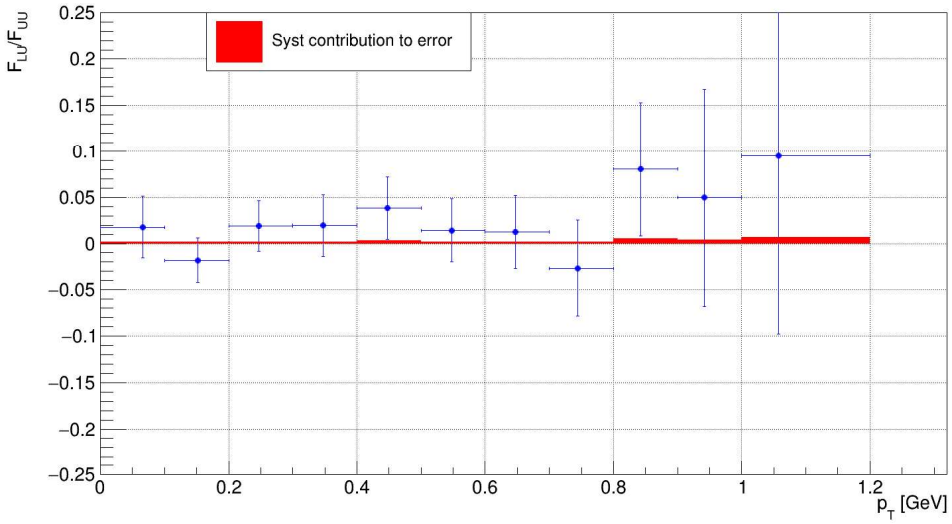

Figure 52: $F_{LU}^{\sin\phi}/F_{UU}$ as a function of p_T. The red area shows the contribution of the total systematic uncertainty to the measurement error.

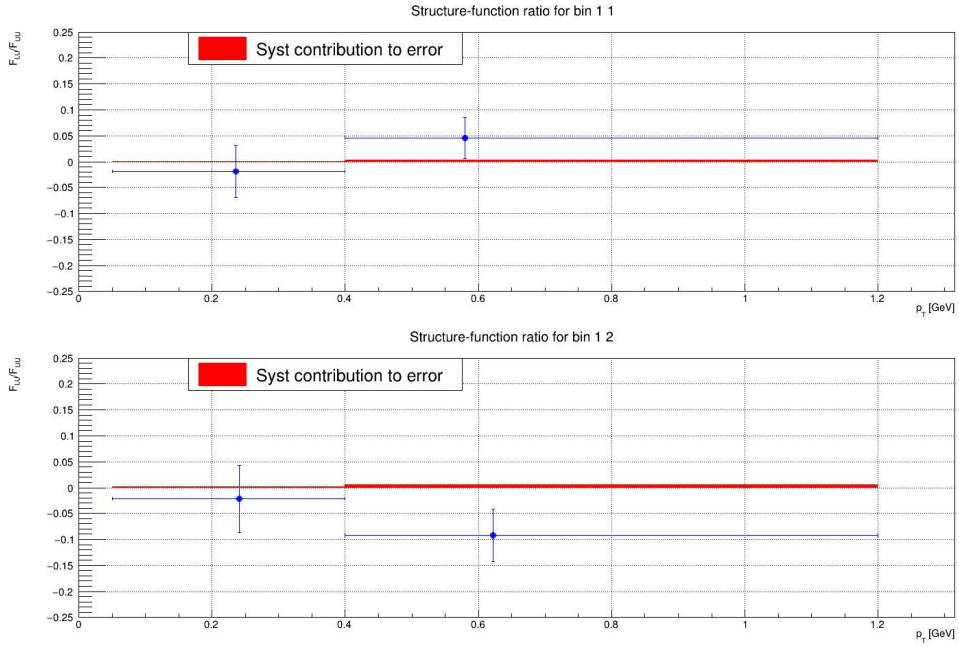

Figure 53: $F_{LU}^{\sin\phi}$ as a function of p_T, for the first bin on the electron variables and the two bins in z. The mean values and bin extremes are $Q^2 = 1.6(1.0, 3.0)$, $x_B = 0.12(0.09, 0.14)$ for both plots and respectively $z = 0.51(0.35, 0.62)$ and $z = 0.72(0.62, 0.95)$ for top and bottom. The x-coordinate of each point shows the mean value of p_T, and the correspondent error bar shows the bin width.

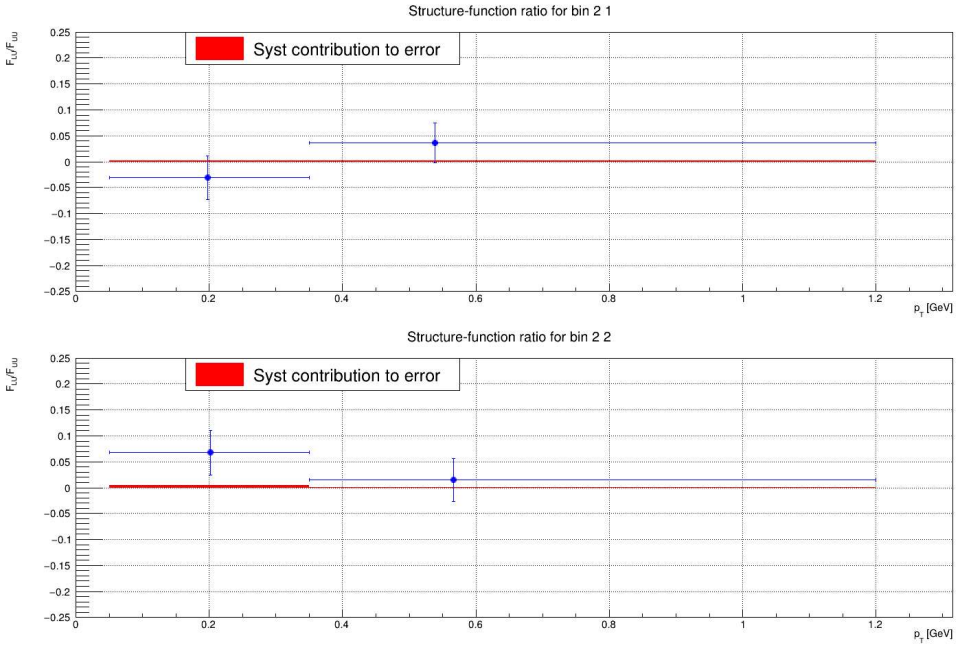

Figure 54: $F_{LU}^{\sin\phi}$ as a function of p_T, for the second bin on the electron variables and the two bins in z. The mean values and bin extremes are $Q^2 = 2.2(1.0, 3.8)$, $x_B = 0.16(0.14, 0.19)$ for both plots and respectively $z = 0.51(0.35, 0.60)$ and $z = 0.70(0.60, 0.95)$ for top and bottom. The x-coordinate of each point shows the mean value of p_T, and the correspondent error bar shows the bin width.

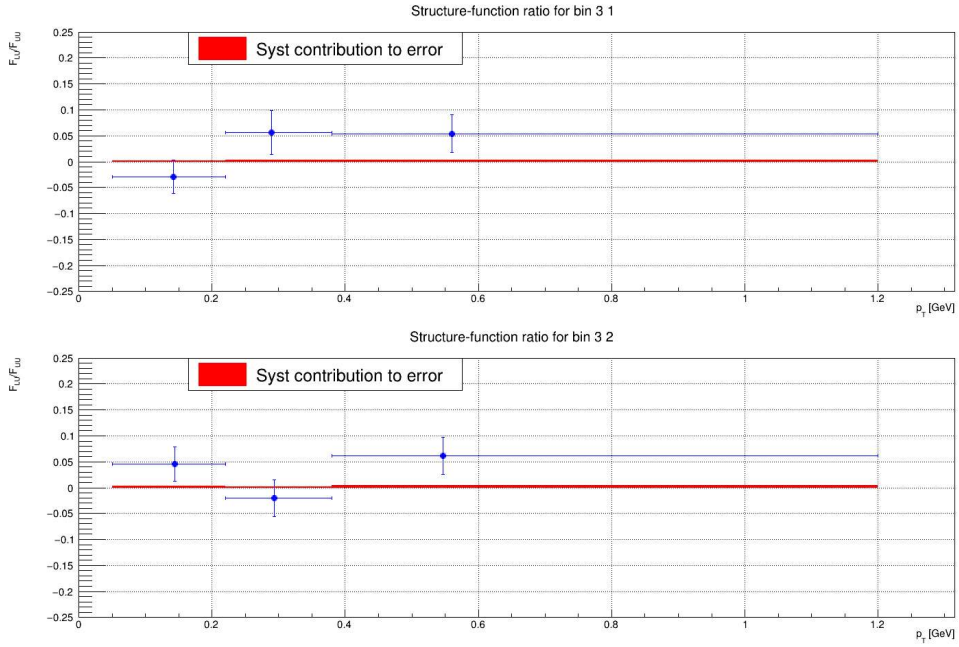

Figure 55: $F_{LU}^{\sin\phi}$ as a function of p_T, for the third bin on the electron variables and the two bins in z. The mean values and bin extremes are $Q^2 = 3.7(1.3, 11.0)$, $x_B = 0.28(0.19, 0.75)$ for both plots and respectively $z = 0.50(0.35, 0.58)$ and $z = 0.68(0.58, 0.95)$ for top and bottom. The x-coordinate of each point shows the mean value of p_T, and the correspondent error bar shows the bin width.

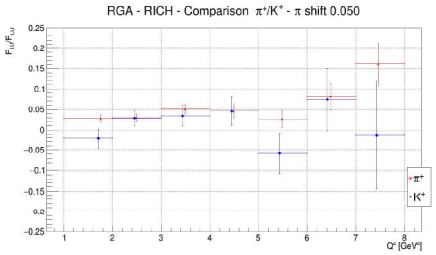

(a) Comparison as a function of Q^2.

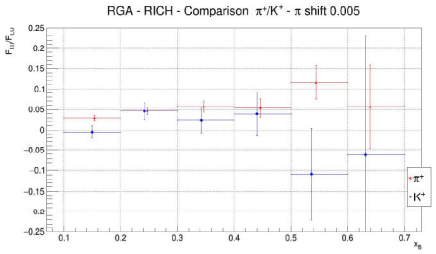

(b) Comparison as a function of x_B.

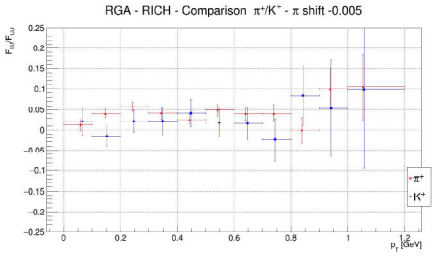

(c) Comparison as a function of p_T.

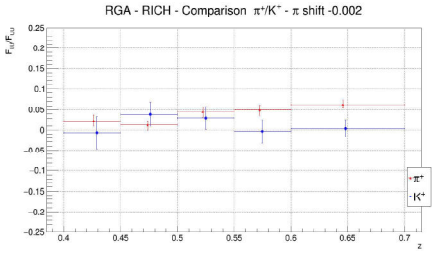

(d) Comparison as a function of z.

Figure 56: $F_{LU}^{\sin\phi}/F_{UU}$ obtained from pion and kaon samples identified by the RICH. The points for pion are slightly shifted along the x-axis to not overlap the error bars

Acronyms

ALCOR A Low Power Chip for Optical Sensor Readout.

AMS-02 Alpha Magnetic Spectrometer.

BAND Back Angle Neutron Detector.

bECAL Barrel Electromagnetic Calorimeter.

bHCAL Barrel Hadronic Calorimeter.

BNL Brookhaven National Laboratory.

BSA Beam-Spin Asymmetry.

CD Central Detector.

CEBAF Continuous Electron Beams Accelerator Facility.

CERN European Council for Nuclear Research.

CLAS12 CEBAF Large Acceptance Spectrometer for operation at 12 GeV.

CND Central Neutron Detector.

CTOF Central Time-Of-Flight.

CVT Central Vertex Tracker.

DC Drift Chamber.

DCR Dark Count Rate.

DESY Deutsches Elektronen-Synchrotron.

DIS Deep Inelastic Scattering.

dRICH dual-radiator Ring Imaging Cherenkov.

DY Drell-Yan.

EC Electromagnetic Calorimeter.

ECAL EElectromagnetic and Pre-shower Calorimeter.

eECAL Backward Electromagnetic Calorimeter.

eHCAL Backward Hadronic Calorimeter.

EIC Electron-Ion Collider.

ePIC Electron-Proton/Ion Collider Experiment.

FBK Fondazione Bruno Kessler.

FD Forward Detector.

FF Fragmentation Function.

FFs Fragmentation Functions.

FT Forward Tagger.

FTOF Forward Time-Of-Flight.

GEM Gas Electron Multiplier.

GEMC GEant4 Monte-Carlo.

GPDs Generalized Parton Distributions.

hECAL Forward Electromagnetic Calorimeter.

HERA Hadron-Elektron-Ringanlage.

hHCAL Forward Hadronic Calorimeter.

HIPO HIghly Performance Output.

hpDIRC high-performance Detection of Internally Reflected Cherenkov light.

HTCC High Threshold Cherenkov Counter.

INFN Istituto Nazionale di Fisica Nucleare.

JLab Jefferson Laboratory.

JLab Thomas Jefferson National Accelerator Facility.

LHCb Large Hadron Collider beauty.

LHCspin LHC fixed-target experiment.

LTCC Low Threshold Cherenkov Counter.

MAPMT Multi-Anode Photomultiplier Tube.

MAPMTs Multi-Anode Photomultiplier Tubes.

MARCO MAgnet with Renewed COils.

MAROC Multi-Anode ReadOut Chip.

MC Monte Carlo.

MIT Massachusetts Institute of Technology.

MPPC Multi-Pixel Photon Counter.

MPPCs Multi-Pixel Photon Counters.

PCAL Pre-shower Calorimeter.

PDF Parton Distribution Function.

PDF Probability Density Function.

PDFs Parton Distribution Functions.

pfRICH proximity-focusing RICH.

PID Particle Identification.

PM Parton Model.

PS Proton Synchrotron.

QCD Quantum Chromodynamics.

QM Quark Model.

QPM Quark Parton Model.

RG-A Run Group A.

RG-B Run Group B.

RHIC Relativistic Heavy Ion Collider.

RICH Ring Imaging Cherenkov.

SIDIS Semi-Inclusive Deep Inelastic Scattering.

SiPM Silicon Photomultiplier.

SiPMs Silicon Photomultipliers.

SLAC Stanford Linear Accelerator Center.

SPE Single PhotoElectron.

SPS Super Proton Synchrotron.

TMD Transverse-Momentum-Dependent.

UML Unbinned Maximum Likelihood.

Bibliography

[1] Y. Ne'eman. "Derivation of strong interactions from a gauge invariance". In: *Nuclear Physics* 26.2 (1961), pp. 222–229. ISSN: 0029-5582. DOI: 10.1016/0029-5582(61)90134-1.

[2] Murray Gell-Mann. "Symmetries of Baryons and Mesons". In: *Phys. Rev.* 125 (3 Feb. 1962), pp. 1067–1084. DOI: 10.1103/PhysRev.125.1067.

[3] Murray Gell-Mann. "A Schematic Model of Baryons and Mesons". In: *Phys. Lett.* 8 (1964), pp. 214–215. DOI: 10.1016/S0031-9163(64)92001-3.

[4] G. Zweig. "An SU(3) model for strong interaction symmetry and its breaking. Version 2". In: *DEVELOPMENTS IN THE QUARK THEORY OF HADRONS. VOL. 1. 1964 - 1978.* Ed. by D. B. Lichtenberg and Simon Peter Rosen. Feb. 1964, pp. 22–101. DOI: 10.17181/CERN-TH-412.

[5] Renaud Boussarie et al. *TMD Handbook.* 2023. DOI: 10.48550/arXiv.2304.03302.

[6] O. W. Greenberg. "Spin and Unitary-Spin Independence in a Paraquark Model of Baryons and Mesons". In: *Phys. Rev. Lett.* 13 (20 Nov. 1964), pp. 598–602. DOI: 10.1103/PhysRevLett.13.598.

[7] John Collins. *Foundations of Perturbative QCD.* Cambridge Monographs on Particle Physics, Nuclear Physics and Cosmology. Cambridge University Press, 2023. DOI: 10.1017/9781009401845.

[8] J. I. Friedman. *Nobel lecture.* 1990. URL: https://www.nobelprize.org/uploads/2018/06/friedman-lecture.pdf.

[9] H. W. Kendall. *Nobel lecture.* 1990. URL: https://www.nobelprize.org/uploads/2018/06/kendall-lecture.pdf.

[10] R. E. Taylor. *Nobel lecture.* 1990. URL: https://www.nobelprize.org/uploads/2018/06/taylor-lecture.pdf.

[11] J. D. Bjorken. "Asymptotic Sum Rules at Infinite Momentum". In: *Phys. Rev.* 179 (5 Mar. 1969), pp. 1547–1553. DOI: 10.1103/PhysRev.179.1547.

[12] J. D. Bjorken and E. A. Paschos. "Inelastic Electron-Proton and γ-Proton Scattering and the Structure of the Nucleon". In: *Phys. Rev.* 185 (5 Sept. 1969), pp. 1975–1982. DOI: 10.1103/PhysRev.185.1975.

[13] Richard P. Feynman. "Very High-Energy Collisions of Hadrons". In: *Phys. Rev. Lett.* 23 (24 Dec. 1969), pp. 1415–1417. DOI: 10.1103/PhysRevLett.23.1415.

[14] Sidney D. Drell and Tung-Mow Yan. "Massive Lepton-Pair Production in Hadron-Hadron Collisions at High Energies". In: *Phys. Rev. Lett.* 25 (5 Aug. 1970), pp. 316–320. DOI: 10.1103/PhysRevLett.25.316.

[15] Edmond L. Berger. "Massive Lepton Pair Production--What has QCD Done to the Classical Drell-Yan Model?" In: *AIP Conference Proceedings* 98.1 (Apr. 1983), pp. 312–342. ISSN: 0094-243X. DOI: 10.1063/1.2947551.

[16] R. K. Ellis, W. J. Stirling, and B. R. Webber. *QCD and Collider Physics*. Cambridge Monographs on Particle Physics, Nuclear Physics and Cosmology. Cambridge University Press, 1996. DOI: 10.1017/CBO9780511628788.

[17] M.E. Peskin and D.V. Schroeder. *An Introduction To Quantum Field Theory*. Frontiers in Physics. Avalon Publishing, 1995. ISBN: 9780813345437. URL: https://books.google.it/books?id=EVeNNcslvX0C.

[18] Jozef Dudek et al. "Physics opportunities with the 12 GeV upgrade at Jefferson Lab". In: *The European Physical Journal A* 48.12 (Dec. 2012). ISSN: 1434-601X. DOI: 10.1140/epja/i2012-12187-1.

[19] V. D. Burkert et al. "The CLAS12 Spectrometer at Jefferson Laboratory". In: *Nucl. Instrum. Meth. A* 959 (2020), p. 163419. DOI: 10.1016/j.nima.2020.163419.

[20] R. Abdul Khalek et al. "Science Requirements and Detector Concepts for the Electron-Ion Collider: EIC Yellow Report". In: *Nuclear Physics A* 1026 (2022), p. 122447. ISSN: 0375-9474. DOI: 10.1016/j.nuclphysa.2022.122447.

[21] M Anselmino et al. "New insight on the Sivers transverse momentum dependent distribution function". In: *Journal of Physics: Conference Series* 295 (May 2011), p. 012062. ISSN: 1742-6596. DOI: 10.1088/1742-6596/295/1/012062.

[22] Miguel G. Echevarria et al. "QCD evolution of the Sivers asymmetry". In: *Phys. Rev. D* 89 (7 Apr. 2014), p. 074013. DOI: 10.1103/PhysRevD.89.074013.

[23] M. Anselmino et al. "Publisher's Note: Extracting the Sivers function from polarized semi-inclusive deep inelastic scattering data and making predictions [Phys. Rev. D 72, 094007 (2005)]". In: *Phys. Rev. D* 72 (9 Nov. 2005), p. 099903. DOI: 10.1103/PhysRevD.72.099903.

[24] J. C. Collins et al. "Sivers effect in semiinclusive deeply inelastic scattering". In: *Phys. Rev. D* 73 (1 Jan. 2006), p. 014021. DOI: 10.1103/PhysRevD.73.014021.

[25] Werner Vogelsang and Feng Yuan. "Single-transverse-spin asymmetries: From deep inelastic scattering to hadronic collisions". In: *Phys. Rev. D* 72 (5 Sept. 2005), p. 054028. DOI: 10.1103/PhysRevD.72.054028.

[26] Alessandro Bacchetta and Marco Radici. "Constraining Quark Angular Momentum through Semi-Inclusive Measurements". In: *Phys. Rev. Lett.* 107 (21 Nov. 2011), p. 212001. DOI: 10.1103/PhysRevLett.107.212001.

[27] M. Anselmino et al. "Sivers effect for pion and kaon production in semi-inclusive deep inelastic scattering". In: *The European Physical Journal A* 39.1 (2009), pp. 89–100. ISSN: 1434-601X. DOI: 10.1140/epja/i2008-10697-y.

[28] Alessandro Bacchetta et al. "The 3-dimensional distribution of quarks in momentum space". In: *Physics Letters B* 827 (2022), p. 136961. ISSN: 0370-2693. DOI: 10.1016/j.physletb.2022.136961.

[29] Miguel G. Echevarria, Zhong-Bo Kang, and John Terry. "Global analysis of the Sivers functions at NLO+NNLL in QCD". In: *Journal of High Energy Physics* 2021.1 (2021), p. 126. ISSN: 1029-8479. DOI: 10.1007/JHEP01(2021)126.

[30] Marcin Bury, Alexei Prokudin, and Alexey Vladimirov. "Extraction of the Sivers Function from SIDIS, Drell-Yan, and $W^{\pm}/Z$ Data at Next-to-Next-to-Next-to Leading Order". In: *Phys. Rev. Lett.* 126 (11 Mar. 2021), p. 112002. DOI: 10.1103/PhysRevLett.126.112002.

[31] A. Bacchetta and M Contalbrigo. *The proton in 3D*. Article on Il Nuovo Saggiatore. 2012. URL: https://www.ilnuovosaggiatore.sif.it/issue/10.

[32] Elke-Caroline Aschenauer et al. *The RHIC SPIN Program: Achievements and Future Opportunities*. 2015. arXiv: 1501.01220 [nucl-ex].

[33] M. Santimaria et al. "The LHCspin project". In: *SciPost Phys. Proc.* (2022), p. 050. DOI: 10.21468/SciPostPhysProc.8.050.

[34] A. Airapetian et al. "Azimuthal single- and double-spin asymmetries in semi-inclusive deep-inelastic lepton scattering by transversely polarized protons". In: *Journal of High Energy Physics* 2020.12 (2020), p. 10. ISSN: 1029-8479. DOI: 10.1007/JHEP12(2020)010.

[35] Alessandro Bacchetta et al. "Semi-inclusive deep inelastic scattering at small transverse momentum". In: *Journal of High Energy Physics* 2007.02 (Feb. 2007), p. 093. DOI: 10.1088/1126-6708/2007/02/093.

[36] S. Bastami et al. "Semi-inclusive deep-inelastic scattering in Wandzura-Wilczek-type approximation". In: *Journal of High Energy Physics* 2019.6 (2019), p. 7. ISSN: 1029-8479. DOI: 10.1007/JHEP06(2019)007.

[37] S. Wandzura and F. Wilczek. "Sum rules for spin-dependent electroproduction-test of relativistic constituent quarks". In: *Physics Letters B* 72.2 (1977), pp. 195–198. ISSN: 0370-2693. DOI: 10.1016/0370-2693(77)90700-6.

[38] S. Diehl et al. "Multidimensional, High Precision Measurements of Beam Single Spin Asymmetries in Semi-inclusive π^+ Electroproduction off Protons in the Valence Region". In: *Phys. Rev. Lett.* 128 (6 Feb. 2022), p. 062005. DOI: 10.1103/PhysRevLett.128.062005.

[39] A. Accardi et al. *Strong Interaction Physics at the Luminosity Frontier with 22 GeV Electrons at Jefferson Lab.* 2023. arXiv: 2306.09360 [nucl-ex].

[40] M. Contalbrigo et al. "The CLAS12 Ring Imaging Cherenkov detector". In: *Nuclear Instruments and Methods in Physics Research Section A: Accelerators, Spectrometers, Detectors and Associated Equipment* 964 (2020), p. 163791. ISSN: 0168-9002. DOI: 10.1016/j.nima.2020.163791.

[41] M. Contalbrigo et al. "Aerogel mass production for the CLAS12 RICH: Novel characterization methods and optical performance". In: *Nuclear Instruments and Methods in Physics Research Section A: Accelerators, Spectrometers, Detectors and Associated Equipment* 876 (2017). The 9th international workshop on Ring Imaging Cherenkov Detectors (RICH2016), pp. 168–172. ISSN: 0168-9002. DOI: 10.1016/j.nima.2017.02.068.

[42] E Aschenauer et al. "Optical characterization of n=1.03 silica aerogel used as radiator in the RICH of HERMES". In: *Nuclear Instruments and Methods in Physics Research Section A: Accelerators, Spectrometers, Detectors and Associated Equipment* 440.2 (2000), pp. 338–347. ISSN: 0168-9002. DOI: 10.1016/S0168-9002(99)00923-7.

[43] *Composite Mirror Company.* URL: https://www.compositemirrors.com/.

[44] *Evaporated Coatings Inc.* URL: https://evaporatedcoatings.com/.

[45] *Media Lario Company.* URL: https://www.medialario.com/.

[46] Sylvie Blin, Pierre Barrillon, and Christophe de La Taille. "MAROC, a generic photomultiplier readout chip". In: *IEEE Nucl. Sci. Symp. Conf. Rec.* 2010 (2010). Ed. by Ron Keyser, pp. 1690–1693. DOI: 10.1109/NSSMIC.2010.5874062.

[47] R. L. Workman et al. "Review of Particle Physics". In: *PTEP* 2022 (2022), p. 083C01. DOI: 10.1093/ptep/ptac097.

[48] T. B. Hayward. *Dihadron beam spin asymmetries on an unpolarized hydrogen target with CLAS12*. PhD thesis. 2021. DOI: 10.21220/xxae-1q88.

[49] Roger Barlow. "Extended maximum likelihood". In: *Nuclear Instruments and Methods in Physics Research Section A: Accelerators, Spectrometers, Detectors and Associated Equipment* 297.3 (1990), pp. 496–506. ISSN: 0168-9002. DOI: 10.1016/0168-9002(90)91334-8.

[50] Run Group A - CLAS COLLABORATION. *CLAS12 RG-A - Analysis Note Overview and Procedures*. URL: https://clas12-docdb.jlab.org/DocDB/0007/000771/001/RGA_Analysis_Overview_and_Procedures_10082020.pdf.

[51] A. Airapetian et al. "Beam-helicity asymmetries for single-hadron production in semi-inclusive deep-inelastic scattering from unpolarized hydrogen and deuterium targets". In: *Physics Letters B* 797 (2019), p. 134886. ISSN: 0370-2693. DOI: 10.1016/j.physletb.2019.134886.

[52] C. Adolph et al. "Measurement of azimuthal hadron asymmetries in semi-inclusive deep inelastic scattering off unpolarised nucleons". In: *Nuclear Physics B* 886 (2014), pp. 1046–1077. ISSN: 0550-3213. DOI: 10.1016/j.nuclphysb.2014.07.019.

[53] M. Calvi et al. "Single photon detection with SiPMs irradiated up to 1014 cm−2 1-MeV-equivalent neutron fluence". In: *Nuclear Instruments and Methods in Physics Research Section A: Accelerators, Spectrometers, Detectors and Associated Equipment* 922 (2019), pp. 243–249. ISSN: 0168-9002. DOI: 10.1016/j.nima.2019.01.013.

[54] Roberto Preghenella et al. "A SiPM-based optical readout system for the EIC dual-radiator RICH". In: *Nuclear Instruments and Methods in Physics Research Section A: Accelerators, Spectrometers, Detectors and Associated Equipment* 1046 (2023), p. 167661. ISSN: 0168-9002. DOI: 10.1016/j.nima.2022.167661.

[55] A. Vasilescu and G. Lindstroem. *Displacement damage in silicon, online compilation*. URL: http://rd50.web.cern.ch/NIEL/.

[56] S. Vallarino et al. "Prototype of a dual-radiator RICH detector for the Electron-Ion Collider". In: *Nuclear Instruments and Methods in Physics Research Section A: Accelerators, Spectrometers, Detectors and Associated Equipment* 1058 (2024), p. 168834. ISSN: 0168-9002. DOI: 10.1016/j.nima.2023.168834.

[57] *Aerogel Factory Co.* URL: https://www.aerogel-factory.jp/.

[58] A. R. Altamura. *Aerogel characterization*. dRICH Meeting. 2023. URL: https://indico.bnl.gov/event/19345/?print=1.

[59] Chandradoy Chatterjee. *ePIC dRICH Simulation and reconstruction status update*. 2024. URL: https://indico.bnl.gov/event/20473/contributions/85263/attachments/51974/88884/dRICH_ePIC_CM_Simupdate.pdf.

[60] M. Ungaro et al. "The CLAS12 Geant4 simulation". In: *Nuclear Instruments and Methods in Physics Research Section A: Accelerators, Spectrometers, D etectors and Associated Equipment* 959 (2020), p. 163422. ISSN: 0168-9002. DOI: 10.1016/j.nima.2020.163422.

[61] URL: https://gemc.jlab.org/gemc/html/index.html.

[62] L. Re et al. "Characterization of three GEM chambers for the SBS front tracker at JLab Hall A". In: *Radiation Effects and Defects in Solids* 173.9-10 (2018), pp. 818–828. DOI: 10.1080/10420150.2018.1528607.

Acknowledgments

Non sono bravo a scrivere dei ringraziamenti, alla fine non sono mai soddisfatto ed è così anche stavolta. Vorrei sempre riuscire ad esprimere più gratitudine di quella che traspare dalle parole che riesco a trovare, o quanto meno descrivendo più precisamente i motivi per cui vi cito.

A Marco Contalbrigo, che mi ha accolto nel gruppo ferrarese, introducendomi all'affascinante mondo dei rivelatori Cherenkov e allo studio del nucleone in tre dimensioni. Grazie per avermi supportato in questi anni, aiutandomi ad imparare molto e permettendomi di spaziare su tutti gli aspetti della vita del fisico sperimentale. Grazie per gli stimoli continui a migliorare e non avermi lasciato accontentare del minimo indispensabile.

A Luca Barion, che in questi anni è stato una presenza costante. Grazie per essere stato sempre pronto a trovare una soluzione alle difficoltà concrete si incontrano durante il lavoro quotidiano.

A Bianca, che con il suo sguardo avanti nel tempo, ha visto il mio futuro molto prima di me. Grazie perché continui ad essere una fonte di ispirazione.

A Vincenzo, Fabio e Costantino. Grazie della vostra amicizia, che nonostante la lontanza mi permette di sapere che in ogni momento possiamo sentirci per un consiglio, o anche solo una chiacchierata.

A Giulio, Ilaria, Marco, Riccardo, Matteo, Nicola, Stefano, Gigi e a tutti gli altri che sto sicuramente dimenticando. Grazie per avermi fatto sentire accolto e desiderato a Ferrara, come persona oltre che come fisico. Grazie per tutti i pranzi e le serate, le discussioni e le birre che abbiamo condiviso. Avete sicuramente reso molto più piacevole la mia esperienza ferrarese.

Ad Ermanno Berio e Fra Luca Pozzi. Grazie, perché in diversi momenti della mia vita siete stati delle figure di riferimento e avete contribuito molto più di quanto si potrebbe immaginare a rendermi chi sono oggi.

A mia mamma Valeria, mio papà Enrico e mio fratello Davide. Grazie. I motivi ovviamente sono tanti, ma in particolare grazie perché la certezza del vostro sostegno continuo mi ha fornito la tranquillità di scegliere la mia strada inseguendo ciò che mi piace fare.

A Costy. Grazie perché sai guardarmi dentro come nessun altro, accettando ogni mio lato. E grazie perché da quasi cinque anni aggiungi sapore alla mia vita, dandomi motivi per sorridere ed essere felice ogni giorno.